UNIVERSIDAD NACIONAL AUTÓNOMA DE MÉXICO

PROGRAMA DE POSGRADO EN ASTROFÍSICA

INSTITUTO DE RADIOASTRONOMÍA Y ASTROFÍSICA

THE RELATION BETWEEN MORPHOLOGY, STELLAR PROPERTIES, AND ENVIRONMENT OF GALAXIES IN THE LOCAL UNIVERSE

Tesis que para optar por del grado de

DOCTOR EN CIENCIAS (ASTROFÍSICA)

presenta

DAVID PÉREZ MILLÁN

Tutores Principales:

DR. JACOPO FRITZ

INSTITUTO DE RADIOASTRONOMÍA Y ASTROFÍSICA

DRA. ROSA A. GONZÁLEZ-LÓPEZLIRA

INSTITUTO DE RADIOASTRONOMÍA Y ASTROFÍSICA

Morelia, México - agosto 2023

David Pérez Millán
The relation between morphology, stellar properties, and environment of galaxies in the local universe
Doctorado en Ciencias (Astrofísica)

TUTORES:
Dr. Jacopo Fritz
Dra. Rosa A. González-Lópezlira
INSTITUTO DE RADIOASTRONOMÍA Y ASTROFÍSICA

Morelia, México, agosto 2023

Dedicated to my loving parents, my great sister, and my sweet girlfriend.

Love is the strongest force in the universe.

ABSTRACT

Among the main questions faced by modern extragalactic astrophysics are the origin and the evolution of galaxy properties. While stellar evolution is the main driver of changes in isolated galaxies, and also dictates their timescales, galaxies in clusters are subject to a whole range of processes and interactions that dramatically change this picture. During the last decades diverse physical mechanisms, that are believed to be responsible for the differences in galaxy properties between low and high-density environments, have been both proposed and observationally identified. To this day, however, pinpointing exactly what the phenomena responsible for these changes are, and to what degree, is still an open question.

To shed light on these issues, we exploit optical spectra from the WIde-field Nearby Galaxy–cluster Survey (WINGS) and its extension OmegaWINGS ($0.04 < z < 0.07$). We use stellar population synthesis techniques to analyze these spectra and obtain properties related to the stars in the galaxies, e. g., stellar mass, stellar ages, star formation rates, and star formation histories. The data include both cluster member and non-member galaxies. Non-member galaxies are analyzed in the same way as cluster members. A thorough comparison between cluster and field galaxies, made by controlling for their most important properties, allows us to quantify the effect of the environment.

Our results show that, although the cluster environment eventually shuts down star formation, several mechanisms at play may instead temporarily enhance it. For example, ram pressure and close encounters with other galaxies can initiate star formation; nevertheless, this further accelerates gas depletion. Likewise, it is of fundamental importance to take morphology into account: while cluster late-type galaxies do follow the main sequence of star-forming galaxies, early-type galaxies display some level of star formation as well, likely triggered by hydrodynamic interactions with the intercluster gas or gravitational interactions with other cluster members. However, the star formation rates of elliptical and S0 galaxies do not show a significant correlation with their stellar mass. Hence, their (very) local environment is the one that shapes the properties of their recent stellar populations, while the global influence of the cluster is likely a secondary agent, resulting from the sum of local ones. In short, the influence of the environment, modulated by the local density of galaxies, is imprinted on the galaxy morphology.

In an attempt to draw a more general picture, we also analyze other parameters in the study of stellar properties, such as the presence/absence of a stellar bar and the effects of merging/relaxed clusters. We likewise observe the influence of strong ram pressure on a sample of jellyfish galaxies. These parameters and phenomena are

analyzed separately. We figure that the issue of the virialized/merging state of clusters and its possible influence on galaxy properties must be addressed in the future with a larger and better defined sample.

Finally, using data from the ESO Distant Cluster Survey (EDisCS; $0.4 < z < 1.0$), we compare our main results at low redshift with those at intermediate-high redshift. We confirm some known findings, such as the morphological evolution through cosmic time and the larger star formation rate on the main sequence at higher redshift. We also determine that clusters may have been more efficient in quenching star formation in the past, and we propose that the general higher star formation activity in galaxies at these redshifts may explain the Butcher–Oemler effect.

Key words: galaxies: clusters: general — galaxies: evolution — galaxies: stellar content —- stars: formation

RESUMEN

Entre las mayores preguntas que la astrofísica extragaláctica moderna enfrenta están el origen y evolución de las propiedades de las galaxias. Mientras que la evolución estelar es el factor principal de los cambios en las galaxias aisladas, y también dicta sus escalas de tiempo, las galaxias en cúmulos están sujetas a un amplio rango de procesos e interacciones que cambian dramáticamente este panorama. Durante las últimas décadas diversos mecanismos físicos, que se creían ser responsables de las diferencias en las propiedades de las galaxias entre ambientes de baja y alta densidad, han sido propuestos e identificados observacionalmente. Al día de hoy, sin embargo, determinar exactamente cuáles son los fenómenos responsables de estos cambios, y a cuál grado, es todavía un problema abierto.

Para arrojar luz en estos temas, aprovechamos los espectros ópticos del WIde-field Nearby Galaxy–cluster Survey (WINGS) y su extensión OmegaWINGS ($0.04 < z < 0.07$). Usamos técnicas de síntesis de poblaciones estelares para analizar estos espectros y obtener propiedades relacionadas con las estrellas en las galaxias, por ejemplo, masa estelar, edades estelares, tasas de formación estelar, e historias de formación estelar. Los datos incluyen galaxias miembros y no miembros de cúmulos. Las galaxias no miembros son analizadas de la misma manera como los miembros de cúmulos. Una minuciosa comparación entre galaxias de cúmulos y del campo, hecha controlando las propiedades más importantes de las galaxias, nos permite cuantificar el efecto del ambiente.

Nuestros resultados muestran que, aunque el ambiente del cúmulo eventualmente apaga la formación de estrellas, varios mecanismos en juego, al contrario, temporalmente la encienden. Por ejemplo, presión ram y encuentros cercanos con otras galaxias pueden iniciar la formación de estrellas; no obstante, de esta forma se acelera el agotamiento del gas. Del mismo modo, es de importancia fundamental tomar en cuenta la morfología: mientras que las galaxias de tipo tardío en cúmulos siguen la secuencia principal de las galaxias con formación de estrellas activa, las galaxias de tipo temprano también muestran cierto nivel de formación de estrellas, probablemente inducido por interacciones hidrodinámicas con el gas intracumular o iteracciones gravitacionales con otros miembros del cúmulo. Sin embargo, la tasa de formación de estrellas en las galaxias elípticas y lenticulares no muestra una correlación significativa con su masa estelar. Por consiguiente, su ambiente (muy) local es el que da forma a las propiedades de sus poblaciones estelares recientes, mientras que la influencia global del cúmulo es probablemente un agente secundario, resultando de la suma de los efectos locales. En pocas palabras, la influencia del

ambiente, modulada por la densidad local de las galaxias, deja huella en la morfología de las galaxias.

En un esfuerzo por elaborar un panorama más global, también analizamos otros parámetros en el estudio de las propiedades estelares, tales como la presencia/ausencia de una barra estelar y los efectos de cúmulos en fusión o relajados. Asimismo, observamos la influencia de presión ram intensa en una muestra de galaxias medusa. Estos parámetros y fenómenos son analizados separadamente. También proponemos que el problema del estado de virialización/fusión de los cúmulos y su posible influencia en las propiedades de las galaxias debe ser abordado en el futuro con una muestra más grande y mejor definida

Finalmente, usando datos del ESO Distant Cluster Survey (EDisCS) ($0.4 < z < 1.0$), comparamos nuestros principales resultados a bajo corrimiento al rojo con los de intermedio–alto. Confirmamos algunos resultados conocidos como la evolución morfológica a través del tiempo cósmico y la tasa de formación de estrellas más alta en la secuencia principal a corrimiento del rojo más alto. Asimismo, determinamos que los cúmulos podrían haber sido más eficientes en apagar la formación de estrellas en el pasado y proponemos que la actividad de formación de estrellas en general más alta en galaxias a estos corrimientos al rojo, y la carencia de transformación morfológica en los cúmulos locales podría explicar el efecto Butcher–Oemler.

Palabras clave: galaxias: cúmulos: general — galaxias: evolución — galaxias: contenido estelar —- estrellas: formación

AGRADECIMIENTOS

Dios, gracias por tu amor, tu cuidado, porque me has guiado hasta aquí, y lo seguirás haciendo cada día.

Padres: Gladys y Cantalicio, gracias por su amor, motivación, apoyo, y oraciones. Gracias por aconsejarme y ofrecerme siempre lo mejor.

Hermana: Judith Esther, gracias por tu apoyo como hermanos, por estar conmigo a pesar de la distancia, y por sentirte orgullosa de mí.

Novia, gracias por tu amor, tus palabras, tu tiempo, y por siempre estar para mí.

Amigos, gracias por su compañía y porque con ustedes estos años fueron más llevaderos.

Tutores: Jacopo y Rosa Amelia, gracias porque siempre estuvieron disponibles para mí, a cualquier hora y día. Gracias por enseñarme con paciencia y darme todo lo que necesité. Gracias por sus cartas de recomendación y solicitudes de becas. Profesor Bernardo, gracias por todos sus aportes, sugerencias, y toda la ayuda en este trabajo.

Comité sinodal: Dr. Eric Jiménez, Dr. Ricardo Chávez, Dr. Omar López, Dr. Rory Smith, y Dra. Mariana Cano, gracias por tomar el tiempo necesario para leer esta tesis y darme tan buenos comentarios y sugerencias que fueron de gran utilidad para tener esta versión final. Gracias por su buena voluntad.

Comité académico: Dra. Omaira González, Dra. Verónica Lora, y Dr. Héctor Bravo, gracias por su tiempo para las reuniones semestrales y sus consejos para finalmente graduarme.

Esta tesis fue realizada gracias al apoyo recibido del Consejo Nacional de Humanidades, Ciencias y Tecnologías (CONAHCyT), así como al Programa de Apoyo a Proyectos de Investigación e Innovación Tecnológica (PAPIIT) con el proyecto IN111620 durante los años de mis estudios de posgrado para obtener el grado de Doctor en Ciencias, en la especialidad de Astrofísica.

CONTENTS

LIST OF FIGURES

LIST OF TABLES

ACRONYMS

AGN active galactic nuclei

BCG brightest cluster galaxy

EDisCS ESO Distant Cluster Survey

EW equivalent width

FWHM full width at half maximum

GASP GAs Stripping Phenomena in galaxies with MUSE

HST Hubble Space Telescope

ICM intracluster medium

IFU integral field unit

IMF initial mass function

IR infrared

ISM interstellar medium

K-S Kolmogorov-Smirnov

LD local density

MS main sequence

PM2GC Padova-Millennium Galaxy and Group Catalogue

RP ram pressure

RPS ram-pressure stripping

SDSS Sloan Digital Sky Survey

SF star-forming

SFH star formation history

SFR star formation rate

SINOPSIS SImulatiNg OPtical Spectra wIth Stellar population models

SNR signal-to-noise ratio

sSFR specific star formation rate

SSP simple stellar population

VLT Very Large Telescope

WINGS WIde-field Nearby Galaxy–cluster Survey

Part I

THEORETICAL FRAMEWORK

1 INTRODUCTION

One of the main challenges faced by modern extragalactic astrophysics is understanding the different mechanisms impelling changes in galactic properties. While isolated galaxies follow evolutionary paths and timescales that are mostly driven by the typical processes of stellar evolution, galaxies in clusters are subject to a whole range of different processes and interactions that dramatically change that picture. This is reflected in the differences between the galaxy populations of clusters and those of the field, as we will see below.

If a galaxy enters a cluster, its evolution receives a kick that accelerates changes in its stellar and interstellar medium (ISM) content and modifies its morphology as well. What processes are the main drivers of these changes? Which galactic components and properties do they affect the most? Under which conditions does one mechanism dominate over the others? What are the prevailing effects: those from the global environment or those of the local one? How and when is star formation in galaxies quenched? What is the fraction of quenched galaxies by morphology, and is this fraction driven by galactic mass or by the environment? Are the stellar populations of galaxies in regular and irregular clusters similar? Can we link the properties of high-redshift galaxies to those of local ones? These are some of the issues that this thesis tries to shed light on; many of them are also among the main incentives for the development of present and upcoming future space missions.

One additional difficulty is that the properties of different clusters present a large variance [e.g., Poggianti et al. (2006), Brodwin et al. (2015)]. Disentangling the effects of cosmic evolution on a broad spectrum of cluster and galaxy properties is not an easy task, and different results can be obtained by analyzing diverse observations of distinct samples. Even more, cluster and galaxy samples are not complete for all luminosities, cluster masses, and environments, and all these properties could depend on redshift. In this work, we try to answer some of these main questions to better understand the phenomena involved in galaxy evolution.

1.1 GALAXY CLUSTERS

Galaxy clusters are the largest (typically a few Mpc of size) systems bound gravitationally in the universe. They are density peaks in the galaxy distribution and can be used to probe a broad range of physical conditions, from the dense cores to the outermost low-density regions. They provide large samples of galaxies at the

same redshift in a relatively small observable field. It is in dense environments, such as clusters and compact groups, that we can directly observe the effects of a very high spatial density of galaxies, and of repeated interactions between galaxies and with the intergalactic medium. As a consequence, clusters constitute an ideal place to trace galaxy evolution and investigate the effects of the environment on galaxies, both theoretically and observationally.

The pioneer works of George Abell were among the first to define a galaxy cluster. Looking at photographic plates of the Palomar Observatory Sky Survey (POSS), he identified them as overdensities of galaxies containing at least 50 objects within a certain radius ($1.72/z$, in arcmin)[1], with a magnitude between m_3 and $m_3 + 2$, where m_3 is the magnitude of the third brightest galaxy within the overdensity itself. This led to the first classification in terms of richness, based on the number of galaxies within the radial and magnitude ranges. Other classifications were also proposed, such as by distance (redshift), compactness, and morphology.

Galaxy clusters can be defined and classified according to different parameters. Clusters with a Gaussian or a non-Gaussian velocity distribution in the line-of-sight are classified as, respectively, relaxed (virialized) or non-relaxed (non-virialized) [Hou et al. (2009)]. Furthermore, the spatial distribution of galaxies within the cluster is indicative of the cluster relaxation state. Relaxed clusters have an approximately spherical shape with non-significant substructures, while non-relaxed ones can present elongated and/or irregular shapes with strong signs of substructures [Zhang et al. (2022), Brambila et al. (2023)]. Morell et al. (2020) analyzed a sample of 146 clusters and found that galaxies evolve in the same way, regardless of the dynamical state of the cluster. However, spiral galaxies dominate the infall in non-Gaussian clusters, whereas Gaussian systems receive all types of galaxy morphologies. Lopes et al. (2018) recommend separating relaxed from disturbed clusters, either using two parameters. The disturbed ones will be those with an offset $\gtrsim 0.01\ R_{500}$ between the brightest cluster galaxy (BCG) and the X-ray centroid, or a magnitude gap between the first and second BCGs $\Delta m < 1.0$ mag.

Clusters can also grow through mergers with other clusters. These are among the most energetic events in the universe [Mann & Ebeling (2012)], in particular when they involve an interaction between similarly massive clusters. These occurrences provide a unique opportunity to study the most extreme environments and their effects on galaxies.

Field galaxies

Cluster galaxies are usually defined by means of a spectroscopic membership (those galaxies within $\pm$ 3 times the cluster velocity dispersion in the line-of-sight) while,

1 Where z was estimated assuming that the tenth brightest galaxy in an overdensity is a standard candle.

on the other side, field galaxies are defined as non-cluster members. Observations show that galaxy abundance (number density), color, and morphology depend on the environment where they are located [McIntosh et al. (2004)], and that the transformation of galaxies, regarding both stellar content and morphology, is not restricted to the dense cluster cores. For example, even in the local field, there is a considerable population of quenched galaxies [Noeske et al. (2007)].

In particular, late-type galaxies are significantly different in the cluster and field environments [Boselli & Gavazzi (2006)]; in clusters, they are more gas deficient, redder, and with a lower star formation rate (SFR) [Guglielmo et al. (2015), Paccagnella et al. (2016)]. The mechanisms that drive changes in these galaxies might depend not only on cluster properties but also on the galaxy stellar mass [Fraser-McKelvie et al. (2018a)]. Low-mass spirals are quenched via gas stripping and heating processes operating in rich clusters. It has been suggested that for high-mass spirals there is not a privileged mechanism, but rather a mixture of all processes [Fraser-McKelvie et al. (2018b)]. Cava et al. (2017) analyzed a large sample of galaxies in clusters and concluded that late-types are a recently accreted population; in time, they will change not only their morphology but their phase-space distribution as well, approaching that of cluster earlier types.

Throughout this work, we make a distinction between "local" and "large-scale" (global) environments. By local, we refer to the space immediately surrounding the galaxies, and we quantify it through the galaxy number density. Conversely, the large-scale environment denotes the structure to which a galaxy belongs, such as a cluster, a group, or the field; we characterize it by the cluster mass and the cluster membership, or lack thereof.

1.2 STELLAR PROPERTIES

It is nowadays well accepted that galaxy evolution strongly depends on stellar mass and that properties such as color, SFR, and internal structure are correlated with it [e. g., Kauffmann et al. (2003a), Kauffmann et al. (2004), Mannucci et al. (2010), Kelvin et al. (2014)]. Galaxies follow well-defined relations, such as between color and magnitude [e. g., Baldry et al. (2004)], color and mass, SFR and stellar mass [e. g., Kauffmann et al. (2003a), Paccagnella et al. (2016)], mass and metallicity [established by Lequeux et al. (1979), and studied, among others, by Tremonti et al. (2004)]. They also follow relations with the environment, such as between galaxy morphology and local density [e. g., Dressler (1980)], and between morphology and clustercentric radius [e. g., Goto et al. (2004)].

In general, the color–magnitude relation displays a bimodal distribution, with a tight region of red galaxies (the red sequence), most of them early types with a reduced/quenched star formation, and a loose distribution (the blue sequence), mostly constituted by SF, late-type, galaxies. In between these two regions, a smaller

number of galaxies is found in the so-called "green valley" [Martin et al. (2007)]. This contains mostly galaxies with reduced star formation (compared with SF galaxies of the same mass). The green valley is considered a transition phase for galaxies going from blue/SF to red/quiescent, in a relatively rapid timescale [< 1 Gyr; Salim (2014), Schawinski et al. (2014)].

From observations, a general consensus has been built about the dependence of SFR on stellar mass, with higher SFRs found in more massive galaxies [Peng et al. (2010), Paccagnella et al. (2016)]. This is known as the main sequence (MS). Lagana & Ulmer (2018) confirm a universal MS in cluster galaxies at least since $z \sim 0.9$, and more generally for higher redshifts [$0 < z < 2.5$; Whitaker et al. (2012)]. On the other hand, regarding the specific star formation rate (sSFR), i. e., the SFR normalized by the stellar mass, an anti-correlation is found between the sSFR and the stellar mass, meaning that low-mass galaxies have higher sSFRs than higher-mass galaxies, or that the SFR per unit stellar mass decreases as a function of the stellar mass itself.

The value of both the stellar mass and the colors of galaxies are the result of their star formation history (SFH): the stellar mass mostly depends on the older SFR, while the colors are sensitive to the more recent rates, with dust attenuation and metallicity playing a role as well. Analyzing differences in the SFR as a function of cosmic time can give us clues about the processes regulating these properties. Some investigations [e. g., Wijesinghe et al. (2012)] have failed to find a link between SFR and environmental properties, such as the local density (LD), hence hinting at a predominance of nature over nurture. This is not the case of Gomez et al. (2003), who found an SFR–LD relation. Calvi et al. (2018), studying these relations for field galaxies in the local universe, also determined that, at a given stellar mass, galaxies in low-density environments have systematically higher SFRs than those in denser environments, with a wide spread, which can be explained in terms of morphology. Accordingly, they concluded that processes acting at local scales have a larger effect on galaxy properties than the large-scale environment. Conselice (2006) analyzed a large galaxy sample with $z < 0.05$ and resolved that the most important property determining their physical state is the stellar mass, followed by the SFR and the environment (interactions/mergers). He concluded that these three features should be used to classify galaxies.

Semi-analytic models and hydrodynamical simulations are powerful tools to test galaxy formation and evolution [see Somerville & Davé (2015), for a review]. In these models, cold gas, stars, and dark matter feed galaxies to form stars in episodes. Different physical processes are invoked to stop star formation, such as active galactic nuclei (AGN), stellar feedback, the environment, and morphological transformations. Linking predictions of these simulations to observations is key to understanding the mechanisms that lead galaxies to be quenched [see e. g., Pacifici et al. (2016), and references therein]. Perhaps more importantly, simulations allow us to follow

evolution through time and, hence, to trace progenitors; observations, on the other hand, are snapshots at particular times.

1.3 STAR FORMATION HISTORY

A SFH shows how stars are formed through cosmic time until today. Studying the present SFR and the past SFH helps to describe and understand galaxy evolution. A key issue when studying galaxy formation and evolution is how galaxies form stars, as a function of their stellar masses. The general scenario accepted nowadays for galaxy formation and evolution is known as "downsizing" [Cowie et al. (1996), Neistein et al. (2006)]. This means that more massive galaxies, which are currently observed mostly as early types, formed the bulk of their stars in the past, whereas low-mass galaxies are typically late types and have younger stars. Pérez-González et al. (2008) studied the stellar mass content of the universe at $0 < z < 4$ using infrared (IR) data, and found that "downsizing" is observed from this redshift. They also determined that most massive galaxies assemble their stellar content very rapidly (in $1 - 2$ Gyr), beyond $z \sim 3$ and with high sSFRs, while less massive galaxies form half of their stellar mass below $z \sim 1$ and with lower sSFRs.

As far as the build-up of the stellar mass of galaxies is concerned, the cosmic age encompassed by the redshift range $1 < z < 3$ is crucial. As we already mentioned, at $z \sim 3$, galaxies are very actively SF. During $1.5 < z < 2$, the SFR density reaches a peak [Leslie et al. (2020)] and, for this reason, this period is also known as "cosmic noon". Then, it steadily drops across all galaxy populations towards $z = 0$ [e. g., Madau & Dickinson (2014), Khostovan et al. (2015)]. The exhaustion of the gas reservoir and the reduction in the number of galaxy mergers have been proposed as mechanisms to explain galaxy quenching since $z \sim 1$ [Noeske et al. (2007)]. Besides, the SFRs at fixed stellar mass are significantly lower in the present than in the past [Sobral et al. (2014)].

As already mentioned, both internal and environmental factors affect the star formation activity of galaxies. Environment impacts not only the morphology of galaxies but also their gas content. Since the SFH of a galaxy crucially depends on the amount of gas available, any process that removes, adds, or even perturbs the gas is ultimately determining the evolution and the fate of a galaxy, at least as far as its stellar content is concerned. Galaxies are likely to have their star-formation activity quenched if they are massive, or located in dense environments [Kauffmann et al. (2003a)], and the vast majority of quenched galaxies are early types, suggesting that morphological type and quenching of star formation are related. This interdependence between morphology/star formation/environment complicates disentangling the processes that affect galaxies and their evolution.

In an attempt to address this issue, Schawinski et al. (2014) studied the relation between morphology and SFH in low-redshift galaxies, without considering the environment, and found two evolutionary pathways towards quenching: the slow

quenching of late-types through secular evolution, and the fast quenching of early-types through star formation, probably driven by major mergers. A third pathway could be due to weaker interactions that cause an intermediate quenching [Smethurst et al. (2015)].

Other studies [e. g., Liu et al. (2015), Contini et al. (2019)] have also suggested that the fundamental parameter in the quenching of star formation may not be the environment, but rather stellar mass, on which the SFR is strongly dependent. On the other hand, at least at $z \leqslant 0.8$, LD may be more important than the large-scale environment to determine the stellar mass distribution of galaxies, which suggests that galaxy properties are more strongly dependent on local processes [Vulcani et al. (2012)]. Liu et al. (2019) also find that both morphological transformation and quenching of star formation are mainly driven by stellar mass, at least for massive galaxies.

Peng et al. (2010), Cybulski et al. (2014) distinguish between "mass quenching" and "environment quenching". *Mass quenching* drives shutting down in objects that they are born in a massive dark matter halo, which is, in turn, leading their star formation mode: the potential well they are located in facilitates and triggers very intense star formation episodes by which the galaxies quickly increases their stellar mass at the expenses of the gas mass. Most of it is turned into stars in a relatively short amount of time, and this is how their gas reservoir is depleted, hence leaving no more room for other significant star formation episodes. *Environmental quenching* means that star formation is shut off ensuing different environmental mechanisms, which are discussed in better detail in the next section.

1.4 GALAXY EVOLUTION

By galaxy evolution, we refer to changes across cosmic time in stellar population properties, ISM content, and galaxy morphology. This evolution can be driven by both internal and external physical mechanisms. Internal mechanisms include several astrophysical processes, such as star formation activity and the related electromagnetic and mechanical feedback [Kennicutt (1998)]; supernovae explosions [the most important mechanism among those related to stellar evolution; Burrows (2000)]; nuclear activity, in particular, accretion onto a supermassive black hole, and the related release of mechanical and electromagnetic energy [Silk & Ress (1998)]; the structural configuration of the different morphological components, e. g., angular momentum reconfiguration by stellar bars [Debattista & Sellwood (2000)].

External (environmental) mechanisms can also play a major role. Among them, we include the influence of the gravitational potential of the cluster, galaxy–galaxy interactions, and interactions between galaxies and the hot and dense gas of the intracluster medium (ICM) [e. g., Boselli & Gavazzi (2006)]. To explain the evolutionary paths that galaxies follow in clusters, multiple environment-dependent processes have

been identified and proposed in the local universe, such as harassment [Moore et al. (1996)], that consists in repeated high velocity encounters with other galaxies in the cluster; starvation or strangulation [Larson et al. (1980)], which is the removal of the galactic gas halo by the cluster halo during cluster collapse, and leaves a reduced amount of gas to fuel star formation; ram-pressure stripping (RPS) [Gunn & Gott (1972)], i. e., the removal of the cold interstellar gas through high-velocity interactions with the ICM; thermal evaporation [Cowie & Songaila (1977)], which can also strip galaxies of their ISM by heat transference from the hot ICM; preprocessing [Fujita (2004), Mihos et al. (2004)], where the environment of groups or filaments can affect galaxies before they fall into the main cluster; major and minor mergers [Toomre (1977)]; and the overall tidal influence of the cluster [Byrd & Valtonen (1990)].

Ram pressure (RP) is broadly proposed to explain the existence of the so-called "jellyfish" galaxies, the most extreme manifestations of RPS, preferentially triggered by cluster mergers [McPartland et al. (2016)]. These galaxies are characterized by prominent tails, knots, and high SFRs [Poggianti et al. (2017)]. RP is also invoked to explain HI deficiency, truncated SF disks and HI disks, gas tails of HI, CO, and Hα in cluster galaxies.

Several investigations have shown, through both observations [e. g., Park & Hwang (2009), Cao et al. (2016)] and simulations [e. g., Hwang et al. (2018), Patton et al. (2020)], that hydrodynamical/tidal galaxy interactions with nearby companions can enhance (for late–late pairs) or suppress (late–early pairs) the SFR. Minor mergers may induce a similar effect [e. g., Lambas et al. (2012), Kaviraj (2014)]. Interactions among galaxies may be a key piece to understand star formation activity, both at present and in earlier epochs. Finally, cluster mergers can also affect stellar properties in galaxies [Contreras-Santos et al. (2022)].

Jaffé et al. (2015) studied the relaxed cluster A963 ($z = 0.203$), and showed that galaxies lost their gas content in the first passage around the cluster center. There is also a significant fraction of galaxies arriving at the cluster with no gas, as confirmed by a red-sequence in field galaxies. This last result questions the cluster environment role in the gas removal from galaxies, as well as the importance of other mechanisms.

1.5 GALAXY CLUSTERS AT HIGH-Z

It is well-known that galaxies in the local universe possess a lower star formation activity than in the past. In 1980, Butcher & Oemler (1984) were pioneers in the study of galaxy clusters, and showed that the blue galaxy fraction increases from $z = 0$ to $z \sim 0.5$. This is known as the Butcher-Oemler effect. It is now well understood that high-redshift galaxy clusters are characterized by a population of blue, SF spiral galaxies, which is almost absent in the local universe, whereas the fraction of ellipticals remains more or less uniform since $z \sim 1$. At this same redshift, the S0 population is observed to be scarce [Desai et al. (2007), Poggianti et al. (2009)].

Now, different investigations [e. g., Margoniner et al. (2001), Goto et al. (2003)] have demonstrated that the Butcher-Oemler effect depends on cluster properties, such as richness (number of cluster members), sampled clustercentric radius, and adopted galaxy magnitude limit. The Butcher-Oemler effect provides hints about galaxy formation models [Baugh et al. (1996)], and is evidence that both mergers and secular evolution are engaged in the evolution of galaxies. It is one of the most striking examples of evolutionary effects in galaxies within dense environments.

Pacifici et al. (2016) studied SFHs of a sample of quiescent galaxies from the Cosmic Assembly Near-IR Deep Extragalactic Legacy Survey (CANDELS), at $0.2 < z < 2.1$. They concluded that stellar mass is a key factor in galaxy evolution and that low- and high-mass galaxies experiment different quenching mechanisms on different timescales. For earlier ages ($z \sim 2-7$), Reddy et al. (2012) highlights that star formation was inefficient since galaxies were still assembling.

The influence of the environment on galaxy properties at $1 < z < 3$ is still debated. As clusters are just forming at $z > 1$, spotting protoclusters is difficult [Muldrew et al. (2015)]. Also, statistics are poor, since data are lacking, and those available are biased towards high-mass galaxies, where the environment plays a lesser role. Cosmic variance can be significant when estimating galaxy number density in finite volumes at any epoch [see Somerville et al. (2004), Moster et al. (2011), for more details]. Brodwin et al. (2015) noted a large scatter from cluster to cluster, which makes generalizations still harder. In addition, determining cluster memberships at high redshifts is challenging, as well as reliable morphologies, for which high-resolution imaging is needed.

To perform a comparison between high- and low-redshift cluster galaxies, and study the relation between morphological variations and global environment, we need to quantify the morphological evolution as a function of cluster mass. High-redshift studies [Postman et al. (2005), Poggianti et al. (2006)] have revealed that the particular morphological mix depends on the global cluster properties, in particular the X-ray luminosity and the velocity dispersion, both considered good tracers of the cluster mass.

1.6 SUMMARY OF THIS WORK

Leveraging current facilities, in this work we exploit one of the largest, most complete, and most homogeneous databases of cluster galaxies in the local universe: the WIde-field Nearby Galaxy–cluster Survey [WINGS; Fasano et al. (2006)], and its follow-up OmegaWINGS [Gullieuszik et al. (2015)]. The ultimate goal of this work is to establish causal connections between the galactic stellar population properties and the characteristics of the environment in which they are found, and possibly disentangle the relative importance of such characteristics. At the same time, we attempt to qualitatively and quantitatively assess the evolutionary features driven

by clusters (e. g., color, SFR, morphological fraction, SF fraction), and determine which galaxy types are the most affected.

To this end, we perform a "holistic" analysis of the stellar population properties of galaxies in clusters, taking simultaneously into account the main features of the galaxies themselves, i.e., their stellar masses and morphologies, and all the information we have at our disposal about their environment, both local and large scale. In order to ensure self-consistency and homogeneity, this work repeats analyses that have already been partially published, given the differences in the samples between this and previous publications.

The WINGS and OmegaWINGS projects, together with their products, have been formerly presented in several papers. In Chapter 2, we briefly recap all the information on the data, such as the survey, photometry, spectroscopy, redshift, membership, cluster velocity dispersion, as well as morphological classification and completeness of data. We define the environment tracers used in this work: clustercentric projected distance, distance to the closest neighbor galaxy, and LD, and show how these properties were binned. Here, we also present our results regarding the morphological fractions of galaxies, as a function of cluster mass.

As this work heavily relies on the spectrophotometric code SImulatiNg OPtical Spectra wIth Stellar population models (SINOPSIS), we summarize in Chapter 3 the main features of the modeling and its limitations; likewise, we list its main products: stellar ages, stellar masses, and star formation histories. We also describe the setup used on our data.

In Chapter 4, we outline the criteria that have been used to define the final samples of cluster and field galaxies we are exploiting. Then, using these data, we show the well-known morphology–density relation. Next, we present the main characteristics of the cluster and field galaxy samples, divided by morphology: stellar mass distributions; color–magnitude, color–mass, color–LD, color–projected distance diagrams; phase–space diagrams. We define SF galaxies and study their fraction as a function of different tracers of the environment: projected distance, LD, and cluster mass. We also obtain the SFR-mass relation and analyze the distribution of galaxy inclination as a function of stellar mass. Total stellar mass is one of the most important galactic physical properties, both in general and in the context of scaling relations, whereas colors and star formation rates are fundamental for the study of galaxy evolution.

In Chapter 5, we dive into the possible correlations between SFH and environment, simultaneously taking into account galaxy stellar mass and morphology. As a first step, we characterize the SFHs of galaxies in cluster and field environments, while keeping mass and morphology fixed. This comparison allows us to study environmentally–driven differences in the stellar content, focusing on different parameterizations of the environment: clustercentric distance, LD, and closest neighbor morphology. Here, we also try to understand which one of these parameters

affects more the ability to form stars of the recently infalling galaxies. We then approach the issue from another –more global– point of view: we check if and how total cluster mass drives differences in the SFHs of galaxies, in comparison with those in the field.

Following with Chapter 6, we present additional works that have used our stellar population synthesis results. We start with an introduction to the GAs Stripping Phenomena in galaxies with MUSE (GASP) sample of jellyfish galaxies, followed by some results, such as the jellyfish MS and SFHs, compared with our global galaxy sample. The next section is about the impact of stellar bars on galaxy properties, through results such as the barred galaxy fraction as a function of color, stellar mass, and morphology. We also study quenching as a function of the presence of a bar. The last part of this chapter studies morphological fractions and quenching in the galaxies of a sample of both relaxed and post-merger clusters.

Chapter 7 presents the EDisCS, with a summary of the data acquisition, photometry, spectroscopy, redshifts, and cluster properties. We define a high-z galaxy sample for comparison with the low-z WINGS/OmegaWINGS galaxies. The compared properties include morphological fractions, stellar mass distributions, color–magnitude and color–mass diagrams, SF fractions of galaxies as a function of clustercentric distance and cluster velocity dispersion, the main sequence, and SFHs at fixed morphology and stellar mass, and in bins of clustercentric distance.

All the aspects that we have studied somewhat separately in the previous chapters are then combined and analyzed in Chapter 8, where we try to give a self-consistent picture of the different findings. The most important results are highlighted in Chapter 9 for low- and high-redshift, including a brief overview, future work, and publications of this thesis. We include tables of cluster properties in the WINGS/OmegaWINGS (Appendix A) and EDisCS (Appendix B) datasets, and a brief explanation about the bootstrap resampling method (Appendix C).

In this work, to avoid repetitions, we mostly omit the word "projected", when referring to clustercentric distance, LD, and neighbor galaxy distance. However, these three quantities are always measured in projection in the sky. We always refer to the cluster virial radius as R_{200} (defined in subsection 2.1.4), and to the virial radius of galaxies as R_{vir} (defined in subsection 2.2.2). We assume a Chabrier (2003) IMF, and a ΛCDM cosmological model with $\Omega_m = 0.3$, $\Omega_\Lambda = 0.7$, and $H_0 = 70$ km s^{-1} Mpc^{-1}.

Part II

DATASET AND SPECTROPHOTOMETRIC CODE

2

DATASET

Here, we briefly recall the properties of the data we have used in this work. A more complete and detailed description can be found in previously published works, to which we refer in the following.

2.1 THE WINGS AND OMEGAWINGS SURVEYS

The WIde-field Nearby Galaxy–cluster Survey (WINGS) is a targeted survey of a collection of galaxy clusters, designed to provide a complete and homogeneous observational dataset, to allow a systematic study of the environment, the cluster properties, and the galaxies in them, in a low redshift ($0.04 < z < 0.07$) sample. This was selected from the ROentgen SATellite (ROSAT) Brightest Cluster Sample [BCS; Ebeling et al. (1998)], its extension in the northern hemisphere [eBCS; Ebeling et al. (2000)], and the X-ray Brightest Abell-type cluster sample in the southern hemisphere [XBACs; Ebeling et al. (1996)]. The sample was conceived as a reference for subsequent evolutionary studies and investigations at higher redshifts.

The original WINGS sample [Fasano et al. (2006)] includes 77 clusters (41 in the southern hemisphere and 36 in the northern hemisphere; see Figure 2.1), selected to span a wide range in both X-ray luminosity ($\log L_X$ / (erg· s^{-1}) [0.1 − 2.4 keV] = 43.2 − 44.7) and velocity dispersion ($\sigma_{cl} \sim 400 - 1400$ km s^{-1}). The catalog is uncontaminated by non-cluster X-ray sources, like AGN or foreground stars.

Photometric data in the optical B and V bands of galaxies and stars in the field of the 77 clusters [Varela et al. (2009)], as well as morphological information of the brighter galaxies [Fasano et al. (2012)], constitute the core of the project. A subsample of 48 clusters was chosen to perform a multi-fiber survey of galaxy spectra [Cava et al. (2009)]. A follow-up imaging survey ensued for 28 clusters in the near-IR J and K bands [17 were observed in both filters; Valentinuzzi et al. (2009)], and for 17 clusters in the ultraviolet U band [Omizzolo et al. (2014)]. The database in the U band was recently enlarged to contain 39 clusters [D'Onofrio et al. (2020)].

WINGS was initially planned to cover the innermost regions of the clusters ($34' \times 34'$, or about half a virial radius). It was extended later on, through its photometric follow-up OmegaWINGS, also in the B and V bands, to observe up to 2.5 virial radii of 46 clusters in 45 fields from the original WINGS cluster sample [Gullieuszik et al. (2015)]. A subsequent spectroscopic campaign followed for 33 OmegaWINGS clusters

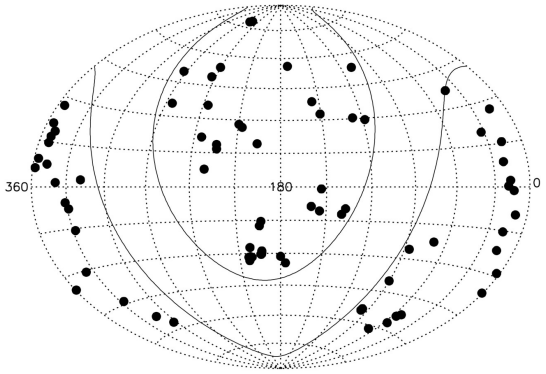

Figure 2.1: All-sky map of the WINGS clusters in equatorial coordinates. Solid black lines delimit the galactic plane ($|b| < 20$ deg), which was excluded in the cluster sample. Image taken from Fasano et al. (2006).

[Moretti et al. (2017)]. Table A.1 (see Appendix A) lists the WINGS cluster sample with some basic properties.

2.1.1 *Photometry*

Source extraction and photometry were performed using `SExtractor` [Bertin & Arnouts (1996)], with a detection threshold of 1.5σ above the background. The detected objects were classified into galaxy, star, or unknown, following the stellarity index `CLASS_STAR`. Additionally, the classification was tested using different combinations of parameters, such as magnitudes at different radii, isophotal areas, and full width at half maximum (FWHM). In diagrams of several of these combinations, segregation between stars and galaxies is found. Outliers were visually checked. In the end, the degree of misclassification by `SExtractor` was less than 1% for stars/galaxies brighter than $V \sim 22$ mag [Varela et al. (2009)]. The final number of objects includes only those detected both in the V and B bands. For WINGS, the photometric catalog comprises $\sim 394,280$ galaxies, 90% complete at $V \sim 21.7$ and 50% at $V \sim 23.2$ [Varela et al. (2009)]. In the case of OmegaWINGS, 195,756 objects were classified as galaxies, with a completeness of 80% at $V = 22.4$ and 50% at $V = 23.1$ [Gullieuszik et al. (2015)].

2.1.2 *Spectra*

The galaxies targeted with spectroscopy were selected from the photometric catalogs to have a total magnitude $V < 20$, a magnitude within the fiber aperture $V_{\rm fib} < 21.5$ (although it is fainter in a few cases), and a color $(B-V)_{5\ \rm kpc} \lesssim 1.4$ within a 5 kpc aperture, with small variations depending on the cluster redshift. These magnitudes and colors have been corrected for extinction by dust in the Milky Way, and the

selection limits were applied to avoid any bias in the observed galaxy type, as occurs when choices are made based on the color-magnitude diagram only [which mainly selects red galaxies; Cava et al. (2009)].

Three sets of spectra are available in the WINGS/OmegaWINGS survey:

- ★ WINGS north (WHT+AF2/WYFFOS);
- ★ WINGS south (AAT+2dF);
- ★ OmegaWINGS (AAT+AAOmega).

We describe them all here. In brief, the original WINGS spectroscopy dataset [Varela et al. (2009)] contains 22 clusters in the south and 26 in the north. WINGS north spectra cover a wavelength range of $\lambda \sim 3800 - 7000$ Å, with a resolution FWHM $= 3 - 6$ Å and a fiber aperture of $1\farcs6$. WINGS south spectra have a resolution of FWHM = 9 Å, a fiber diameter of $2\farcs0$, and cover a range $\lambda \sim 3600 - 8000$ Å. As for OmegaWINGS spectra [Moretti et al. (2017)], they have a FWHM of $3.5 - 6$ Å and a fiber diameter of $2\farcs16$. OmegaWINGS spectra were observed in two sections of the optical range, which could not be put together coherently (Moretti A., private communication). Therefore, we used the blue branch of the spectrum between $\sim 3800 - 5800$ Å to run the spectrophotometric code (see Chapter 3, similar to the method developed by Kauffmann et al. (2003a). Besides, we highlight the use of the V-band magnitude and the equivalent width (EW) of the Hα line (previously measured from the red branch of the spectrum).

The reader can consult the already mentioned references for more details about the instruments, spectra acquisition, and other observational details. The total number of galaxy spectra observed in the field-of-view of these clusters, i. e., the full dataset, is 6,137 in 48 clusters for WINGS, and 17,985 in 33 clusters for OmegaWINGS.

A quality check assessment, based on the signal-to-noise ratio (SNR), made us discard 19 clusters from the northern sky. Hence, for the WINGS north set, we only use 7 clusters: A376, A1795, A1983, A2457, A2626, Z8338, and Z8852. For the southern sky, we use all 22 clusters observed in WINGS south, and all 33 clusters in OmegaWINGS, as well.

Summarizing, in this work, we utilize 3,097 spectra of individual galaxies from WINGS, and to all 17,985 spectra from OmegaWINGS (including 811 galaxies observed in both), in a total of 43 clusters (see Table A.1).

2.1.3 *Redshift and membership*

The redshift measurements were made by Cava et al. (2009) for WINGS and Moretti et al. (2017) for OmegaWINGS, with a method based on the IRAF[1] XCSAO task [Kurtz et al. (1992)] in the RVSAO package, developed to calculate radial velocities using emission line fitting and cross-correlation techniques. Each measurement was corrected to the heliocentric velocity; the typical error in the radial velocities is ~ 25 km s^{-1}.

To determine cluster membership, firstly mean cluster redshift, z_{cl}, is estimated from a redshift histogram. Galaxies outside $z_{cl} \pm 0.015$ (~ 4000 km s^{-1}) are excluded from further analysis. An iterative $\pm 3\sigma$ clipping algorithm [Beers et al. (1990)] is then applied, iterating z_{cl} and σ_{cl} until they converge. This method is widely used [e. g., Milvang-Jensen et al. (2008)], and has been demonstrated to determine cluster membership effectively [Wojtak et al. (2007)], although it may include interlopers at large clustercentric distances [Oman & Hudson (2016)]. On average, cluster velocity dispersions are obtained with up to three times more member galaxies than previous studies [e. g., the Sloan Digital Sky Survey (SDSS)].

As shown in Figure 2.2, for WINGS, 6,137 redshifts were obtained, of which 3,647 were tagged as cluster members; for OmegaWINGS 17,985 redshifts were measured, and the number of cluster members is 7,497. Four clusters in OmegaWINGS (A1069, A2382, A3158, and A4059) have a second group of galaxies outside the main group (with radial velocities more than ± 3 times the cluster velocity dispersion away from the cluster systemic velocity). In these cases, the galaxies in the second group were also included as cluster members (see galaxy sample selection in Section 4.1). Besides, many of the clusters present infalling structures (Lourenço et al., submitted).

Finally, given the membership and SNR of spectra, we use here 2,711 galaxies in WINGS and 7,627 in OmegaWINGS to construct the final cluster member sample. From the non-cluster member dataset, we build the field galaxy sample (see Section 4.1).

2.1.4 *Cluster velocity dispersion*

We take R_{200} as the cluster virial radius. Following Finn et al. (2005), it is calculated from the cluster velocity dispersion, σ_{cl}, and the mean redshift of all cluster members, z_{cl}, as follows:

$$R_{200} = 1.73 \, \frac{\sigma_{cl}}{1000 \text{ km s}^{-1}} \, \frac{1}{\sqrt{\Omega_\Lambda + \Omega_m (1+z_{cl})^3}} \, h^{-1} \text{ Mpc}. \tag{2.1}$$

1 IRAF is distributed by the National Optical Astronomy Observatories, which are operated by the Association of Universities for Research in Astronomy, Inc. (AURA), under a cooperative agreement with the National Science Foundation.

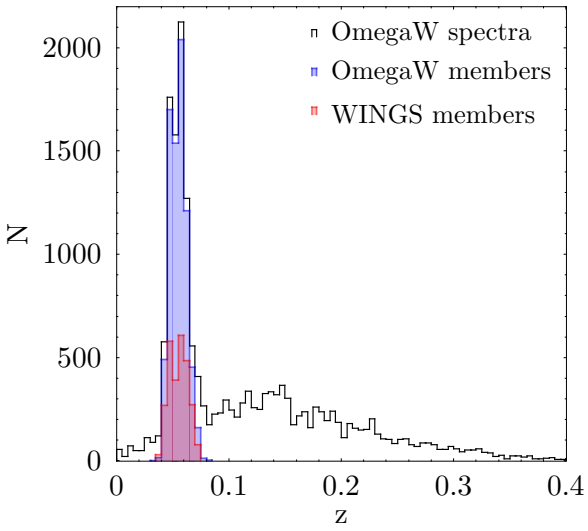

Figure 2.2: Redshift distribution of objects. *Empty histogram:* all OmegaWINGS spectra; *blue histogram:* cluster members in OmegaWINGS; *red histogram:* cluster members observed only in WINGS. Image adapted from Moretti et al. (2017).

This is the radius at which the enclosed mean mass density exceeds the critical density of the universe by a factor of 200 [Peebles (1993)]. The velocity dispersion values span a range of $\sigma \simeq 400 - 1300$ km s^{-1} (see Table A.1 in Appendix A). WINGS clusters fields were chosen to observe at least up to 0.6 R_{200}, while OmegaWINGS fields reach at least the virial radius, and for some cases even almost to 2.5 R_{200}, where there still exist cluster members. We use the updated R_{200} and σ_{cl} values given by Biviano et al. (2017) and Gullieuszik et al. (2020) for each cluster.

2.1.5 *Morphology*

The study of the morphological fractions and their variations in galaxy clusters was one of the most important goals of the WINGS survey. To achieve this, `MORPHOT` [Fasano et al. (2012)] was developed. `MORPHOT` is an automated, non-parametric, tool for the morphological type classification of large galaxy samples. It exploits 21 morphological diagnostics[2], and provides two independent methods to classify galaxies, one semi-analytic technique based on maximum likelihood (ML), and another leveraging a neural network (NN) machine. A sample of ~ 1,000 galaxies is visually classified and used to calibrate the ML diagnostics and train the NN machine. The diagnostics are limited to be image-based, excluding color and spectroscopic

2 These diagnostics are, among others, Sérsic index, luminosity concentration index, asymmetry, clumpiness.

quantities. This is done to avoid biases when studying galaxy evolution in clusters, separating morphology from stellar populations.

The final classification is based on a combination of these two techniques, i. e., NN and ML. MORPHOT has proven to be effective through a comparison with ~ 3,000 randomly selected and visually classified galaxies from WINGS, and with another ~ 1,000 from SDSS. In all cases, the results obtained are consistent. The reader is referred to Fasano et al. (2012) for technical details. MORPHOT can differentiate between elliptical and lenticular galaxies with unprecedented accuracy, making the morphological classification highly reliable. The classification uses a slightly modified version of the Revised Hubble Type (T_{RH}), denoted by T_M (MORPHOT type).

For this work, we will use four main morphological classes:

- ✯ Ellipticals (E): $-5.5 < T_M < -4.25$;
- ✯ Lenticulars (S0): $-4.25 \leqslant T_M \leqslant 0$;
- ✯ Early spirals (SpE): $0 < T_M \leqslant 4$;
- ✯ Late spirals and irregulars (SpL): $4 < T_M \leqslant 11$.

The SpE class roughly includes galaxies with Sa to Sb morphology, while the SpL category includes all galaxies with Sc and later types. Sometimes, when required (e.g., for comparison to other works), we use a broad classification: early types (i.e., ellipticals and S0s) and late types (i.e., early spirals, late spirals, and irregulars). We exclude cD[3] galaxies ($-6.0 \leqslant T_M < -5.5$) throughout this work, because the formation and evolution of cD galaxies are different from those of "normal" ellipticals. In the formation theory of cD galaxies, we find, e. g., tidal stripping (accretion of matter from neighbor cluster members), minor and major mergers, and primordial origin [Tovmassian & Andernach (2012), Pérez-Hernández et al. (2022)]. Besides, there are only 21 cD galaxies in all the WINGS+OmegaWINGS cluster member dataset.

A morphological classification is provided for 39,923 galaxies in WINGS [Fasano et al. (2012)], and for 49,883 galaxies in OmegaWINGS [Vulcani et al. (2023b)]. Stellar mass distributions are studied in Section 4.3, once the galaxy sample is defined. Stellar mass is obtained using the SINOPSIS code, as explained in Section 3.3.

3 The name cD is now interpreted as central/cluster dominant, but this is not its original meaning. The "D" was introduced by Morgan (1958) for ellipticals with outer halos and shallow brightness gradients, i.e., for diffuse objects, and the prefix "c" was given to very large galaxies in his classification. See Bender et al. (2015) for more information.

2.1.6 *Completeness*

For this work, we have used several properties, both observed and computed, to characterize the evolutionary status, the environment, and the physical characteristics of the galaxies in our sample.

Not all galaxies detected in the images (see subsection 2.1.1) have a spectroscopic counterpart, because of two reasons. First, the number of fibers in the spectrometers is limited and, due to the physical size of the fibers, they cannot overlap to cover the densest part of clusters, typically towards the center, where the highest number of galaxies is located. The second reason is that observing time is limited, and brighter galaxies are more easily observed. Neglecting these two facts might lead to wrong conclusions when analyzing the properties of galaxies as a function of their (projected) position in the cluster and of their luminosity. These two considerations bear on the radial (geometrical) completeness, $C(r)$, and on the completeness as a function of magnitude, $C(m)$, respectively [see Cava et al. (2009), for more details].

We take into account these two limitations of the survey through the spectroscopic completeness, i.e., by weighting the properties of each galaxy with:

$$W(m, r) = \frac{1}{C(m) \times C(r)}. \tag{2.2}$$

2.2 ENVIRONMENTAL TRACERS

We use three parameterizations of the cluster environment for the member galaxies: the projected distance to the cluster center, the projected LD, and the projected distance to the nearest confirmed spectroscopic member galaxy.

2.2.1 *Clustercentric (projected) distances*

We analyze the properties of galaxies as a function of their projected distances to the cluster center, considering two different center definitions: the BCG, and the maximum intensity of the X-ray emission. For most WINGS clusters, these two positions coincide, but 13/77 WINGS clusters have two cD galaxies. For those, we take as the cluster center the optical position of the peak in the X-ray emission, updated by Biviano et al. (2017). Clustercentric distance, from spherical trigonometry, is given by:

$$\theta = \cos^{-1}\left[\sin\delta_g \sin\delta_c + \cos\delta_g \cos\delta_c \cos(\alpha_g - \alpha_c)\right], \tag{2.3}$$

with the subscripts g for galaxy, and c for the cluster center. Then, using the cluster redshift (the mean redshift of cluster member galaxies), this projected distance is converted into a linear distance, in units of Mpc and R_{200} of the cluster [Biviano et al. (2017)].

2.2.2 *(Projected) distance to the closest neighbor galaxy*

Here, we use only spectroscopically confirmed cluster members. For each galaxy, we choose the closest neighboring galaxy in projection. The virial radius of the neighbor galaxy is then calculated. This is the radius of a sphere whose density of baryonic matter [approximated by only taking into account the stellar mass ($\mathcal{M}_*$) obtained through SINOPSIS; see Section 3.3 below] is equal to 200 times the critical density of the universe at that redshift:

$$R_{vir} = \left(\frac{3}{4\pi} \cdot \frac{M_\star}{200\rho_c} \right)^{1/3}. \tag{2.4}$$

The distance to the closest galaxy is normalized by this virial radius ($R_{vir,\ neigh}$) of the neighbor galaxy. This approach to obtaining the virial radius of galaxies is similar to that of other works, e. g., Park & Choi (2009), Park & Hwang (2009).

2.2.3 *Local density*

Galaxy LD has an important role in studying many galaxy properties, such as SFR, morphology, color, and gas content, as well as the physical processes involved in galaxy evolution in several environments. The projected LD is defined as:

$$\Sigma_N = \frac{N}{A}, \tag{2.5}$$

or the number of galaxies per unit of circular area $A = \pi R_N^2$ (Mpc^2). This is the area in the sky enclosing the N nearest projected neighbors brighter than a certain absolute magnitude limit, corrected for spectroscopic incompleteness. For the high galaxy densities found in clusters, N is taken as 10 [Vulcani et al. (2012)], i. e., we use Σ_{10}, while for the field N can be 5 [Baldry et al. (2004)]. Given the lack of spectroscopy for all galaxies, a limit in luminosity is imposed to eliminate background galaxies (in this case, $M_V = -19.5$), as well as an additional statistical correction to account for field galaxy contamination, using the counts obtained by [Berta et al. (2006)]. We take advantage of the LD values already published for WINGS by Moretti et al. (2014), and for OmegaWINGS by Vulcani et al. (2023b). We have 9,278 individual galaxies (22,110 weighted objects) with measured properties and, from these, 8,512 (21,086 weighted objects) include LD values.

2.2.4 *Binning*

In Figure 2.3, we show the distribution of LD as a function of projected distance to the cluster center, and projected distance to the closest neighbor galaxy, separated

into the four main morphological classes used for the cluster galaxy sample. We also highlight the bins used to divide galaxies according to the three environment tracers used throughout the text (i. e., LD, clustercentric distance, and distance to the closest neighbor); the bins are indicated with horizontal and vertical dotted lines.

In the left panels, we have that LDs drop when clustercentric distances increase, for all types, with a large dispersion at large distances and low densities. Early types are more concentrated close to the cluster center and at high densities, while galaxies of all types reach large distances. Note that there are a few galaxies at $R/R_{200} > 2$, for all types. Later, in Figure 4.10, we display the averages of LD and R/R_{200} by morphological type. The right panels of Figure 2.3 show that there is no correlation between LD and distance to the closest neighbor.

2.3 FRACTIONS OF MORPHOLOGICAL TYPES WITH CLUSTER MASS

One of the main goals of the WINGS survey was to study the fractions of morphological types in nearby clusters, as a function of cluster mass proxies, such as the velocity dispersion (σ_{cl}) and X-ray luminosity (L_X). We remind the reader that these properties are proxies of cluster mass only for virialized clusters, which is not the case for all WINGS clusters (Lourenço et al., submitted). We can still use σ_{cl} to estimate the mass of clusters that are not virialized, although it will be overestimated for clusters with substructure [Miller et al. (2005)]. Following Finn et al. (2005), and using the virial mass to relate the cluster mass with the velocity dispersion and the virial radius, we obtain the expression:

$$M_{cl} = 1.2 \times 10^{15} \left(\frac{\sigma_{cl}}{1000 \text{ km s}^{-1}}\right)^3 \frac{1}{\sqrt{\Omega_\Lambda + \Omega_m (1+z_{cl})^3}} \, h_{100}^{-1} \, M_\odot, \tag{2.6}$$

whose parameters were explained in subsection 2.1.4. The relation between M_{cl} and L_X is not straightforward, but we refer to Pratt et al. (2009), Stanek et al. (2006), Schneider (2006), for the proportionality between L_X, X-ray temperature, and cluster virial mass.

This analysis was performed by Poggianti et al. (2009) using only bright ($M_V \leqslant -19.5$) cluster galaxies in WINGS, i. e., galaxies within 0.6 R_{200}. The result revealed a lack of correlation of the three main morphological classes (ellipticals, S0s, and spirals) with σ_{cl}, and a weak dependence of the spiral fraction on L_X, when both σ_{cl} and L_X are used indistinctly as proxies of cluster mass. Here, we extend the analysis to the clusters observed in OmegaWINGS and thus include all cluster member galaxies within one projected R_{200}. In the following, we gather the galaxies in the three broad morphological classes already mentioned.

Figure 2.4 shows the fractions of morphological types as a function of cluster velocity dispersion. Solid lines are the least-square fits, with a low correlation

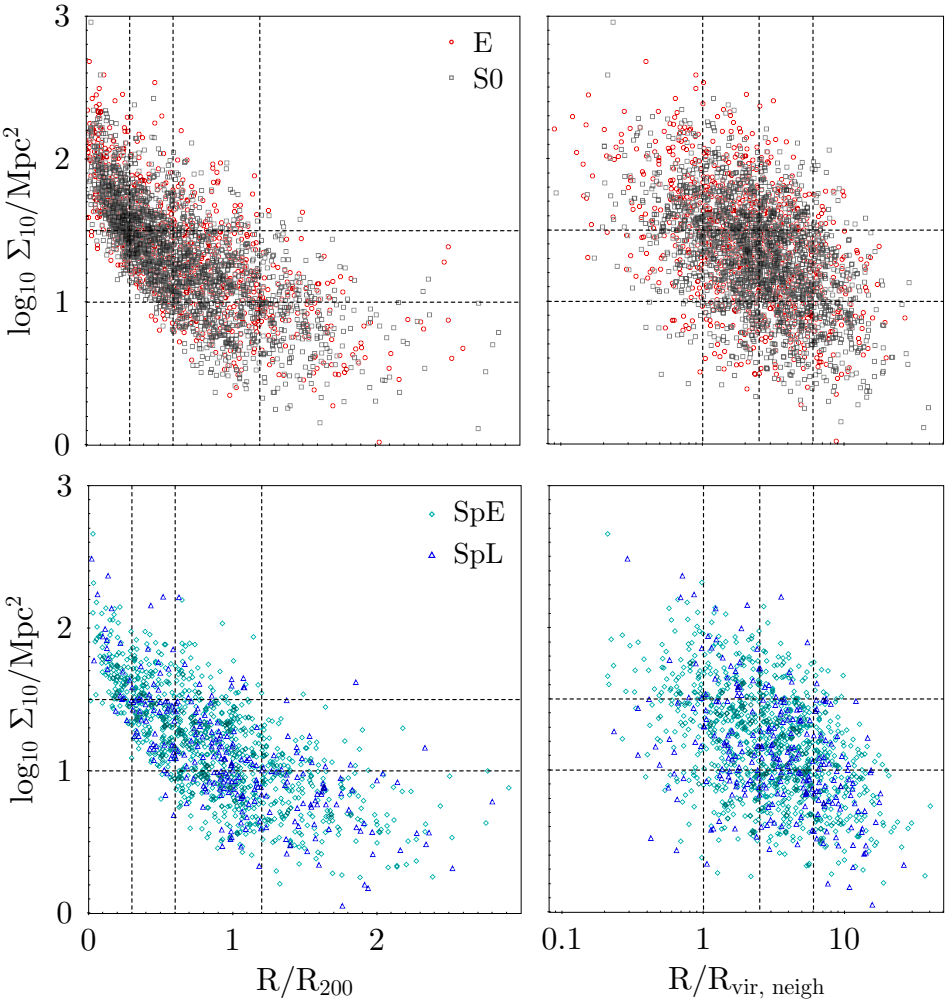

Figure 2.3: LD *versus* clustercentric distance (*left column*), and *versus* distance to the nearest neighbor galaxy (*right column*), for early- (*top row*) and late- (*bottom row*) types in the cluster galaxy sample. Horizontal and vertical dotted black lines indicate the bins used to divide the sample. Early-type galaxies are more concentrated at higher densities and toward the cluster center.

coefficient[4] in all cases: 0.14 for ellipticals, 0.21 for S0s, and −0.21 for spirals. Conversely, Poggianti et al. (2009) do not find correlations for any type. The trends of morphological fraction as a function of X-ray luminosity are shown in Figure 2.5, together with the least-square fits. We also find low correlations: 0.34 for S0s, −0.26 for spirals, and 0.05 for ellipticals. Taking into account the binomial error bars in the fractions, and the errors in the σ_{cl} of clusters, these results indicate that the fractions of S0s and spirals correlate weakly with σ_{cl} and L_X. For ellipticals, there is no correlation,

4 Pearson's correlation coefficient is a measure of the statistical relation between two variables. It gives information about the magnitude of association, and the direction of the relation.

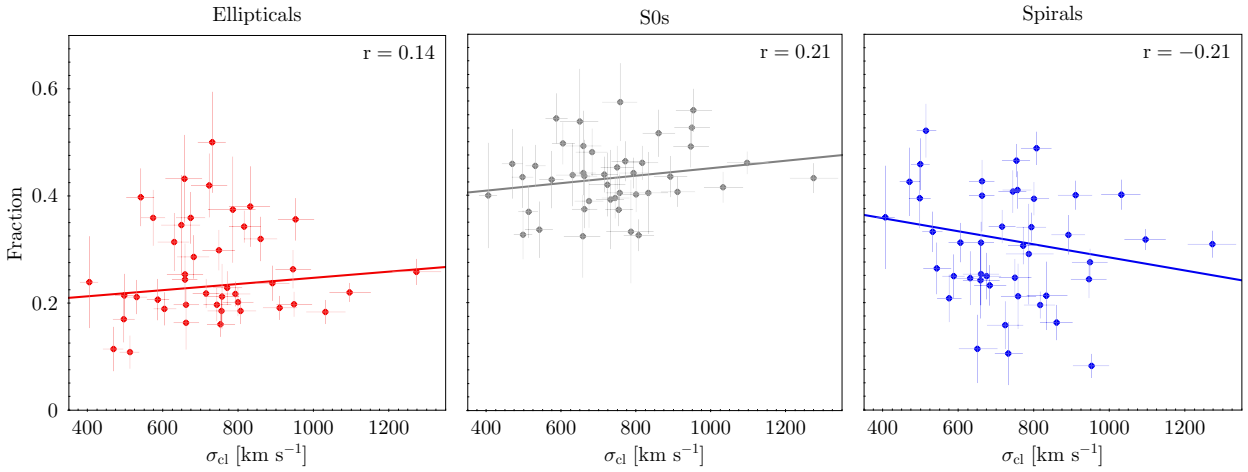

Figure 2.4: Fractions of galaxy morphological types in the WINGS and OmegaWINGS datasets, as a function of cluster velocity dispersion (σ_{cl}): ellipticals (*left*), S0s (*middle*), and spirals (*right*). The error bars for the fractions are binomial. The least-square fits, weighted by the errors, are shown as a solid straight line in each panel. The *r* value corresponds to Pearson's correlation coefficient. There is a weak correlation between the fraction of both S0s and spirals with σ_{cl}, while Poggianti et al. (2009) do not find correlations for any type.

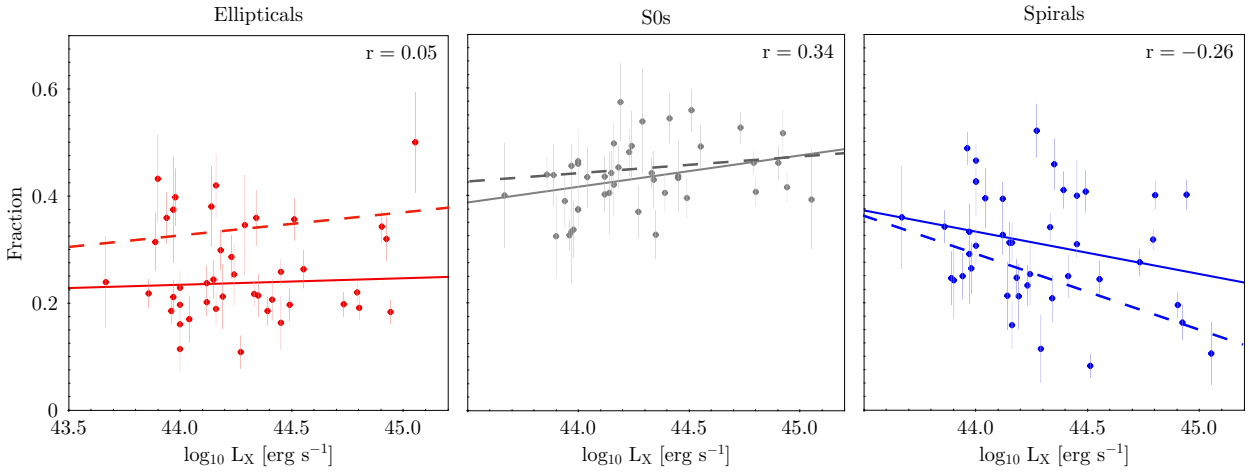

Figure 2.5: Fractions of galaxy morphological types in the WINGS and OmegaWINGS datasets, as a function of cluster X-ray luminosity (L_X). Panels as in Figure 2.4. There is a weak correlation between the fraction of both S0s and spirals with L_X. Dashed lines represent the least-square fits obtained by Poggianti et al. (2009).

either with σ_{cl} or with L_X. In this case, Poggianti et al. (2009) obtain that the fraction of spirals is inversely correlated with L_X, with a Spearman probability of 99.6%.

Table 2.1: Morphological fractions of cluster members (up to 1 R_{200}) and field galaxies in the WINGS/OmegaWINGS dataset. The last column lists the fractions reported by Poggianti et al. (2009), only for WINGS galaxies (see text). Errors are binomial

.

Type	Clusters	Field	Clusters (Poggianti+, 2009)
E	$26.0 \pm 4.3\%$	$14.7 \pm 0.9\%$	$33 \pm 7\%$
S0	$43.5 \pm 4.9\%$	$25.8 \pm 1.1\%$	$44 \pm 10\%$
SpE	$23.2 \pm 4.1\%$	$35.2 \pm 1.2\%$	–
SpL	$7.3 \pm 2.0\%$	$24.3 \pm 1.1\%$	–
Sp	$30.5 \pm 4.3\%$	$59.5 \pm 1.2\%$	$23 \pm 9\%$

In Table 2.1, we list the mean morphological fractions of clusters and the field, compared to the results obtained by Poggianti et al. (2009). Our fraction of spiral galaxies is higher, at the expense of lower elliptical and S0 fractions. We also find that, while the S0 fraction increases with cluster mass, the opposite is true for spirals. We attribute these results to the inclusion of OmegaWINGS data in our analysis and the exclusion of non-cluster members. The OmegaWINGS survey samples the galaxy populations located far from the cluster centers: these galaxies have not been yet affected by the cluster environment, or are still undergoing morphological changes. Sampling larger cluster areas allows for the inclusion of regions where transformations are ongoing or happened recently, while most early types would be dynamically settled toward the cluster center. The comparison between this work and Poggianti et al. (2009) could also be telling us that morphological transformations are slower in less massive galaxies.

What we can conclude from this simple analysis is that, when we characterize clusters by their total mass, differences can be found in the morphological fractions: these can be due either to the existence of large-scale effects or to the combination of multiple local mechanisms.

3

THE SPECTROPHOTOMETRIC CODE

One of the goals of the WINGS project is the study of stellar population properties in cluster galaxies, and the influence of the environment on their characteristics. For this purpose, a stellar population synthesis code was developed to derive SFHs based on previous work by Poggianti et al. (2001). Here, we will briefly describe the SImulatiNg OPtical Spectra wIth Stellar population models (SINOPSIS) code[1] [Fritz et al. (2007), Fritz et al. (2011)], and its results. SINOPSIS is a spectrophotometric fitting code that can recover the characteristics of the stellar populations of galaxies, such as their SFR, SFH, mean stellar ages, stellar mass, dust extinction, among others.

3.1 THE CODE

SINOPSIS aims to reconstruct the SFH of galaxies, by reproducing the main features of the observed spectrum: the EW of the most significant emission and absorption lines: Hα, Hβ, Hδ, Hϵ+CaII (H), CaII (K), Hη, and [OII] [Fritz et al. (2007)], and the continuum flux, measured in particular regions to avoid any notable spectral line. A model spectrum is obtained by adding synthetic spectra of simple stellar populations (SSPs) of different ages. Before summing the simple stellar population (SSP)s, extinction is applied to simulate dust distributed in a uniform screen located in front of the stars. The final synthetic spectrum model flux F_{mod} will have the form:

$$F_{mod}(\lambda) = \frac{1}{4\pi d^2} \sum_{i=1}^{N} M_i \, L_i(\lambda) \, 10^{-0.4 \, A(\lambda) \, R_V \, E(B-V)_i}, \tag{3.1}$$

where the sum is carried out over the number of SSPs used by the code (see Section 3.2 below); d is the luminosity distance to the galaxy; M_i and $L_i(\lambda)$ are the stellar mass and the spectrum (in units of luminosity per solar mass units) for the ith SSP, respectively; and the function in the exponent represents the extinction ($A(\lambda)$, normalized to the V band; R_V is the total-to-selective extinction ratio ($R_V = A_V/(A_B - A_V)$); and $E(B-V)_i$ is the color excess). The free parameters used in the fitting are the color excess and the mass (or, equivalently, the SFR: one value for each

1 http://www.irya.unam.mx/gente/j.fritz/JFhp/SINOPSIS.html

SSP age). SINOPSIS considers "selective extinction" [Calzetti et al. (1994)], in which each SSP has its own value of dust attenuation. The younger the stellar population is, the more likely it is located in a region with more extinction [i.e., in the molecular clouds where it was born; Charlot & Fall (2000), Poggianti et al. (2001)]. For this reason, generally, dust extinction is higher for younger stellar populations.

SINOPSIS assumes that all the stellar populations in a galaxy have the same metallicity value at any age. Then, the code compares the observed spectrum, corrected for extinction from the Milky Way, with synthetic spectra that explore the parameter space to find the combination of metallicity, mass, and extinction that best reproduces the observed spectrum, i.e., the best fit, assessed through the minimization of the standard χ^2 function (see Section 3.5).

It should be noted that, in many cases, good fits are obtained with two or more values of the metallicity, but the code chooses the one that yields the lower χ^2, i.e., it assumes that this is the metallicity of the stars that dominate the light in the spectrum. Fritz et al. (2007) roughly simulated chemical evolution, by constructing synthetic spectra with different SFHs, and varying the metallicity as a function of stellar age. Their results clearly show that using a single metallicity to recover total stellar mass and SFH does not introduce any bias.

Since the set of theoretical SSP spectra used spans a wide wavelength range, we can calculate magnitudes in several bands not covered by the observed spectrum. Likewise, K-corrections are automatically carried out by SINOPSIS: while the fit is performed by shifting the spectrum at the observed redshift, absolute magnitudes in various bands can be calculated from the best-fit model at rest frame and put at a distance of 10 pc. Then it is convolved with the transmission curves of the Johnson filters *U*BVRIJHK, and the *ugriz* passbands of the SDSS system, to derive absolute magnitudes.

3.2 STELLAR AGES

The initial set of SSPs contains models for up to 220 different stellar ages, for each of the 13 metallicity values (see Section 3.5). Nevertheless, such a high age resolution is both non practical, when a non-parametric SFH is assumed, and unreliable for the comparison between models and observed data. Well-known degeneracies, like age-metallicity and age-extinction, and the fact that changes in the spectral features are a logarithmic function of age (i.e., the oldest SSPs are very similar) make it practically impossible to find a unique solution with that degree of precision in age. This is why we lower the age resolution, by binning the SSPs into 12 final spectra (that we will keep calling SSPs, for the sake of simplicity). It is true that with these 12 ages, the solution is still non-unique, but the degree of degeneracy is lower. This number of SSPs is enough to reproduce observed data, as demonstrated by Fritz et al. (2007), but see also Fritz et al. (2017).

Table 3.1: Age intervals used in SINOPSIS to obtain the SFHs. Age interval for SFR_1 goes from today to ~ 20 Myr ago; SFR_4 spans the range between 5.75 Gyr ago and t_u, i.e., the age of the universe at the cluster redshift; z_u is the redshift corresponding to t_u.

SFR_i	Age bin	Age bin width	Redshift bin
SFR_1	$0 - 19.95$ Myr	19.95 Myr	$0 - 0.0014$
SFR_2	$19.95 - 571.5$ Myr	551.55 Myr	$0.0014 - 0.0421$
SFR_3	$0.5715 - 5.754$ Gyr	5.183 Gyr	$0.0421 - 0.6071$
SFR_4	$5.754 - t_u$ Gyr	Δt_u Gyr	$0.6071 - z_u$

The task of the code is to find the combination of 24 parameters (12 for the stellar mass and 12 for extinction) that yields the best fit to the observed spectrum, for each of the four chosen metallicity values. This is done with an algorithm that randomly explores the space of parameters, looking for the absolute minimum of χ^2. The code performs 11 optimizations or model fits in the parameter space and obtains error bars for mass and extinction. In practice, a bad fit can be due to low-quality spectra for several reasons: low SNR, bad flux calibration, presence of telluric lines, and bad sky subtraction. Also, the object could be a type 1-AGN [the fraction of AGN in WINGS/OmegaWINGS clusters is approximately 3%; Marziani et al. (2017)] or a star that has been misclassified as a galaxy (in very few cases).

Even with an initial binning in the age of the model spectra, once the best fit is obtained, the solution is far from being unique. Thus, a further binning in age is performed and the resolution is lowered to four age bins. These are listed in Table 3.1, and were selected by both taking into account the general characteristics of SSPs, and by fitting simulated model spectra. For these four ages the SFR, and thus the SFHs, are obtained (see Section 3.4). The age of the oldest stellar population used is set by the age of the universe at the redshift of the cluster (t_u) harboring the galaxy.

3.3 STELLAR MASSES

Fitting the main features of an aperture-integrated optical spectrum allows us to estimate several properties of stellar populations, among which the stellar mass in the aperture is one of the most important. Other properties, such as the total mass of stars as a function of age, mean metallicity, and dust extinction, are also obtained. In order to rescale the aperture mass (M_{fib}) to the total galaxy stellar mass (M_{tot}), we use:

$$M_{tot} = M_{fib}\ 10^{-0.4\ (V_{fib} - V_{tot})}, \tag{3.2}$$

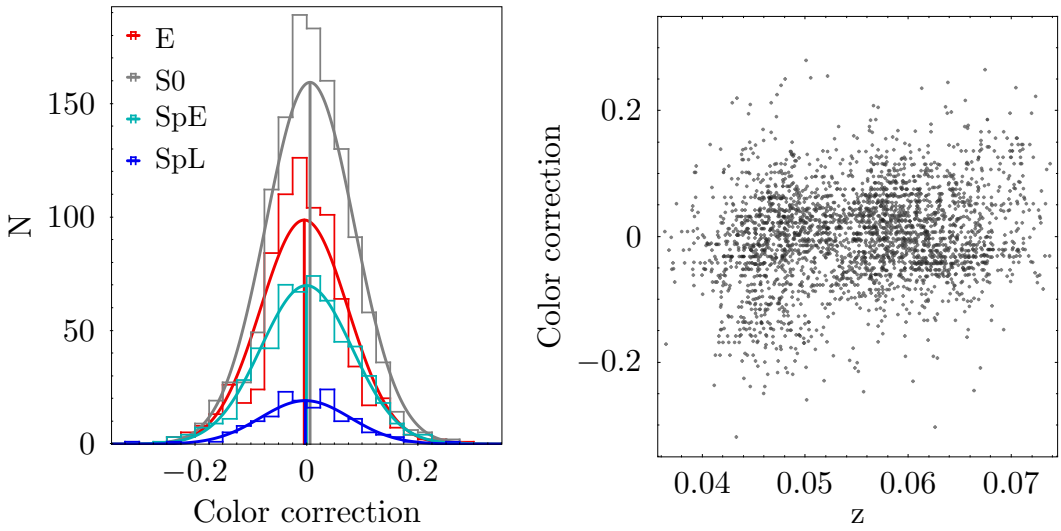

Figure 3.1: *Left:* color corrections of aperture spectra in WINGS cluster galaxies with the four main morphologies (see text). Each type has a normal distribution with mean = zero. *Right:* color corrections versus redshift for all types together; the distribution is flat. Data from Fritz et al. (2011).

where $V_{\rm fib}$ and $V_{\rm tot}$ are the fiber and total V-band magnitudes, respectively. In this formula, we are assuming that the color gradient between the aperture and the whole galaxy is negligible, as done by other authors [e. g., Kauffmann et al. (2003a)].

It is worth mentioning that, ideally, one should use spectra that cover the whole galaxy, but this is out of reach for the present survey. Fritz et al. (2011) made a comparison between the $(B-V)$ colors within the fiber aperture and a 5 kpc aperture; they found that the colors in both apertures are very similar (with a mean difference of $B-V \sim 0.1$ mag), and that the color within a 5 kpc aperture represents a good approximation to the total color of the galaxy for the redshift range in WINGS/OmegaWINGS.

To take into account the possible effect of color gradients on the total mass determination [Brinchmann et al. (2004)], Fritz et al. (2011) computed a correction factor, that considers the color difference when rescaling the aperture mass to the total mass. We plot the distribution of this color correction (Figure 3.1, left panel) and verify that it very closely follows a normal distribution peaking at zero, with a standard deviation of 0.08 magnitudes for all morphologies and the whole galaxy sample. Additionally, we plot the color correction as a function of z (Figure 3.1, right panel); there is no dependence of correction on redshift.

Moreover, as it will be shown in Section 4.5, our galaxy sample uniformly covers the whole range of inclination values, and hence, in many cases, galaxy outskirts are included in the aperture spectrum. We observe no trends of total mass or SFR with inclination (Figure 4.8). Furthermore, Fritz et al. (2011) performed a careful

comparison between masses obtained through SINOPSIS, and those from the SDSS DR4 [Gallazzi et al. (2005)] and the SDSS DR7, using a subsample of objects in common between all surveys. Fritz et al. obtained an excellent agreement, despite the use of different analysis techniques.

Finally, stellar mass values are taken according to definition 2 in Longhetti & Saracco (2009), i. e., the mass contained in stars still in the nuclear burning phase and remnants (white dwarfs, neutron stars, and black holes); hence, stellar mass does not include mass lost due to stellar evolution and supernovae.

3.4 STAR FORMATION HISTORIES

In Section 3.2, we mentioned that the code uses 12 SSPs of different ages to search for the best fitting model and that these 12 ages are binned *a posteriori* into four age intervals, shown in Table 3.1, with which the SFH is properly recovered [Fritz et al. (2011)]. The SFRs for each of the four age ranges are computed by adding up the initial stellar masses contained in the SSPs that constitute the bin, and dividing the result by the bin time length. To calculate the current SFR (in the last $\sim$ 20 Myr, or SFR_1), a fit is performed to the EW of the emission lines, when present: Hα, Hβ, and OII. These lines are entirely attributed to star formation processes, but other mechanisms, happening in both AGN and low-ionization nuclear emission-line region (LINER) galaxies, can produce ionizing flux and cause an overestimate of the current SFR. To mitigate this problem, we impose a cut ($= 6$ Å) on the $\mathrm{EW}_{\mathrm{H}\alpha}$. Several works [e. g., Sánchez et al. (2014), Cid Fernandes et al. (2013)] have demonstrated that lower values can be associated with ionization mechanisms different from star formation. Hence, we assume that a low EW value ($0 < \mathrm{EW}_{\mathrm{H}\alpha} < 6$ Å) is not due to star formation, and in such cases, we always take the present-day SFR as 0. This helps us account for low-luminosity AGN, and for galaxies in which the Hα emission is not dominated by star formation. Although luminous AGN can contaminate the sample of SF galaxies, given their very low numbers ($1 - 2\%$), they likely have a negligible effect on our analysis.

The four age bins in Table 3.1 are defined according to stellar population features [Fritz et al. (2007)], thus:

SFR_1: Characterized by emission lines and the strongest ultraviolet emission.

SFR_2: Hydrogen lines from the Balmer series reach their maximum intensity *in absorption*, while the CaK,H UV lines still have low (almost undetectable) EWs.

SFR_3: Balmer absorption lines decrease in intensity, while the K calcium line reaches its maximum level in absorption.

SFR_4: SSPs in this age bin are reddest, and the main spectral characteristics show an asymptotic behavior. The 4000 Å break (D4000) attains the highest values.

3.5 THE ADOPTED SETUP

Photometric stellar masses (and, more in general, inferred stellar population properties) depend on the choice of different parameters, such as the initial mass function (IMF), metallicity, extinction law, and stellar population models [Marchesini et al. (2009)]. In this respect, SINOPSIS is a quite flexible code that allows the user to define how the fit is to be performed, and easily manipulate the fitting parameters. The setup and parameters used to run the code are described hereafter. We assume a nonparametric prescription for the SFHs, meaning that the SFRs are allowed to vary freely and independently for stellar populations of different ages (as opposed to adopting analytical forms for the SFR as a function of cosmic time). As already mentioned, SINOPSIS utilizes spectra of 12 different ages. These include four spectra in the age range between 0 and $\sim$ 20 Myr, i.e., when stars can significantly ionize the gas and hence produce emission lines.

Fritz et al. (2017) determined that optical nebular lines contribute negligibly to spectra of stellar populations older than $\sim 2 \times 10^7$ yr. The ages between 0 and $\sim 2 \times 10^7$ yr are represented in about 100 (of 220) SSPs (for each value of the metallicity). Fritz et al. (2017) employed the photoionization code `CLOUDY` [Ferland et al. (2013)], assuming physical parameters typical of HII regions [see Fritz et al. (2017), for more details]. To be consistent with this approach, we choose to assign the same SFR to the four youngest SSPs. This hence reduces the number of parameters to 21, instead of 24. In this fashion, we are also able to calculate the recent SFR based on Balmer emission line intensities.

As for the theoretical spectra, we employ the revised version of the Bruzual & Charlot (2003) stellar population synthesis models (C&B models, hereinafter), introduced by Plat et al. (2019). Although the updated models have been used in several recent publications [e.g., González-Delgado et al. (2022), Werle et al. (2022)], a detailed description is still to be published by Charlot & Bruzual (in prep.). The most complete outline is found in Appendix A of Sánchez et al. (2022), from where we summarize here the ingredients of the models.

The C&B models follow the PARSEC (PAdova and tRieste Stellar Evolutionary Code) evolutionary tracks [Marigo et al. (2013), Chen et al. (2015)] for single and non-rotating stars with masses 0.1 $M_\odot$ – 600 $M_\odot$, through small steps of mass and time, and for 16 possible metallicities, from $Z = 0.0000$ to $Z = 0.060$. The tracks cover the evolution from the MS to the thermally pulsing asymptotic giant branch (TP–AGB) for stars with masses < 6 $M_\odot$, and for O and B stars from the MS to the Wolf–Rayet (WR) phase, whose model atmospheres are computed by the Potsdam group (PoWR). The post-AGB evolution of low and intermediate-mass stars follows Miller-Bertolami (2016). The tracks also take into consideration the mass loss rates from Vink et al. (2011). In the visible range, the standard C&B models use the stellar spectral libraries MILES [Sánchez-Blázquez et al. (2006)], for 3540.5 – 7350.2 Å, and IndoUS [Valdes

et al. (2004)], for 7350.2 – 9399.8 Å. The C&B models are calculated for three IMFs: Salpeter (1955), Kroupa (2001), and Chabrier (2003), and for upper mass limits of 100, 300, and 600 $M_\odot$. For each combination of metallicity, IMF, and upper mass limit, a set of 220 spectra is computed, spanning the ages between 0 and 14 Gyr with a nonuniform time step.

In this work, we use the Chabrier (2003) IMF with stellar masses between 0.1 and 100 $M_\odot$. The Chabrier IMF is widely used in current day spectral analysis of many surveys [e. g., Krogager et al. (2013), Shan et al. (2015), Li et al. (2017), Mukherjee et al. (2022)], and unlike Salpeter IMF, the Chabrier IMF does not assume a linear extrapolation at low stellar masses. We adopt the mean Galactic extinction curve [$R_V = 3.1$, Cardelli et al. (1989)]. From the metallicity values in the C&B models, we select four:

- ➤ Subsolar: $Z = 0.004$
- ➤ Solar: $Z = 0.017$
- ➤ Supersolar: $Z = 0.03, 0.04$.

We also test and exploit a new feature of SINOPSIS that was developed specifically for this project. The code now calculates automatically the oldest SSP to be used in each fit. This is chosen to be the oldest possible SSP, from the full model grid, that is still compatible with the age of the universe at the galaxy redshift. Distances to galaxies are always taken to be the same as the one to the cluster they reside in, to avoid biases due to peculiar motions. Finally, in Figure 3.2, we show a flow diagram to explain the working process of the code.

3.6 DIFFERENCES AND IMPROVEMENTS OF THE NEW ANALYSIS

Although stellar population properties for both the WINGS and OmegaWINGS surveys had already been computed [see Fritz et al. (2011), Moretti et al. (2014), for WINGS and OmegaWINGS, respectively], we undertook the task of recalculating all the stellar-related physical properties. This is now done with more accuracy and with a more modern set of models. The main differences in the setup from previous runs are:

- ★ We use four possible values of Z and the C&B (in prep.) SSP models, which provide spectra for 220 ages. Fritz et al. (2011), Moretti et al. (2014) build their own SSP models, using the stellar library from Jacoby et al. (1984), with five possible metallicities ($Z = 0.0004, 0.004, 0.008, 0.02, 0.05$), and the MILES library, with three different metallicities ($Z = 0.004, 0.02, 0.05$). The resulting SSP models have spectra for 108 ages.

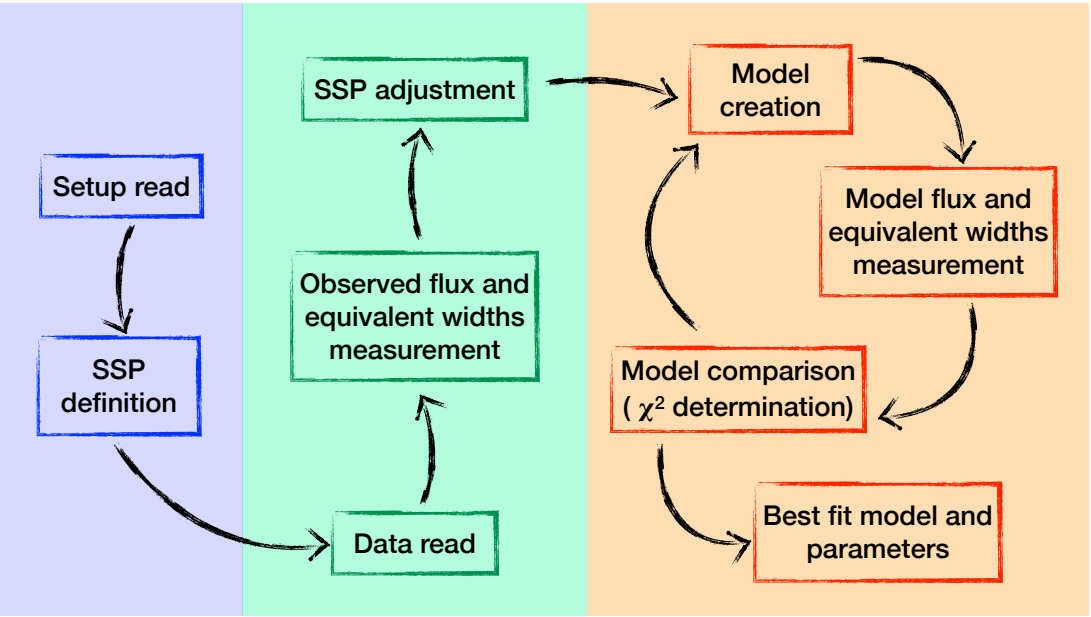

Figure 3.2: Workflow diagram of the SINOPSIS code, divided into three stages. *Left:* input reading; *middle:* flux and EW measurements; *right:* spectrum fitting and outputs.

- ★ We employ the Chabrier IMF, while they use Salpeter's.
- ★ We fix SFR_1 between 0 and 20 Myr (the first age bin), while they allow the possibility of different SFR values within this age range.
- ★ The oldest possible age is the age of the universe at the cluster redshift (see Table 3.1), while they allow it to go up to 17.78 Gyr.
- ★ We utilize Hα EWs and V-band magnitudes to fit OmegaWINGS spectra (see subsection 2.1.2), unlike them.
- ★ We do not apply color corrections to obtain total stellar masses. Conversely, we assume that, for each galaxy, the aperture color is equal to the total color.

In total, we fit 11,369 spectra from WINGS/OmegaWINGS in this work, including cluster members and non-member galaxies. On average, a fit, made by SINOPSIS may take up to approximately $1-2$ minutes in a personal computer.

Part III

RESULTS

4

PHYSICAL PROPERTIES OF THE SAMPLE

In this chapter, we define the galaxy sample in clusters and in the field to be used throughout this work, and we present and analyze some basic properties of the galaxies, such as color, magnitude, stellar mass, phase space position, and if and how they are mutually related.

4.1 GALAXY SAMPLE

Once in possession of all the measured or calculated observables and physical quantities, we proceed to define the sample of objects to be used in our analysis. Galaxies in the final sample should satisfy the following requirements:

1. Stellar mass $\mathcal{M}_* > 3 \times 10^9$ $M_\odot$, roughly corresponding to an absolute V magnitude brighter than $M_V = -18.5$ mag.

2. An acceptable spectral fit from SINOPSIS, represented by a value of $\chi^2 \leqslant 5$.

The limit imposed on the stellar mass is related to the absolute magnitudes of the galaxies, given the photometric threshold reached by the observations, whereby spectroscopy has been obtained down to $V = 20.0$ with a satisfactory enough completeness [$C(r) = 0.8$].

The χ^2 limit was empirically chosen, by comparing the model spectra to the observed ones. Good results are obtained for values equal to or lower than the limit, even in cases for which some of the observational constraints were severely affected by locally bad SNR. We also exclude cD galaxies in clusters and neglect the AGN contribution, since the fraction of AGN in WINGS/OmegaWINGS clusters is approximately 3% [Marziani et al. (2017)]. Furthermore, by taking the imposed limit in EW (Hα) (see the end of Section 3.1), low-luminosity AGN are excluded, while type-1 AGN still present cannot be fitted through stellar populations synthesis, and hence the resulting χ^2 value will be above the threshold we have defined as acceptable. From these considerations, we can safely assume that possible contamination by AGN in the sample of SF galaxies can be neglected.

Regarding the control sample, we have adopted the same approach as in Paccagnella et al. (2016). The sample is assembled with galaxies located in the fields of view of the WINGS/OmegaWINGS clusters with $0.02 < z < 0.09$, and whose relevant

Table 4.1: Number, weighted (w) number, and weighted fraction of galaxies by morphological type in the galaxy sample. The uncertainties in the fractions correspond to binomial errors. Spirals are more common in the field, while early types are more abundant in clusters.

Environment	Type	N	N_w	Fraction
Cluster	E	1208	2605	$26.1 \pm 0.6\%$
	S0	1960	3915	$42.5 \pm 0.7\%$
	SpE	1152	1922	$25.1 \pm 0.6\%$
	SpL	291	452	$6.3 \pm 0.4\%$
Field	E	113	193	$16.7 \pm 1.4\%$
	S0	180	287	$26.6 \pm 1.7\%$
	SpE	253	380	$37.4 \pm 1.9\%$
	SpL	130	211	$19.2 \pm 1.5\%$

physical properties were measured/calculated, but that do not satisfy the membership condition in velocity, i. e., they are foreground or background galaxies.

The final sample of cluster galaxies comprises all 33 OmegaWINGS clusters with spectroscopy and all 22 southern WINGS clusters, but only 4/22 northern WINGS clusters, because of the reasons already mentioned. The final sample from WINGS and OmegaWINGS, taking into account the criteria defined above, contains 4,611 galaxies (8,895 after weighting) in 43 clusters. For the field galaxy sample, we have 677 galaxies (1,071 after weighting). Regarding the morphological classes, the number of galaxies and fractions are listed in Table 4.1 for the cluster and field samples. The clusters for which we have SINOPSIS results are marked in Table A.1.

4.2 THE MORPHOLOGY–DENSITY RELATION

There is a well-known relation between the LD of a galaxy and its morphology: the so-called morphology–density relation [Dressler (1980), Postman & Geller (1984), Pfeffer et al. (2023)][1]. Bright cluster members of WINGS/OmegaWINGS ($M_V \leqslant -18.0$ mag) follow this relation quite well, as shown for the four main morphological classes in the left-hand panel of Figure 4.1; each bin in LD has 1,057 galaxies. It is interesting that, in the lowest LD bin, the fractions of S0s and early spirals are the same (34%), while the fractions of ellipticals and late spirals are equal, as well (16%). A very

1 The dependency of morphology with both clustercentric distance and LD has been discussed since some decades ago [e.g., Whitmore & Gilmore (1991)] and, recently, by Vulcani et al. (2023b).

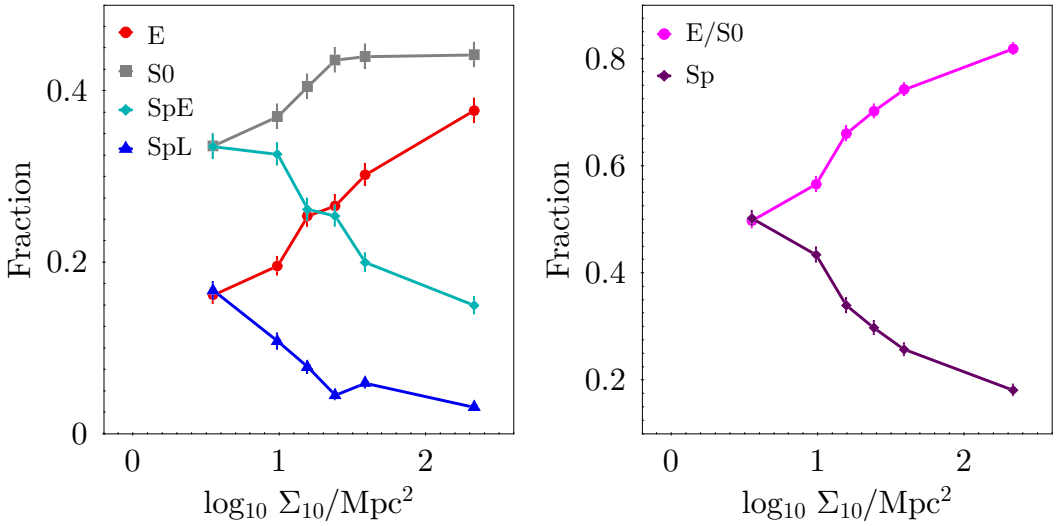

Figure 4.1: Morphology–density relation for WINGS/OmegaWINGS cluster members with $M_V \leqslant -18.0$ for the four main morphological classes: ellipticals, S0s, early- and late-spirals (*left*), and for early- and late-type galaxies (*right*).

similar, possibly clearer, trend is observed when we use a broader morphological classification, grouping ellipticals, and S0s in the early-type class, and all spirals in the late-type class. Each group contributes 50% at the lowest LD while, at the highest density, early-type galaxies represent 80% and late-type galaxies only 20%, as seen in the right panel of Figure 4.1. These results are in good agreement with those of Fasano et al. (2015), Vulcani et al. (2023b), with similar fractions as a function of LD. LD will be analyzed later on (see Section 5.4) as a factor possibly influencing the SFH.

4.3 STELLAR MASS FUNCTION DISTRIBUTION

The stellar mass is a driving factor for several galactic properties, such as morphology, color, SFR, and downsizing [e.g., Binney & Tremaine (1987), Cowie et al. (1996), Kauffmann et al. (2003a), Schneider (2006)]. Thus, when comparing distinct properties, the stellar mass must be taken into account.

The stellar mass function of WINGS galaxies was presented by Vulcani et al. (2011). However, we cannot compare their results with ours in a straightforward manner, since we have used different parameters and theoretical SSP models in SINOPSIS, plus we include here also OmegaWINGS galaxies.

In Figure 4.2, we present the weighted cumulative distribution of the stellar mass for all the galaxy sample, separated by morphological classes, and distinguishing between the cluster and field samples. Firstly, we observe that, as expected, late-type

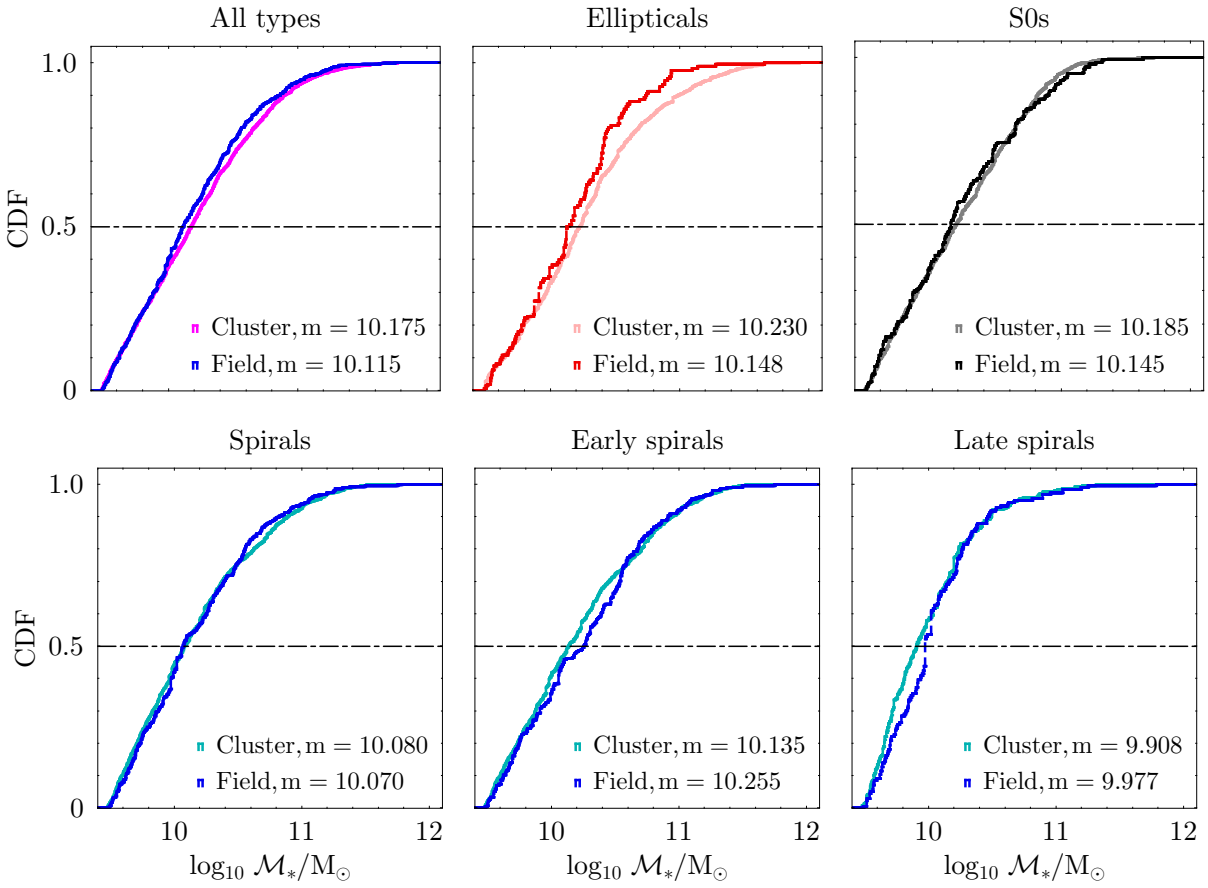

Figure 4.2: Cumulative distribution functions (CDF) of total stellar mass for galaxies in the cluster and field samples, normalized by the respective total number of galaxies, and separated by morphologies, as indicated in the panels. Horizontal black lines mark CDF = 0.5, i.e., the median value of the CDF. The results have been corrected for incompleteness.

galaxies are, on average, less massive than early types, and that clusters contain both more massive and less massive ellipticals than those in the field.

We apply a Kolmogorov-Smirnov (K-S) test to the stellar mass distributions of cluster member and field galaxies, corrected for incompleteness. The results are listed in Table 4.2. The null hypothesis, that cluster and field mass functions come from the same parent distribution, is rejected if the critical value $P < 0.05$. At face value, we find that when we make no morphological distinctions, the mass distributions of field and cluster galaxies are different. The same is true, when we separate according to morphology, for ellipticals and late spirals. Conversely, the distributions of S0s and early spirals are the same for the two environments.

For this study, the number of galaxies in the field is smaller than for those in the cluster sample (see Table 4.1), and these differences are even higher for weighted

Table 4.2: D and P values of the K-S test for the stellar mass cumulative distributions of the cluster and field galaxy samples, according to morphological type.

K-S	All	E	S0	Sp	SpE	SpL
D	0.054	0.130	0.058	0.047	0.086	0.138
P	0.007	0.004	0.329	0.239	0.017	0.007

Table 4.3: D and P mean values of the K-S test for the stellar mass distributions of cluster subsamples and the field sample. These means correspond to 1000 realizations of cluster subsamples with the same number of galaxies as the field sample, for each morphological type. N indicates the number of times, out of 1000, that $P < 0.05$.

K-S	All	E	S0	Sp	SpE	SpL
D	0.063	0.151	0.067	0.062	0.081	0.147
P	0.060	0.054	0.562	0.232	0.217	0.030
N	662	676	14	73	165	825

numbers (see Equation 2.2). We checked whether the results described above for the K-S test could be affected by the different numbers of galaxies in the field and clusters using a statistical test. We made 1000 realizations of cluster subsamples with the same number of galaxies as in the field sample (the probability of a galaxy to be chosen is given by its weight), and compared the cluster subsamples with the field, applying again the K-S test. We also counted the number of realizations for which both distributions were different. Results are presented in Table 4.3.

We find that the differences in the sizes of the cluster and the field samples do affect the results. The probability of having different parent distributions in the cluster and field is 0.662 for all types together, 0.676 for ellipticals, and 0.825 for late spirals, while for S0s, all spirals together, and early spirals, this probability is very low. As a control test, we also compare the cluster subsamples with the whole cluster sample and find that, for all the morphologies analyzed, they come from the same parent distribution with a probability larger than 0.98.

Calvi et al. (2013) studied the mass function of WINGS galaxies, compared to the "general field", through the Padova-Millennium Galaxy and Group Catalogue (PM2GC). We also find that the mass function changes with morphology at fixed environment. However, as demonstrated by the K-S tests that take into account the different numbers in the cluster and field samples, the parent distributions of ellipticals and late spirals are likely very different in clusters and the field.

Furthermore, the mass limits adopted in the two works are different, as well as the samples themselves (we use WINGS+OmegaWINGS for cluster and field galaxies, while they only include WINGS and PM2GC). A result that is, however, common to the two investigations is that the most massive ellipticals are indeed found in clusters.

4.4 COLOR AND MAGNITUDE RELATIONS

Colors of galaxies, in the first instance, are a broad proxy for stellar population properties. Redder galaxies possess more evolved stellar populations with lower star formation activity, while bluer galaxies boast younger stellar populations with recent star formation [e.g., Baldry et al. (2004)]. Exploring the so-called color-magnitude and color-mass diagrams [e.g., Flower (1996), Baraffe et al. (1998)], leads us to the study of stellar properties, such as stellar ages and SFRs.

We use the absolute magnitudes (Section 3.1), rest-frame colors, and total stellar masses (Section 3.3), as provided by SINOPSIS, based on the spectral model and automatically including K-corrections. We have assumed that the K-corrections are the same for aperture (A) and total (Tot) magnitudes:

$$M^{A} = m^{A} - DM - K^{A}_{Corr} \tag{4.1}$$

$$M^{Tot} = m^{Tot} - DM - K^{Tot}_{Corr}, \tag{4.2}$$

where M is absolute magnitude, m denotes apparent magnitudes, and DM is the distance modulus. Subtracting Equation 4.1 from Equation 4.2, we find for absolute magnitudes in the B and V bands:

$$M^{Tot} = m^{Tot} - m^{A} + M^{A}. \tag{4.3}$$

The advantage of this approach is that we do not need to rely on pre-calculated K-correction values that depend on morphological types, which might be problematic for cluster spirals, since they are normally redder than their field counterparts. Furthermore, this formulation has already been successfully tested and used in Valentinuzzi et al. (2010).

4.4.1 *Mass–luminosity relation*

Some of the most important properties obtained with SINOPSIS include the stellar mass and absolute magnitudes in several bands (Section 3.1). We take advantage of these quantities to construct the well-known mass–luminosity relation for the galaxy sample, as shown in Figure 4.3, divided into morphologies. For all types, the relation is fulfilled, albeit with steeper slopes for earlier types. The fit equation for the whole galaxy sample is:

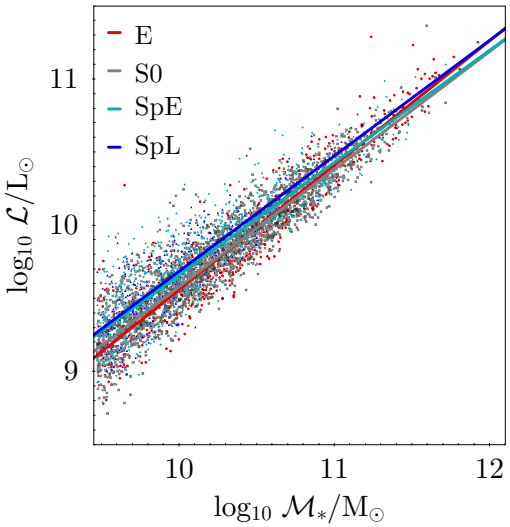

Figure 4.3: Luminosity-stellar mass relations for the cluster galaxy sample, separated into morphological types. The best least square fits are shown with solid lines, with a different color for each type, as labeled.

$$\log \frac{\mathcal{L}}{L_\odot} = 1.381 + 0.821 \cdot \log \frac{\mathcal{M}_*}{M_\odot}. \tag{4.4}$$

A very similar slope (0.89) was found by Bernardi et al. (2010), using *r*-band data from the SDSS.

4.4.2 *Color–magnitude and color–mass diagrams*

Several studies [e. g., Whitaker et al. (2013), Mendel et al. (2015)] have demonstrated that galaxy colors in different bands are useful for determining stellar-population parameters, such as mean stellar ages. Colors can be obtained much more easily than galaxy spectra, and they can be used as a good proxy for the mean ages of stellar populations, provided that it can be assumed that dust extinction is a second-order effect, or that it affects equally galaxies of similar type. The broad morphological classification into early and late types allows us to separate the galaxy sample in two clouds, i.e., the well-known bimodal distribution of galaxy colors, with galaxies in the so-called red sequence generally being more massive, luminous, and quiescent, while the "blue clump" hosts late-type galaxies, less luminous but with younger stellar populations, on average [Eales et al. (2018)].

In Figure 4.4, we present color-mass and color-magnitude diagrams for galaxies in the cluster and field sample. Comparing cluster and field galaxies is not straightforward, due to the smaller number of galaxies in the second sample. For

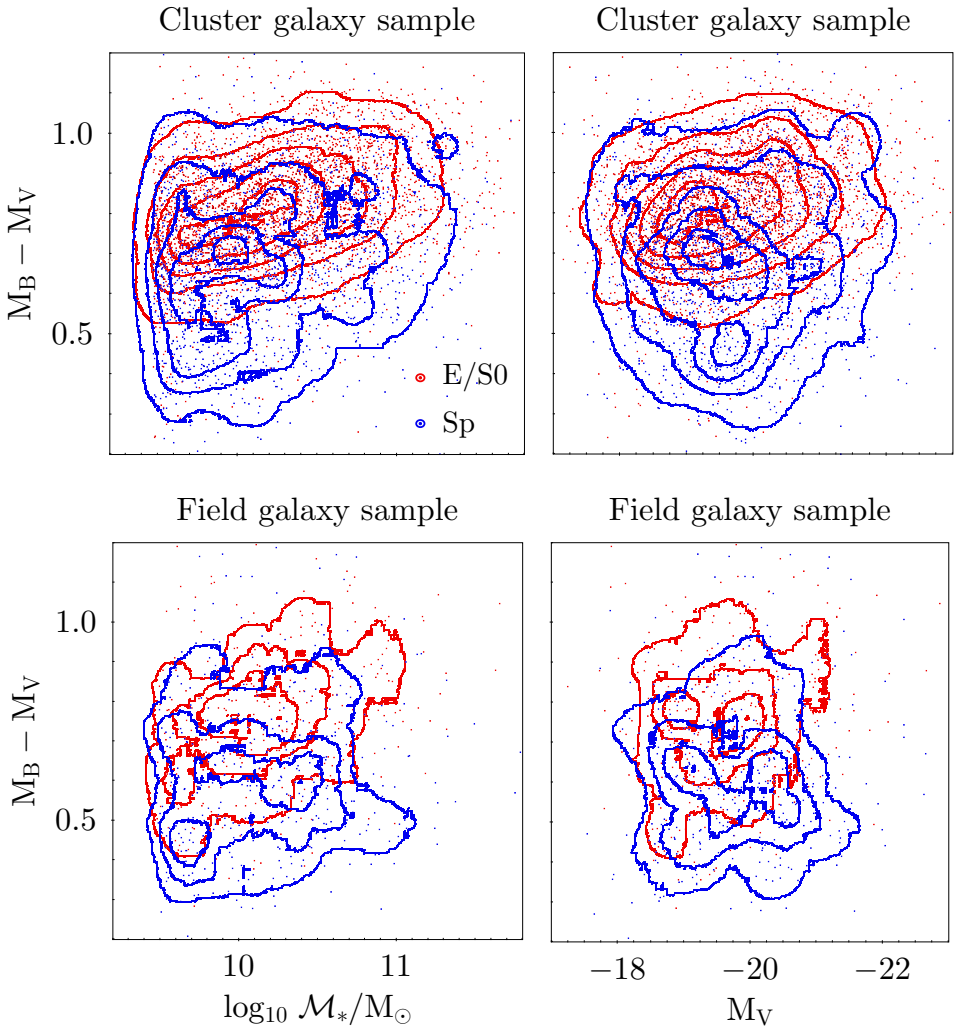

Figure 4.4: Color-mass (*left column*) and color-magnitude (*right column*) diagrams for cluster (*top*) and field (*bottom*) galaxy samples. *Red points and number density isocontours:* elliptical and S0 galaxies; *blue points and number density isocontours:* late-type galaxies.

this reason, we take averages in bins of stellar mass and luminosity, also separated by morphological class, as shown in Figure 4.5.

When separating galaxies into early and late types, we obtain a clear correlation for color as a function of stellar mass, with bluer colors for field galaxies. Early types present a steeper slope with mass than late types in both environments (top left panel). If this relation is analyzed as a function of morphology (bottom left panel), we observe that late spirals have practically the same colors in clusters and the field, at all masses. Similarly, ellipticals in both environments show negligible differences, at fixed mass. On the other hand, early cluster spirals are redder than those in the field by $0.04 - 0.06$

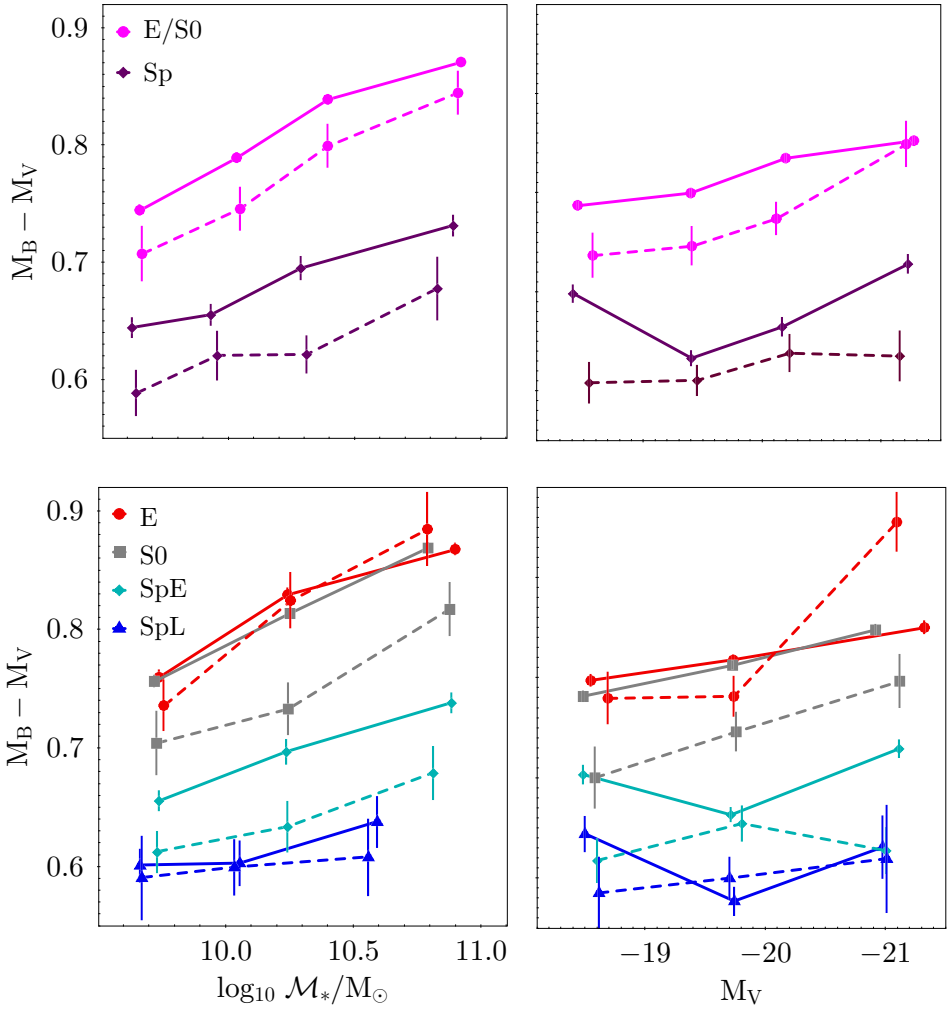

Figure 4.5: Mean colors of galaxies in the cluster (*solid lines*) and field (*dashed lines*) samples, as a function of stellar mass (*left column*) and luminosity (*right column*), divided into morphological classes, as labeled. Error bars were obtained through the bootstrap resampling method.

mag. The strongest difference is found for S0 galaxies: in clusters, they are as red as ellipticals, but in the field, they are $0.05 - 0.08$ mag bluer. Note that these differences are significantly larger than the uncertainties, gathered with the bootstrap resampling method (see Appendix C).

The trend between color and luminosity (see right plots in Figure 4.5) is less evident; more luminous early-type galaxies are redder, but late types do not present a clear result. When we differentiate between the four morphologies, the most luminous E and S0 galaxies are redder in both clusters and the field, while the colors of early and late spirals do not seem to be a function of luminosity.

Besides displaying a clear, well-known, dependency of color on mass [e.g., McGaugh & Schombert (2014), van der Wel et al. (2016)], cluster galaxies are redder, at fixed mass, than their field counterparts [e.g., Martinez et al. (2010), and likewise see the left panel in Figure 4.5]. This result is also confirmed by Lewis et al. (2002).

4.4.3 *Color–local density and projected distance*

We explore now the possibility of a correlation between color, LD, and clustercentric radius. Using SDSS data for 19,714 galaxies with $0.030 < z < 0.065$, and absolute r-band AB magnitudes between -19.4 and -21.4, Tanaka et al. (2004) found a correlation between $(g-i)$ color and LD, measured by Σ_5 (see Equation 2.5), according to which redder and more luminous galaxies are expected in higher LD environments. We follow this approach and divide our cluster galaxy sample into two groups of luminosity, respectively, fainter and brighter than $M_V = -19.2$, and also in two groups of stellar mass, respectively, more massive and lighter than $\log_{10} \mathcal{M}_*/M_\odot = 10.2$, as shown in Figure 4.6. Despite the different colors and LD gauge used (see subsection 2.2.3), we get a good agreement between our results and those of Tanaka et al. (2004). We find that color is correlated with LD, with redder galaxies in higher-density environments. On the other hand, more luminous galaxies are redder than fainter ones, and more massive galaxies are redder than lighter ones; the color difference between more and less massive galaxies seems to be larger than when dividing by luminosity.

Baldry et al. (2004) found a small increase in color for early types very close to the cluster center, with the highest LDs. We test that result, taking color averages as a function of LD, and dividing by morphology, as shown in Figure 4.7 (left panel). Since this time we have fewer LD bins, the trend in color is smoothed in comparison with Figure 4.6, but we can even see a trend in the color of late-type galaxies with LD, supported by the bootstrapping analysis. On the other hand, the color of Es and S0s is mainly independent of LD.

In Figure 2.3, we show the distribution of LD as a function of distance to the cluster center. Although the relation between these two quantities is not univocal and both can be biased by projection effects, the clustercentric distance approximates the environment on a more global scale. We use both to characterize the environment within clusters. Here, we also analyze color as a function of projected distance, dividing the sample by morphology, as shown in the right panel of Figure 4.7. We obtain that colors are mostly invariant, within the errors, for all morphologies.

Finally, when comparing the colors of cluster and field galaxies separated by morphology, larger differences are found for S0s and early spirals (see again Figure 4.7). The colors of ellipticals and late spirals are more similar in the two environments, as already pointed out in Figure 4.5.

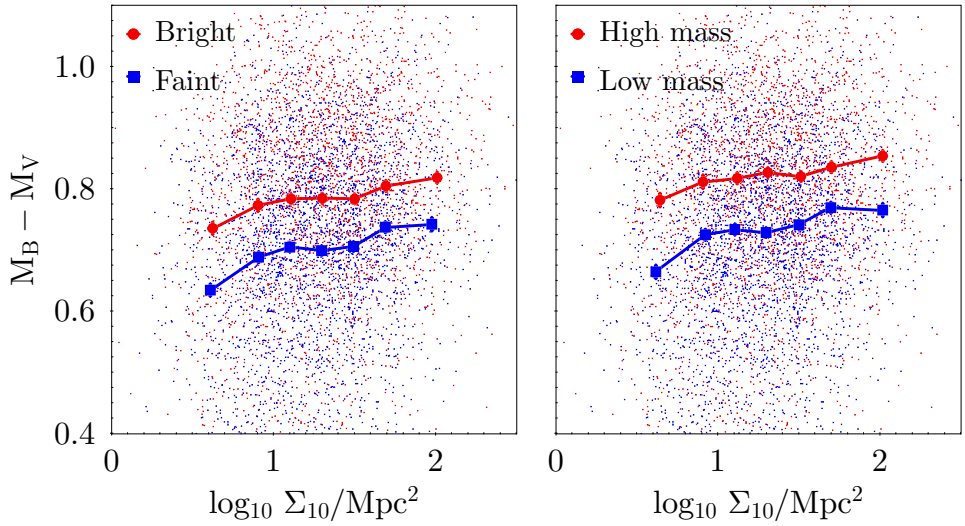

Figure 4.6: Color *versus* LD for the cluster galaxy sample, divided by luminosity (*left*: bright and faint), and by stellar mass (*right*: high and low mass). Bright and massive galaxies are redder than faint and low-mass ones, respectively. Galaxies are also redder at higher LDs.

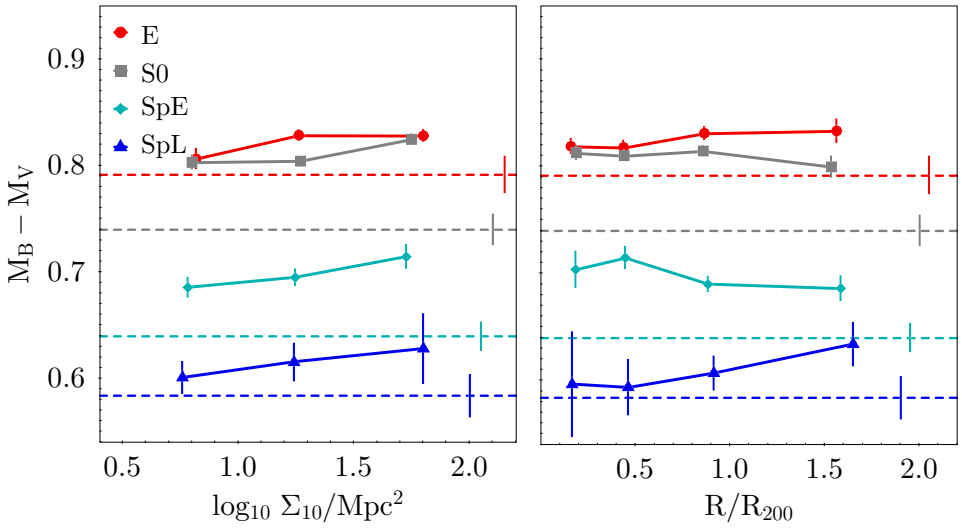

Figure 4.7: Mean color *versus* LD (*left*) and clustercentric distance (*right*) in the cluster (*solid lines*) and field (*dashed lines*) samples, separated by morphology. Error bars were obtained through the bootstrap resampling method. Colors are approximately invariant, within errors, for all morphologies, while cluster galaxies are redder than field ones.

4.5 INCLINATION DISTRIBUTION

As we mentioned above, in this work we use aperture spectra, which only cover the central part of the galaxies (aperture diameter $\sim 2-3$ kpc), as many other authors

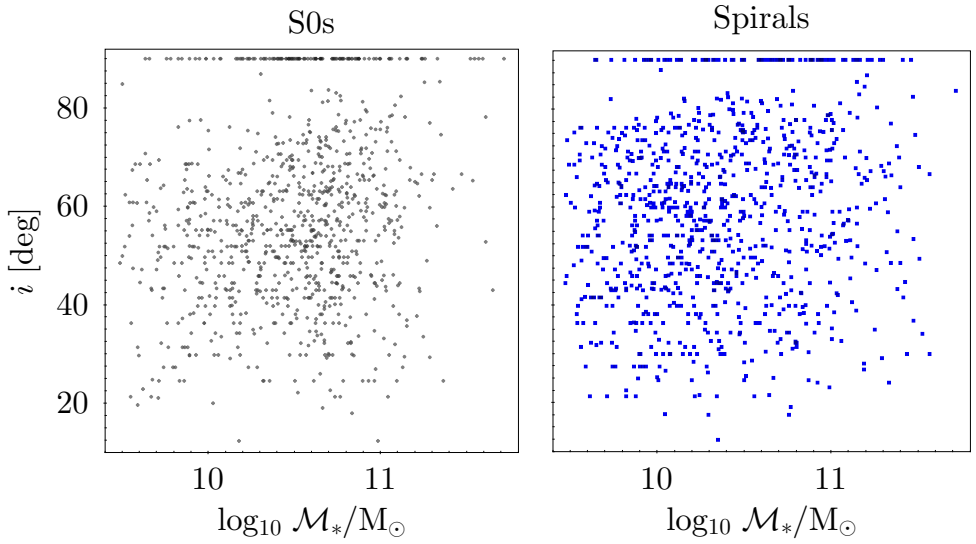

Figure 4.8: Galaxy inclination *versus* stellar mass for disk galaxies in the sample: S0s (*left*) and spirals (*right*). There is no trend between the inclination angle and the galaxy stellar mass. Several galaxies are reported as seen edge-on ($i = 90°$). Typical errors in the inclination angle are a few degrees.

have done [e.g., Kauffmann et al. (2003a), Kauffmann et al. (2003b), Kauffmann et al. (2004), Gallazzi et al. (2005), Casado et al. (2015), for the SDSS; Guglielmo et al. (2015), Paccagnella et al. (2016), for WINGS and OmegaWINGS]. To investigate whether the derived SFHs suffer from biases due to the better coverage of stellar populations in the centers of galaxies, in Figure 4.8, we plot the distribution of stellar mass as a function of galaxy inclination along the line-of-sight, for 672 S0s and 309 spirals in our sample. The crowding of points with $i = 90°$ can be explained by the fact that it is difficult to precisely measure the inclination of galaxies seen almost edge-on. The inclination values have been taken from the HyperLEDA[2] catalog [Makarov et al. (2014)]. A K-S test reveals that there is no correlation between the derived stellar masses and the inclination values, neither for S0s nor for spirals, with $P = 0$.

An observed trend of stellar mass with inclination would mean (at least for spirals, for which a different line-of-sight view can result in the most significant difference, because of their structure) that the stellar populations sampled by the fiber do not represent the average stellar populations of the galaxies. For instance, for a perfectly edge-on spiral, we would observe mainly the (dusty) disk and not the bulge, and this could result in a severe underestimate of the stellar mass. The flat distribution of mass with inclination is a good indication that fiber spectra are sampling stellar populations in a whole range of galactocentric distances for most galaxies. The results we get for the SFHs further confirm this analysis.

2 http://leda.univ-lyon1.fr/

4.6 PHASE–SPACE DIAGRAMS

The position-velocity space of infalling galaxies into a cluster provides kinematic information about their positions and infall times, and the assembly history within the cluster [Oman et al. (2013)]. While recently accreted objects will have higher velocities, in general, galaxies that have been in the cluster for a few cluster crossings (i.e., the virialized galaxies) will gather at low velocities and closer to the cluster center, partially via dynamical friction, especially for high-mass galaxies [Mahajané et al. (2011), Jaffé et al. (2015)]. Phase–space diagrams are very useful to analyze the processes and evolutive stages that galaxies suffer in clusters, such as gas stripping, star formation quenching, and the final settling into the cluster [Jaffé et al. (2015)]. Through simulations, [e. g., Taranué et al. (2014)] suggest that a galaxy can be (almost) completely quenched in a single orbit through the cluster.

Here, we study the phase–space diagram of galaxies: the line-of-sight velocity, with respect to the mean cluster velocity, as a function of clustercentric radius, in units of cluster virial radius (R_{200}; see Equation 2.1). We calculate weighted means of three parameters: projected distance to the cluster center, LD, and peculiar velocity with respect to the cluster center. The results for the four main morphological types are listed in Table 4.4 and shown in Figure 4.9. We obtain monotonic trends for the three properties with morphology. Earlier types are located closer to the cluster center, with higher LDs, while late types lie at larger radii from the cluster center, reside in lower LDs, and have larger peculiar velocity differences.

4.7 ACTIVELY STAR-FORMING GALAXIES

We consider as actively SF all those galaxies for which SINOPSIS can measure emission lines and derive a minimum value of $SFR_1 > 1 \times 10^{-3}$ $M_\odot$ yr^{-1}. The threshold value is

Table 4.4: Values of mean clustercentric distance, LD, and peculiar velocity in units of cluster velocity dispersion, for the galaxy sample, divided by morphology. Uncertainties were obtained with the bootstrapping method. These values are plotted in Figure 4.9.

Type	R/R_{200}	$\log_{10}\ \Sigma_{10}/Mpc^2$	$\Delta v/\sigma_{cl}$
E	0.561 ± 0.011	1.436 ± 0.011	0.904 ± 0.022
S0	0.619 ± 0.010	1.389 ± 0.009	0.930 ± 0.018
SpE	0.802 ± 0.013	1.230 ± 0.012	1.043 ± 0.027
SpL	0.907 ± 0.039	1.160 ± 0.026	1.161 ± 0.057

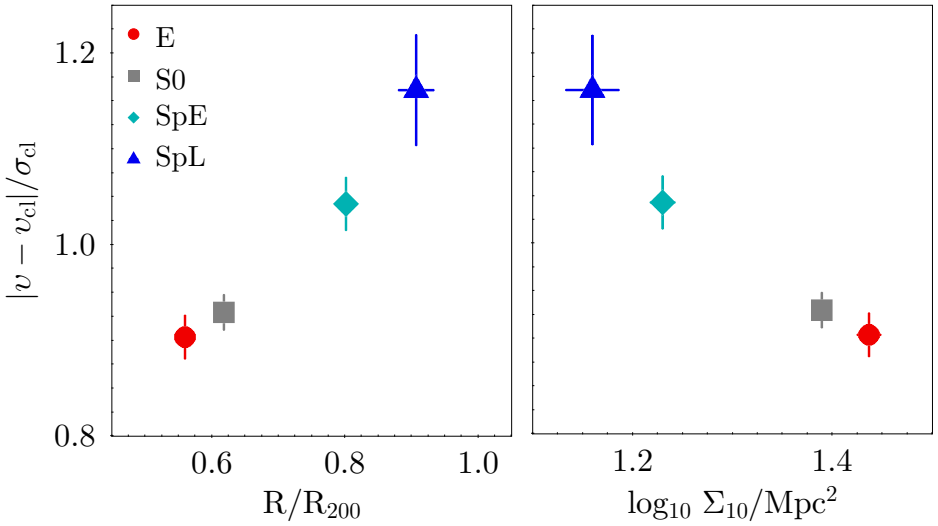

Figure 4.9: Mean phase–space diagram (*left*) and mean peculiar velocity as a function of mean LD (*right*) for galaxies in the sample divided into morphologies. Radial velocities in units of cluster velocity dispersion. Error bars were calculated through the bootstrap resampling method. A clear trend between galaxy environment and morphology is observed. Early types are located towards the cluster centers and at higher LDs, while late types have larger clustercentric distances, lower LDs, and higher radial velocities than the cluster centers.

calculated by taking into account a typical age range of about 10^7 yr for SFR_1, and a minimum stellar mass of 10^4 $M_\odot$:

$$SFR_1 > \frac{10^4\ M_\odot}{10^7\ \mathrm{yr}} = 10^{-3}\ M_\odot\ \mathrm{yr}^{-1}. \tag{4.5}$$

If the stellar population synthesis method is applied to spectra sampling total stellar masses lower than 10^4 $M_\odot$, it may lead to biased results, due to the possibly incomplete sampling of the IMF [Weidner & Kroupa (2006)]. We remind the reader that (as mentioned in Section 3.4) galaxies with low values of Hα ($0 < EW_{H\alpha} < 6$ Å) host AGN, and their Hα emission is not due to star formation (see Section 3.4). For this reason, we consider them as non-SF (i. e., $SFR_1 < 10^{-3}$ $M_\odot$ yr^{-1} or, in practice, $SFR_1 = 0$ $M_\odot$ yr^{-1}).

We now investigate the influence of the large-scale cluster environment on the quenching of star formation, by calculating the fraction of SF galaxies as a function of both galaxy morphology and environment. Table 4.5 shows the fraction of SF active galaxies in clusters and the field, divided by morphology. There is a clear trend of increasing SF fraction, from early to later types, in both environments, and, for all types, SF fractions in the field are larger than in clusters. Strikingly, more than half of

Table 4.5: Actively SF (weighted) fractions of cluster and field galaxy samples, classified by morphology. Uncertainties represent binomial errors.

Type	Cluster	Field
All	$34.1 \pm 0.5\%$	$69.8 \pm 1.4\%$
E	$23.0 \pm 0.8\%$	$54.1 \pm 3.7\%$
S0	$26.5 \pm 0.7\%$	$58.6 \pm 2.9\%$
SpE	$53.9 \pm 1.1\%$	$75.5 \pm 2.2\%$
SpL	$79.4 \pm 1.9\%$	$88.1 \pm 2.2\%$

ellipticals and S0s in the field are SF, versus 25% or less in clusters. A population of blue SF early-type galaxies is also found in large galaxy samples of clusters and field in the local universe [e. g., Schawinski et al. (2009), Brambila et al. (2023)], becoming more common for low stellar masses, reaching a fraction of $\sim 20-30\%$ for early types with 5×10^9 $M_\odot$ [Kannappan et al. (2009)]. On the other hand, 80% or more of the SpLs are active in clusters and in the field, the SF fraction of SpEs drops from 75% in the field to slightly more than 50% in clusters.

Going into finer detail, we explore the phase–space diagrams by morphology and separated into SF and quenched galaxies. For all types, we expect that most galaxies located in the cluster outskirts (i.e., at large distances to the cluster center) are SF, while most quenched galaxies have low peculiar velocities and are found closer to the cluster center. This result is confirmed when we calculate, as before, weighted means of clustercentric distance, LD, and peculiar velocity, as shown in Table 4.6 and plotted in Figure 4.10.

Trends are clearer when phase space is divided into different regions of infalling galaxies, as done by Rhee et al. (2017) and we show in Figure 4.11. Region A is dominated by the most recently infalling galaxies, and those that have not yet fallen; B and D correspond to galaxies infalling at relatively recent and intermediate times; the C region is a combination of B and D. E contains most of the galaxies with ancient infall times, which are well settled within the cluster potential well. By breaking down phase space into these regions, we can associate the infall of galaxies with different timescales. Thus, in the left panel of Figure 4.10, quenched elliptical and S0 galaxies are located in the bottom left corner, i.e., the early infall time region E of phase space, while SF versions of these same morphologies sit in zones of more recent infall times.

Quenched late-type galaxies infall at intermediate times, and hence with enough time for environmental interactions to stop their SF activity. On the other hand, SF early types are located in a zone that suggests that these objects have only recently entered the cluster from the field. Finally, SF late types populate a zone that implies

Table 4.6: Values of mean-weighted clustercentric distance, LD, and peculiar velocity with respect to the cluster center, for quenched and SF active galaxies, separated by morphology. Uncertainties were obtained using the bootstrapping resampling method.

	Type	R/R_{200}	$\log_{10}\Sigma_{10}/Mpc^2$	$\Delta v/\sigma_{cl}$
Star-forming	E	0.596 ± 0.013	1.375 ± 0.024	1.021 ± 0.054
	S0	0.681 ± 0.026	1.326 ± 0.017	1.018 ± 0.035
	SpE	0.850 ± 0.015	1.196 ± 0.014	1.119 ± 0.039
	SpL	0.935 ± 0.034	1.141 ± 0.029	1.205 ± 0.065
Quenched	E	0.520 ± 0.010	1.453 ± 0.013	0.812 ± 0.023
	S0	0.587 ± 0.014	1.410 ± 0.011	0.874 ± 0.020
	SpE	0.745 ± 0.015	1.271 ± 0.018	0.954 ± 0.033
	SpL	0.801 ± 0.047	1.231 ± 0.056	0.990 ± 0.101

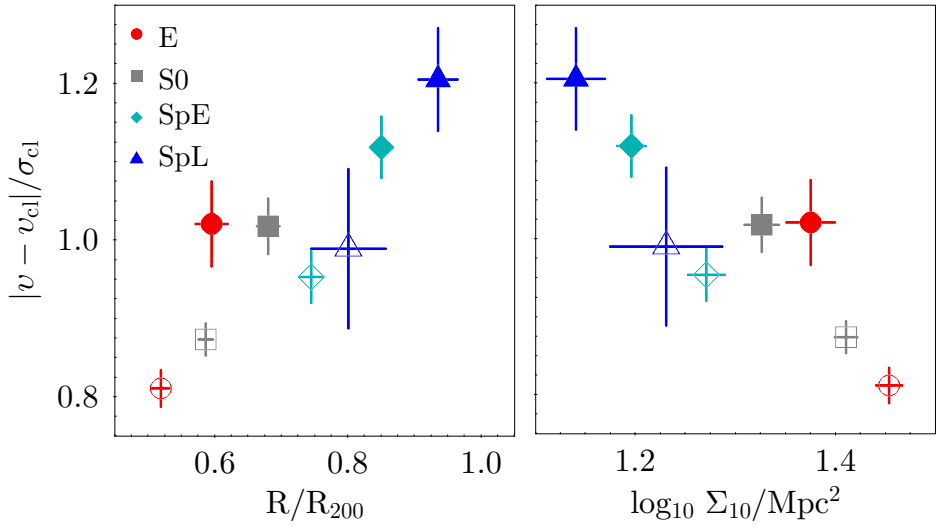

Figure 4.10: Mean phase–space diagram (*left*) and mean peculiar velocity as a function of mean LD (*right*), for the cluster galaxy sample separated into SF (*filled symbols*) and quenched (*empty symbols*) galaxies. Morphologies, units, and error bars as in Figure 4.9. Similarly to Figure 4.9, there is a trend between morphology and position in phase space. Quenched galaxies are more settled in the cluster, while SF galaxies have fallen into the cluster more recently.

either the most recent infall or that the galaxies are just to be accreted into the cluster.

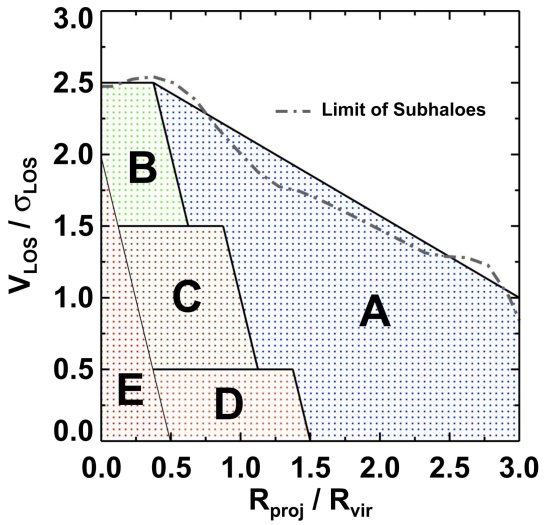

Figure 4.11: Phase–space diagram, separated into five regions to illustrate infalling time/time since the start of infall. A: most recent infall; B: recent infall; D: intermediate infall; C: mixed region between B and D; E: ancient infall. The *gray dashed line* shows the limit of subhalos after 1,000 random rotations. The shape and location of each region are somewhat arbitrary. Image taken from Rhee et al. (2017).

4.7.1 *Star-forming fraction with projected distance and local density*

When we consider the percentage of actively SF galaxies (Figure 4.12), as a function of clustercentric distance (left panel) and LD (right panel), we note a decline towards the cluster center. Between $\sim 2-0.2\ R_{200}$, the SF fractions go from $61.0 \pm 2.6\%$ to $42.7 \pm 3.0\%$ for SpE; from $84.6 \pm 3.5\%$ to $70.3 \pm 7.5\%$ for SpL; from $33.2 \pm 3.4\%$ to $18.1 \pm 1.3\%$ for Es, and from $39.3 \pm 2.5\%$ to $22.4 \pm 1.2\%$ for S0s. The SF fractions of both spiral types exhibit a sudden drop of 9% between $0.5-0.2\ R_{200}$, while for early types they taper slowly within $0.9\ R_{200}$ and display fluctuations that may be due to projection.

For all morphological classes, SF fractions in the field are higher than in clusters, at any distance from the center or LD value. The fractions as a function of LD (Figure 4.12, right panel) are comparable to those obtained concerning projected distances. When we separate by morphological classes, SF early-types decrease slightly with increasing LD. The quenching effect of the environment, parameterized by both clustercentric distance and LD, is somewhat stronger for spirals.

These results are in agreement with Barsanti et al. (2018) and Paccagnella et al. (2016) for whom the fraction found of quenched galaxies in the field is minimum, while this population in clusters is abundant. Besides, Jaffé et al. (2015) found that HI-rich galaxies are located in the cluster outskirts. These blue SF galaxies slowly decline their star formation activity while they lose their gas content through RP,

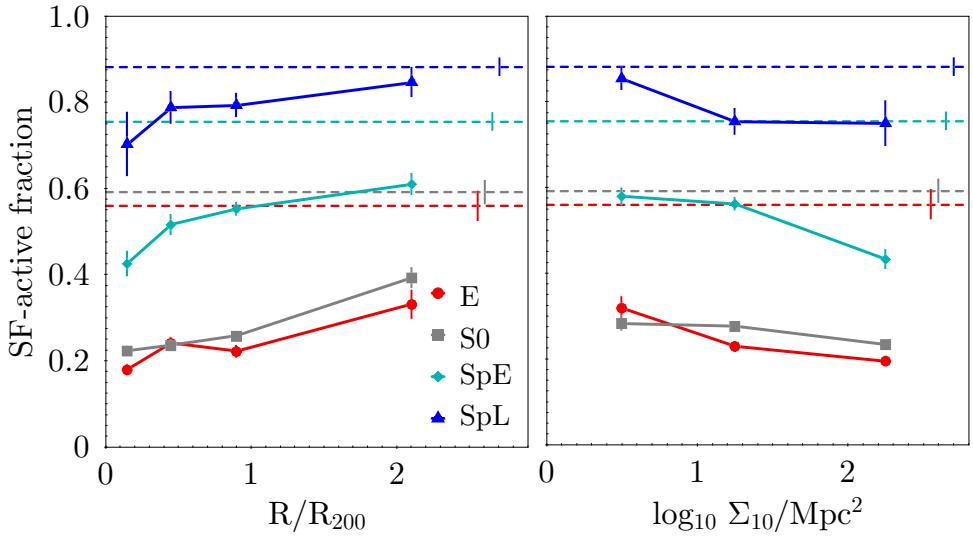

Figure 4.12: Fractions of SF galaxies as a function of clustercentric distance (*left*) and LD (*right*), for the four morphological classes in the sample. The *horizontal dashed lines* show fractions of SF galaxies in the field, for the same morphological types. Error bars indicate binomial errors. SF fractions decrease toward the cluster center and higher LDs.

becoming passive toward the 'virialized' region of the cluster, which is dominated by early-type quenched galaxies.

4.7.2 *Star-forming fraction with cluster mass*

The fraction of galaxies that are currently observed in an actively SF state, should in principle, show a dependence both on their morphology and on the environment. In a simplistic view, we would expect that the higher the cluster mass, the higher its "quenching ability". Here, we analyze a possible role of the cluster mass, taking as its proxies σ_{cl} and L_X. As mentioned in Section 2.3, both properties are good indicators of total mass for virialized clusters (note that, as only some of the WINGS clusters are virialized; Lourenço et al., submitted), the relation between σ_{cl} and L_X is not exactly linear). Superimposed to the assumed environmental effects, morphology is definitely playing a role in determining the SF fraction and, as we noted previously, the trends for the morphological fractions are slightly different as a function of both properties (see Figure 2.4 and Figure 2.5). Another effect playing a role is the presence of mechanisms typical in clusters (but not only in clusters, i. e., galaxy neighbor interactions, see Section 5.5 below), that can enhance star formation.

In Figure 4.13, we show the fractions of SF galaxies, by morphological type, as a function of σ_{cl} and L_X, and compare them to the SF fractions of the same

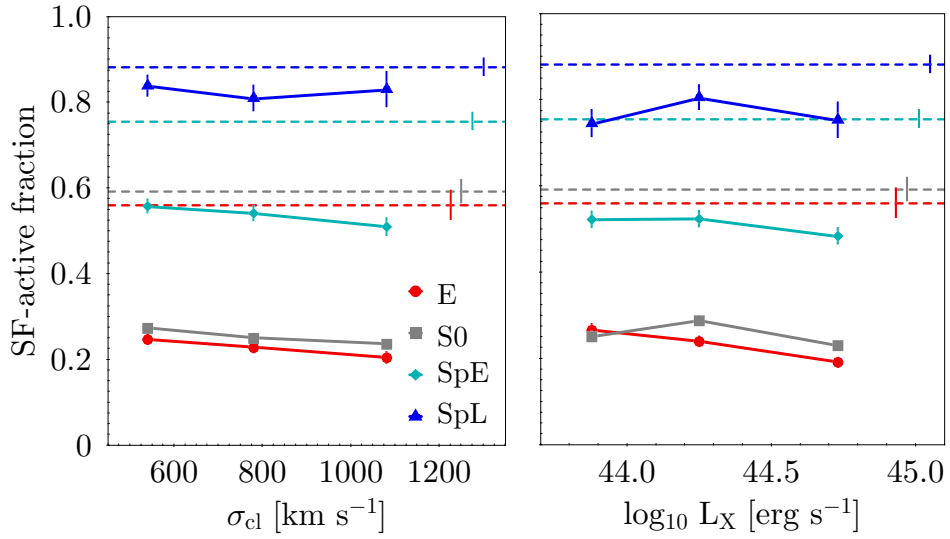

Figure 4.13: Fractions of SF galaxies as a function of cluster galaxy velocity dispersion (*left*) and X-ray luminosity (*right*), by morphological type. *Horizontal dashed lines* and error bars as in Figure 4.12. SF fractions in the field are always higher than those in clusters for all morphologies, while fractions, as a function of cluster mass, are almost flat.

morphological classes in the field (dashed lines). Only mild trends are observed in clusters, with hints of decreasing fractions with σ_{cl} for Es and S0s, and for Es with L_X.

These results are in agreement with both Poggianti et al. (2009) and Fritz et al. (2014), and extend what was previously reported by them, who found that the fraction of emission-line galaxies does not depend on the general properties of the cluster. However, both works only analyzed galaxies located within half a cluster virial radius. Here, we do not simply rely on the presence/absence of emission lines, but we use a threshold in the $EW_{H\alpha}$ to correct for possible contamination from non SF ionization processes.

We conclude that the fraction of SF galaxies is larger in the field than in clusters, for all morphologies. Nevertheless, it is worth noting that the size of the difference is an almost monotonic function of morphological type, with Es and S0s displaying a larger difference than spirals. This result is likely related to the time spent within the cluster, which affects both the morphology and the gas content of galaxies.

4.8 SFR–MASS RELATION

The SFR-mass relation, also known as the MS for galaxies, has been observed in the local universe, for instance with SDSS data [e.g., Kauffmann et al. (2003a), Chang

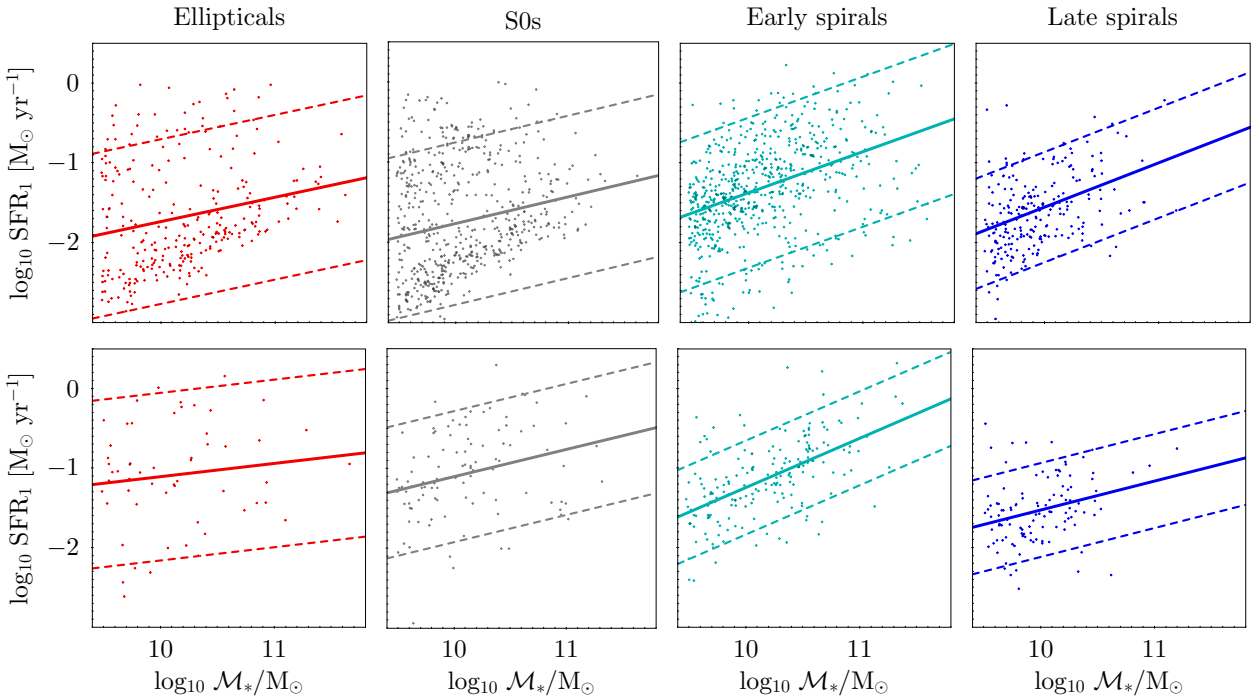

Figure 4.14: SFR–stellar mass relation for SF galaxies in the cluster (*top*) and field (*bottom*) samples, divided by morphology, as labeled. *Solid lines:* least-square best fits. *Dashed blue lines:* ±1.5 σ dispersion.

et al. (2015), Pan et al. (2018)], in high redshift galaxy populations to $z \sim 2$ [e.g., Lara-Lopez et al. (2010), Peng et al. (2010), Wuyts et al. (2011)] and above [e.g., Speagle et al. (2014), Salmon et al. (2015), Katsianis et al. (2016)]. For the sample of WINGS and OmegaWINGS, the SFR-mass relation has been presented and discussed by Paccagnella et al. (2016). Here, besides using the results from the new stellar population analysis (see Section 3.6), we make a distinction based on morphology. Only galaxies with $\mathrm{SFR}_1 > 1 \times 10^{-3}$ M$_\odot$ yr^{-1} have been used (see Section 4.7). Results are presented in Figure 4.14 for cluster and field galaxies, separated by morphology.

We fit the points of each relation with straight lines, whose parameters are summarized in Table 4.7. We separate by environment and note a monotonic increase of the slope, m, with morphology in clusters. Later types present a steeper slope, i.e., earlier types have flatter SFR-mass relations. In the field, on the other hand, the slope for SpL is shallower than for SpE. However, SpLs are the least massive galaxies and constitute the least numerous morphological class, so this result could be biased statistically due to the scarcity of massive SpL in the field. There is also a trend with morphology in the scatter of SFR_1, in both environments: it is always wider for earlier types, and goes from 0.69 dex to 0.46 dex for cluster galaxies; the difference is larger for field galaxies and goes from 0.70 to 0.39 dex (see the σ values in Table 4.7).

Table 4.7: Parameters of the line equations ($y = m * x + b$) corresponding to the best fits in Figure 4.14. σ is the standard deviation of $\log_{10}$ SFR$_1$.

Environment	Parameter	E	S0	SpE	SpL
Cluster	b	−4.783	−5.086	−6.507	−7.110
	m	0.305	0.332	0.514	0.556
	σ	0.688	0.674	0.628	0.461
Field	b	−2.772	−4.503	−7.435	−5.165
	m	0.167	0.340	0.619	0.364
	σ	0.703	0.547	0.464	0.394

On the other hand, at fixed morphology and for similar stellar masses, we obtain a wider range of SFR in cluster galaxies than in their field counterparts (see σ values in Table 4.7), except for ellipticals, which have similar dispersions in both environments. In Chapter 5 and Chapter 8, we offer some possible explanations and further results.

To investigate whether the smaller number of galaxies in the field sample introduces biases in the σ measurements, we performed a statistical test for each morphology. We extracted 1000 random subsamples of cluster galaxies of the same size as the field sample (the higher the weight of a given galaxy, the higher the probability of being chosen), and compared the mean standard deviations of the subsamples with that of the field sample. We confirmed that the MSs of cluster S0, SpE, and SpL have larger dispersions than those of their field counterparts and that ellipticals have the same dispersions in both environments. With this analysis, we demonstrate that the small number of galaxies in the field sample is not affecting these results.

4.9 FINAL REMARKS ON THE SAMPLE PROPERTIES

Here, we summarize the characteristics of the galaxy sample and the main results obtained in this chapter. The galaxy cluster sample comprises only confirmed members with the best spectral fits ($\chi^2 \leqslant 5$) in SINOPSIS, and with a cut in stellar mass, i.e., $\mathcal{M}_* > 3 \times 10^9\ M_\odot$, corresponding to a cut in luminosity $M_V < -18.5$ mag. The field galaxy sample satisfies non-cluster membership in a redshift range $0.02 < z < 0.09$, with the same stellar mass limit and fit quality. The numbers of galaxies in the samples are 4,611 for the clusters (8,895 after weighting) and 677 (1,071 weighted) for the field. The numbers of galaxies and fractions by morphology are shown in Table 4.1. Once the galaxy samples were established, we reviewed some of the fundamental relations already known for galaxies, which gave the following results:

1. Morphology–density relation (Figure 4.1); we obtain an excellent agreement with Dressler (1980).

2. Stellar mass distributions, both for the whole galaxy sample together and divided into morphological types. The stellar mass functions determined in cluster and field are the same for S0, all Sp, and SpE galaxies, while for all types together, ellipticals, and late spirals, slight differences are found (due to ellipticals).

3. In a color–magnitude and color–mass diagram (Figure 4.4), early types in clusters and the field are grouped in the red cloud, while cluster late types cover a larger color region. Figure 4.5 shows that ellipticals and late spirals in clusters and the field exhibit similar colors at fixed mass, while S0s and early spirals are redder in clusters than in the field, for all masses.

4. Color–environment. Brighter and more massive galaxies are the reddest (Figure 4.4). Galaxies located in higher LD environments are also redder (Figure 4.6). If separated by morphology, basically there is no trend of galaxy color with clustercentric distance.

5. Fractions of SF galaxies. SF galaxies are defined as having $\mathrm{SFR}_1 > 10^{-3}\ \mathrm{M}_\odot\ \mathrm{yr}^{-1}$. 70% of field galaxies are SF, while in clusters they are only 34%. When separated by morphology, it is clear that there are higher SF fractions for later types (Table 4.5), larger clustercentric distances, and lower LDs (Figure 4.12). On the other hand, fractions are almost flat as a function of cluster mass (Figure 4.13).

6. Phase–space diagrams of SF and quenched galaxies (Figure 4.10). A clear trend is found where quenched and earlier types are located deeper within clusters, while later types and SF galaxies populate more recent infall regions (Figure 4.11).

7. MS. The SFR–mass relations by morphology are displayed in Figure 4.14. The MSs of elliptical and S0 galaxies are flatter and have more dispersion than those of SpE and SpL, both in clusters and the field. The scatter around the MSs of cluster spirals is larger than for those in the field. This is evidence that the cluster environment can both enhance and reduce SF activity.

5

STAR FORMATION HISTORIES AND QUENCHING

One of the properties most influenced by the cluster environment is, surely, galaxy morphology. Several works, starting with the one by Dressler (1980), but also Postman & Geller (1984), Houghton (2015), have shown that galaxy morphology is strongly affected by the local environment, with early types being more common at high LD values and, more specifically, in the innermost regions of clusters. For this reason, if a cluster galaxy is still observed with a spiral or, more generally, a late-type morphology, this likely means that it entered the cluster environment relatively recently, i. e., a few Gyr ago, at most [e. g., Mamon et al. (2019)]. On the other hand, there are physical mechanisms, such as RPS and starvation, that also affect the stellar content and the ability of a galaxy to form stars and that act on shorter timescales [Boselli & Gavazzi (2006)].

In this chapter, we study if and how the star formation history (SFH) of a galaxy is affected by its local environment. To do so in the most unbiased way possible, we analyze the major drivers of the SFH of galaxies: morphology [e. g., Schawinski et al. (2014), Guglielmo et al. (2015)], stellar mass [e. g., Kauffmann et al. (2003a), Sánchez-Blázquez et al. (2006)], and environment [e. g., Vulcani et al. (2012), Guglielmo et al. (2015)]. We include our work [Pérez-Millán et al. (2023)], and quantify the effects of stellar mass, morphology, and environment (i. e., cluster, field) on the SFR. We then search for the effects of more subtle, second-order, agents, such as neighbor interactions, LD, clustercentric distance, and cluster mass. We also look into other manifestations of the SFH, such as present-day fractions of SF galaxies, and quenching indices, as introduced below.

When considering the overall life span of galaxies, to better visualize differences in the SFH, it is useful to normalize the SFR in each bin to the oldest one (SFR_4). Given that the bulk of the total stellar mass of galaxies is usually formed at early epochs, this representation is similar to the sSFR (i. e., the SFR divided by the corresponding stellar mass). This procedure allows us to explore how SF activity has changed over time, relative to its initial value, while fixing other important properties, such as the morphological type, galaxy mass, and cluster properties, among other parameters.

Furthermore, to better detect and quantify variations in the SFH, we define a "*quenching index*", i. e., the ratio between the SFRs in different, usually contiguous, age bins:

$$S_{i,j} = \frac{SFR_i}{SFR_j}, \tag{5.1}$$

with $i > j \in [1, 4]$ (see Table 3.1 for the age bins definitions). With quenching indices thus defined, $S_{i,j} > 1$ indicates a diminishing SFR in time. Different values of this index quantify diverse quenching (or enhancement, if $S_{i,j} < 1$) intensities, and can be used to quantitatively compare the SFH of galaxies with varied properties and in disparate environments. Hence, $S_{4,3}$ is a proxy of the initial build-up efficiency of the stellar mass. $S_{3,2}$ can be used to quantify changes involving earlier epochs, when the galaxy was likely in the first stages of interaction with the cluster environment, while $S_{2,1}$ is related to the current epoch quenching timescale.

Hereafter, whenever needed, quoted uncertainties on the mean SFRs and quenching indices are evaluated with the bootstrap resampling method (see Appendix C). SFHs are plotted as a function of the age of the galaxy stellar populations or lookback time, i. e., 10 Myr corresponds to the most recent lookback time, and 10 Gyr to the oldest.

5.1 SFH AND MORPHOLOGY

A connection is known to exist between morphology and the SFH [e. g., Kennicutt et al. (1989)]. This is observationally suggested by the colors of galaxies of different Hubble types (see e. g., Figure 4.5) and by spectral analysis [e. g., Garcia-Benito et al. (2017)], and is found in cosmological simulations as well [e. g., Tacchella et al. (2019)]. Here, we analyze how the SFHs depend on morphology for cluster galaxies; we also compare those SFHs with the ones of field galaxies.

Figure 5.1 presents the SFHs of cluster and field galaxies, divided into the four main morphological classes. In the left panel, it is possible to discern a sequence in both the average values of the SFR and the slopes, as a function of morphological type. The average value of SFR_4, which is a quite good proxy for the total stellar mass, diminishes monotonically from ellipticals to SpL, hence confirming the already known morphology–mass relation [e. g., Vulcani et al. (2011), Calvi et al. (2012), Wilman & Erwin (2012), but see also the mass distribution as a function of morphology for the sample in this work, presented in Figure 4.2]. This is even more evident in the right panel of Figure 5.1, where the SFR at each epoch is normalized by the oldest one. What we observe here is a consequence of both downsizing (more massive galaxies are quenched at earlier epochs) and morphology.

At fixed morphology, the average normalized values of both SFR_1 and SFR_2 are systematically higher for field galaxies, reflecting a recent quenching effect (or tendency) of the cluster environment. The SFR at earlier cosmic epochs is similar in

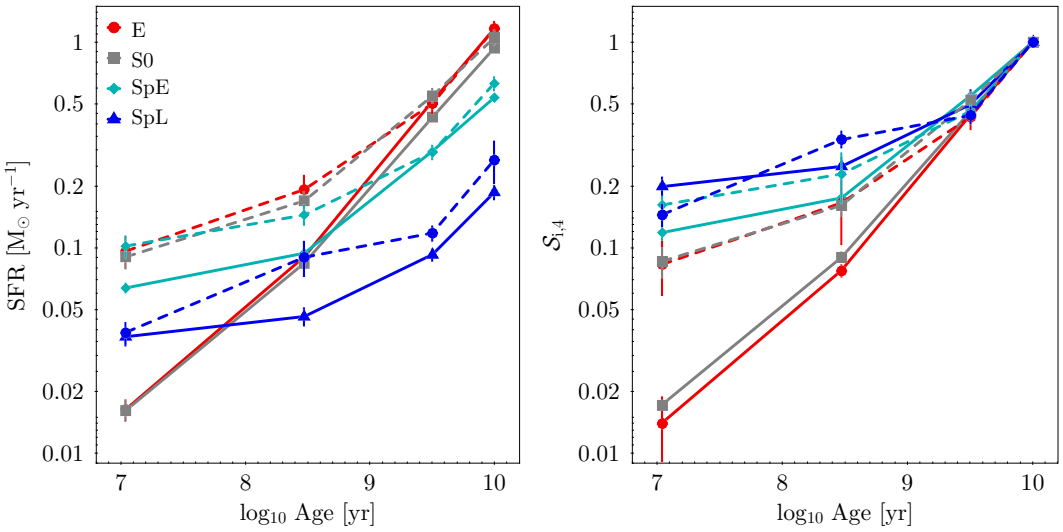

Figure 5.1: *Left:* SFHs for the final sample of cluster (*solid lines*) and field (*dashed lines*) galaxies, divided into the main galaxy morphological types. *Right:* $S_{i,4}$ quenching indices, i. e., SFHs normalized by the oldest age bin (SFR_4). See Table 3.1 for the definition of the SFR bins.

Table 5.1: Quenching indices for cluster and field galaxy samples, according to morphological type. Uncertainties were calculated with the bootstrapping method.

Environment	Index	E	S0	SpE	SpL
Cluster	$S_{4,3}$	2.25 ± 0.08	2.16 ± 0.18	1.82 ± 0.11	2.00 ± 0.19
	$S_{3,2}$	5.71 ± 0.42	5.12 ± 0.39	3.14 ± 0.23	2.00 ± 0.35
	$S_{2,1}$	5.51 ± 0.70	5.00 ± 1.09	1.47 ± 0.09	1.25 ± 0.14
Field	$S_{4,3}$	2.30 ± 0.36	1.91 ± 0.21	2.16 ± 0.18	2.20 ± 0.29
	$S_{3,2}$	2.62 ± 0.42	3.24 ± 0.47	2.02 ± 0.25	1.35 ± 0.28
	$S_{2,1}$	2.02 ± 0.66	1.87 ± 0.28	1.42 ± 0.34	2.27 ± 0.25

the two environments for all morphologies, as galaxies may not have yet entered the cluster at that time.

Differences in the SFH for the various morphological types are more clearly quantified with the quenching indices, presented in Table 5.1. The build-up of stellar mass at the earliest epochs, probed by the $S_{4,3}$ index, is remarkably similar in the four morphological classes and two environments here considered.

Differences are instead found when inspecting the values of $S_{3,2}$: we first notice that this index is much larger for Es and S0s than for spirals. Secondly, both Es and S0s

show important disparities between environments: the highest quenching indices are observed for both cluster ellipticals and S0s, and they are significantly higher than in the field. Spiral galaxies display in general lower $S_{3,2}$ values, indicative of a more constant SFH. Again, they are about 50% higher for clusters than in the field.

The quenching indices of late types for the most recent epochs ($S_{2,1}$) are generally much lower than those for earlier epochs (in line with what is presented later, in Section 5.2). The highest values are found in cluster Es and S0s; they can be up to three times larger than their field counterparts. Conversely, this index is very similar for cluster and field SpE, and 80% larger for SpL in the field than in clusters. This might be related to the shorter timescale probed by the recent SFR and will be discussed later on.

Finally, we note that SFR_1 is measurable for all types (Figure 5.1), even for early-type galaxies. Possible differences in the SFH of cluster and field ellipticals may also come from slight discrepancies in the mass distributions of the two (see Section 4.3), being weighted towards slightly more massive values for cluster ellipticals.

5.2 SFH AND STELLAR MASS

There is a known correlation between morphology and stellar mass, with higher mass galaxies having an increased probability of being ellipticals or S0s, rather than spirals [see, e. g., Vulcani et al. (2011)]. To isolate the effect of stellar mass on the SFHs, we group the galaxies in each of the four morphological classes into three mass bins. The result is shown in Figure 5.2.

Low-mass galaxies of all morphologies present a much flatter SFH than massive ones. In all mass bins, however, ellipticals and S0s have the steepest decline, and the difference in SFH between early- and late-types (i. e., spheroidals and spirals) is much more pronounced in the massive bin (although we should recall that the most massive galaxies in our sample are found among ellipticals and S0s).

The SFHs patterns agree very well, on average and from several points of view, with a downsizing scenario [Cowie et al. (1996)]. Consistently with previous well-known results [e. g., Brinchmann et al. (2004), Chen (2009), Guglielmo et al. (2015)], there is a correlation between galaxy mass and the slopes of the SFHs: less massive galaxies have flatter SFHs, reflecting a more continuous star formation process, while massive galaxies are dominated by old stellar populations, indicating a much quicker build-up of their stellar mass.

This result holds both for the whole sample (see Section 5.1) and for the different morphologies considered separately, which means that the SFHs of cluster and field galaxies are mainly dictated by their stellar mass. However, the environment may influence the (recent) SFH, as well as the quenching. In the following, we study environmental quenching, while trying to isolate the stellar mass.

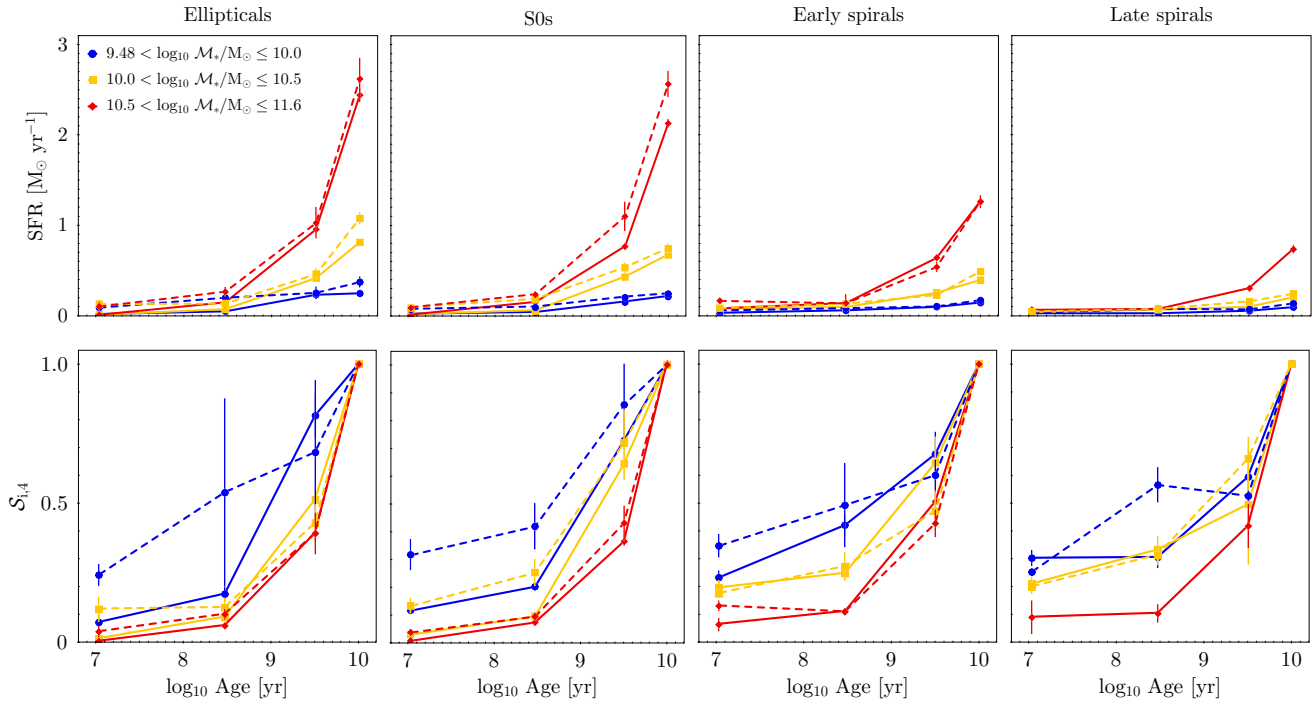

Figure 5.2: SFHs (*top row*) and SFHs normalized by the oldest age bin (*bottom row*), for the galaxy sample separated into bins of morphology and stellar mass, as named. *Solid lines:* cluster galaxies; *dashed lines:* field galaxies. Uncertainties are calculated using the bootstrapping technique. Dashed red lines in the rightmost panels are not shown, due to the small number of galaxies in this bin.

5.2.1 *Quenching in different environments*

Galaxies in the local universe are on a path that naturally brings them to become passive objects. Several works [see, e. g., Madau & Dickinson (2014), and references therein, for a review on the topic] have shown that the SFR density of the universe peaked at around $z \approx 2$ (approximately 10.2 Gyr ago; see Chapter 1), and has declined exponentially since then. Evidence suggests that both galaxy mass and environment (more significantly for lower mass galaxies) have a crucial role in galaxy quenching [e. g., Pintos-Castro et al. (2019)]. Using WINGS data, Guglielmo et al. (2015) found that, for $z > 0.1$, SFHs are similar for galaxies with the same mass, regardless of morphology. For $z < 0.1$, however, late-type galaxies have, on average, higher SFRs than early-types.

Here, we try to disentangle the effects of galaxy mass and environment on quenching. To this end, we calculate the quenching indices as in Table 5.1, but this time separating by stellar mass, as presented in Table 5.2, and plotted in Figure 5.3 with solid lines for cluster galaxies, and dashed lines for field ones.

Table 5.2: Quenching indices for the cluster and field samples, separated by morphology and divided into three bins of stellar mass: low ($9.48 < \log_{10} \mathcal{M}_*/M_\odot \leqslant 10.0$), intermediate ($10.0 < \log_{10} \mathcal{M}_*/M_\odot \leqslant 10.5$), and high ($10.5 < \log_{10} \mathcal{M}_*/M_\odot \leqslant 11.6$). Uncertainties are calculated with the bootstrapping method.

Environment	Type	Index	low mass	intermediate mass	high mass
Cluster	E	$S_{4,3}$	1.07 ± 0.05	1.95 ± 0.16	2.54 ± 0.12
		$S_{3,2}$	4.69 ± 0.56	5.58 ± 0.63	6.37 ± 0.76
		$S_{2,1}$	2.35 ± 0.28	6.10 ± 2.36	11.66 ± 6.94
	S0	$S_{4,3}$	1.37 ± 0.05	1.55 ± 0.10	2.75 ± 0.38
		$S_{3,2}$	3.60 ± 0.60	6.70 ± 0.96	4.93 ± 0.28
		$S_{2,1}$	1.71 ± 0.58	3.13 ± 0.80	9.01 ± 5.84
	SpE	$S_{4,3}$	1.48 ± 0.11	1.55 ± 0.16	1.97 ± 0.21
		$S_{3,2}$	1.60 ± 0.28	2.58 ± 0.44	4.51 ± 0.62
		$S_{2,1}$	1.80 ± 0.39	1.27 ± 0.28	1.70 ± 0.38
	SpL	$S_{4,3}$	1.68 ± 0.21	2.02 ± 0.33	2.39 ± 1.14
		$S_{3,2}$	1.94 ± 0.55	1.49 ± 0.41	3.96 ± 2.10
		$S_{2,1}$	1.01 ± 0.35	1.58 ± 0.52	1.15 ± 0.82
Field	E	$S_{4,3}$	1.46 ± 0.69	2.33 ± 0.60	2.55 ± 0.59
		$S_{3,2}$	1.27 ± 0.37	3.39 ± 0.82	3.83 ± 1.01
		$S_{2,1}$	2.21 ± 2.80	1.05 ± 0.24	2.59 ± 3.31
	S0	$S_{4,3}$	1.17 ± 0.19	1.39 ± 0.19	2.32 ± 0.41
		$S_{3,2}$	2.04 ± 0.59	2.85 ± 0.76	4.55 ± 0.98
		$S_{2,1}$	1.32 ± 0.34	1.89 ± 0.33	2.49 ± 1.28
	SpE	$S_{4,3}$	1.67 ± 0.20	2.08 ± 0.29	2.08 ± 0.22
		$S_{3,2}$	1.22 ± 0.34	1.72 ± 0.36	4.06 ± 0.54
		$S_{2,1}$	1.42 ± 0.40	1.97 ± 0.37	0.89 ± 0.15
	SpL	$S_{4,3}$	1.90 ± 0.10	1.52 ± 0.42	–
		$S_{3,2}$	0.93 ± 0.47	2.10 ± 0.28	–
		$S_{2,1}$	2.23 ± 0.23	1.56 ± 0.29	–

The $S_{4,3}$ index, which reflects the early build-up of stellar mass, shows, on average, higher values for larger stellar masses, and monotonically decreases from more to less massive galaxies. It is much less dependent on stellar mass for spirals than for ellipticals or S0s and is independent of the environment for all morphologies. For

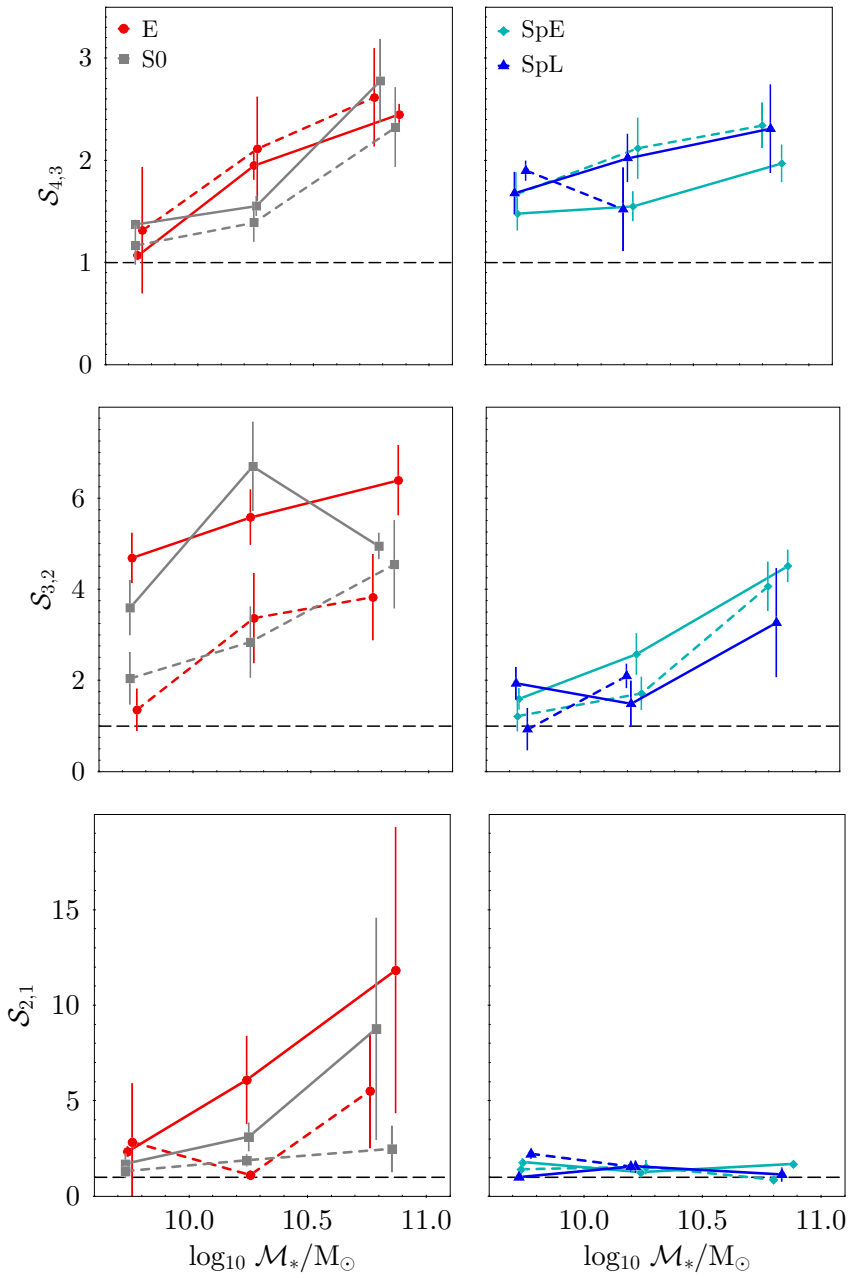

Figure 5.3: Quenching indices $S_{4,3}$ (*top row*), $S_{3,2}$ (*middle row*), and $S_{2,1}$ (*bottom row*), for early- (*left*) and late- (*r*ight) type galaxies in the cluster (*solid lines*) and field (*dashed lines*) samples, separated into bins of stellar mass. Quenching occurs if index $S_{i,j} > 1$, i. e., it lies above the long-dashed black line.

each morphological type and mass interval, the values are the same, within the errors, for field and cluster galaxies, hinting at a common formation scenario.

Following the analysis of the quenching indices, we find that the $S_{3,2}$ index, in general, increases with mass for all morphologies. At fixed morphology and stellar mass (see Table 5.2), the values are almost always higher for cluster galaxies than for their field counterparts, and nearly a factor of two for Es and S0s. Besides, indices for early types take generally higher values than for spirals. These differences in the quenching indices can be interpreted as a pure, direct, consequence of environmental mechanisms.

Differences induced by the environment are more subtle for spirals; for them, mass dominates over the environment. Once the mass effect is taken into account, what is left can be attributed to the physical processes happening in clusters. The fact that spirals are the same in clusters and the field, within the errors, suggests that the time scales needed for quenching to be effective are larger than the $\sim$ 570 Myr probed by our second age bin (see Table 3.1). At older ages, morphological transformations are more effective, and we likely observe strongly quenched spirals as S0s.

Quenching effects on the most recent SFR, probed by $S_{2,1}$, are evident in ellipticals and S0s in clusters, hinting again at the fact that both stellar mass and environment are acting to quench star formation. For early types, $S_{2,1}$ indices are lower in the field than in clusters, implying that the cluster environment is causing the quenching in this case. At the same mass bins, the $S_{2,1}$ index presents the largest differences between early types and spirals; this is likely a consequence of the fact that the percentage of *bona fide* quenched galaxies is much lower for spirals than for early-types. Possible differences in the values of $S_{2,1}$ for spirals in clusters and the field are much less evident and seem to be dominated by stochastic variations, due to the very nature of the SFR_1. However, in general, $S_{2,1}$ is lower than $S_{3,2}$ for spirals, at any given mass. Possible explanations for this will be proposed later on, and they involve mechanisms typically found in clusters that can both promote or hinder star formation activity on short timescales.

Guglielmo et al. (2015) analyzed a sample of cluster and field galaxies using WINGS and PM2GC data, and found a surprising similarity, at fixed mass and environment, between galaxies of different morphological types in their SFHs. The findings of that paper are quite counterintuitive and unexpected since early morphological types are known to be characterized by strong bursts of star formation mostly at the beginning of their formation, while late types present SF episodes throughout their lifetime. Conversely, our investigation through the quenching indices finds non-negligible differences as a function of morphology, more in line with what is commonly found in the literature [see e. g., Kennicutt (1998), Eales et al. (2017)]. Several factors might explain these divergent results. First of all, quenching indices (see Figure 5.3 and Figure 5.6 below), defined as ratios (Equation 5.1), are well suited to highlight differences in the SFR at different epochs. Secondly, via our use of OmegaWINGS data, we include outer parts of the clusters; these contain larger fractions of late-type galaxies that have a short history of interactions with the cluster itself. Finally, the fact

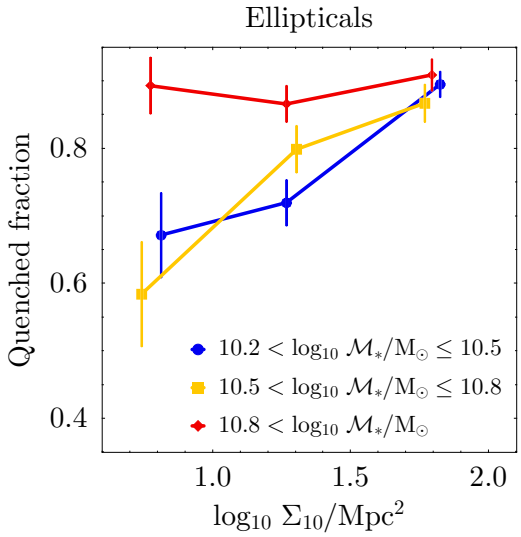

Figure 5.4: Quenched fraction of massive elliptical galaxies as a function of local density, divided into bins of stellar mass. Most massive ellipticals are quenched, regardless of local environment density.

that we do not apply aperture corrections affects late and early types differently, since the latter generally display flatter radial color gradients.

Peng et al. (2010) showed that the quenched fraction of massive elliptical galaxies is independent of environmental density. We test that result by calculating the quenched fraction of ellipticals in different bins of stellar mass, as shown in Figure 5.4. We find that the quenched fraction depends on LD for low-intermediate mass galaxies, but it reaches the highest values ($\sim$ 88%) for the most massive ellipticals ($\log_{10} \mathcal{M}_*/\mathrm{M}_\odot > 10.8$), regardless local density.

5.3 SFH AND PROJECTED DISTANCE

The comparison previously carried out between the SFH of field and cluster galaxies has clearly demonstrated and quantified how the environment can affect the ability of galaxies to form stars. In what follows, we look into the mechanisms that are responsible for this in more detail, through the analysis of the recent SFR (SFR_1 and SFR_2).

Paccagnella et al. (2016) have studied the changes in the SFR–mass relation for WINGS/OmegaWINGS galaxies, as a function of the clustercentric distances. Here, we extend this analysis; we investigate possible effects due to morphology, and explore differences in the older stellar populations, with a particular focus on SFR_2. This parameter samples star formation processes that most likely happened during the first galaxy-cluster interaction for the recently accreted population. To this end, we

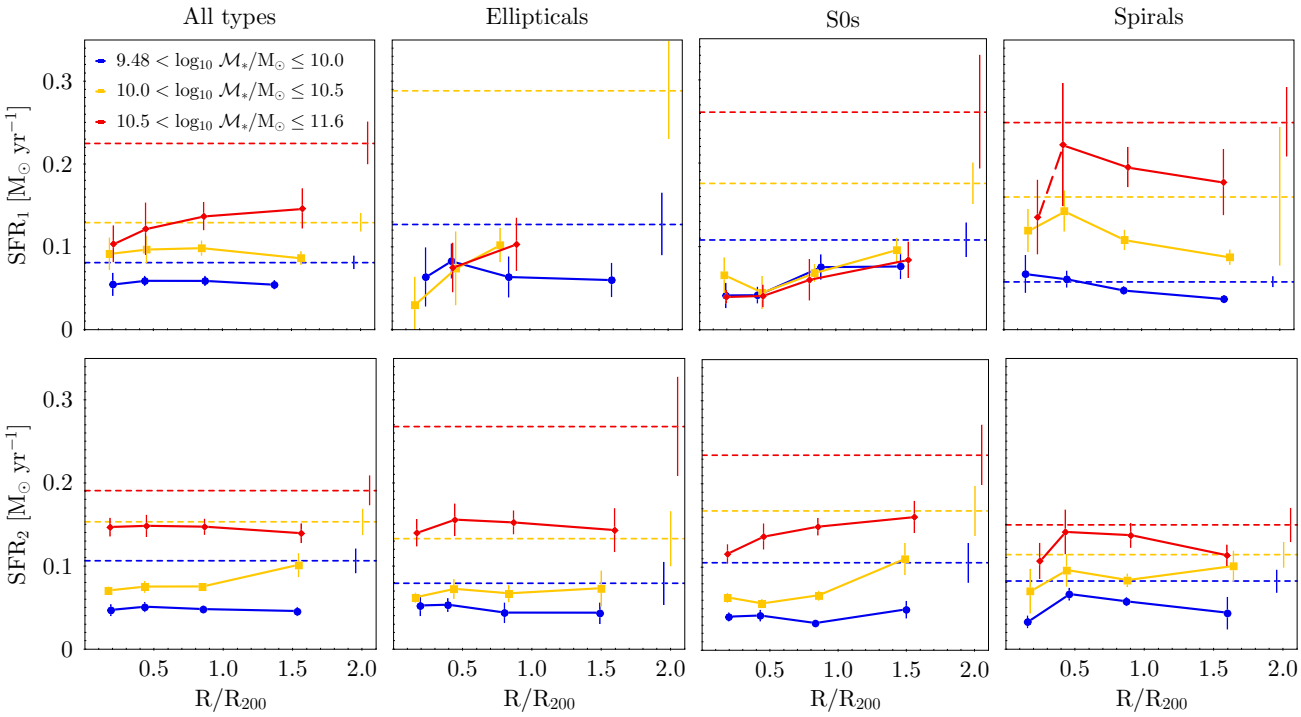

Figure 5.5: SFR *versus* mean clustercentric distance for the final sample, in bins of stellar mass, denoted by different colors (see legend in the top left panel), and separated by morphological class: all types (*left)*, ellipticals (*center left)*, S0s (*center right)*, and spirals (*right)*. *Top row:* SFR_1 (only actively SF galaxies in the sample). *Bottom row:* SFR_2 (full galaxy sample). *Solid lines:* cluster galaxies; *dashed lines:* field galaxies. The *long-dashed red line* in the top right panel means that the number of SF, massive, cluster spirals in the bin closest to the center is very small, and this trend should be taken with caution. The rightmost panels show all spirals (and irregulars) together, to have enough numbers in each bin.

will consider spiral galaxies as one unique population, making no distinction between early and late types, to avoid poor statistics.

In Figure 5.5, top row, we show the mean SFR_1 of SF galaxies (see Section 4.7), divided into four bins of morphology and three bins of mass, denoted with different colors, as a function of distance to the host cluster center, normalized by R_{200}. In the bottom row, we display the mean SFR_2 of the whole sample, regardless of SFR_1 value, also as a function of clustercentric distance. From left to right, the columns present data for all morphological types together, ellipticals, S0s, and spirals, respectively.

In the top left panel (average SFR_1 for SF galaxies of all morphological types), we observe roughly flat trends as a function of distance, except for the most massive bin, for which SFR_1 decreases towards the center. When separating into different morphologies, SFR_1 declines with diminishing distance for S0s and for ellipticals of

intermediate masses (note that the statistics are poor for Es in the cluster outskirts). Interestingly, the SFR-mass relation –on average– seems to break down in this representation. SFR_1 appears only weakly correlated with stellar mass for early types, while a dependency still holds for late types (see also Figure 4.14). Regarding the trend with distance, in the case of spirals, SFR_1 grows for all masses towards the center, up to a clustercentric distance of 0.5 R_{200}. At smaller distances, where the virialized population dominates over infalling galaxies, there is a possible hint of a decreasing SFR_1 with smaller distances for high- and intermediate-mass galaxies. Although this observed tendency is driven by a small number of galaxies, it is confirmed by bootstrap resampling analysis (see Appendix C). These late-type galaxies, having preserved their spiral morphology, may have also kept a substantial fraction of their gas until close to the center, and the high-density medium there may have stimulated vigorous star formation, through hydrodynamical or gravitational interactions.

We also observe, in some cases, large offsets between cluster and field SFRs. In principle, SFRs at large clustercentric radii should reach the field values. However, this trend is likely diluted, since the number of galaxies with $R/R_{200} > 2.0$ is small (see Figure 2.3). There is also some probability that we are including galaxies in filaments reaching the cluster, and hence in fact sampling an environment that is very different from the field.

We analyze SFR_2 in a similar way (Figure 5.5, bottom row), to search for possible effects of the environment on stellar populations at older ages. With this aim, we consider all galaxies in the sample (not only actively SF ones). First, we observe once again that field galaxies have on average a higher SFR_2 than cluster members in the same mass bin, most evidently in the case of spheroidal galaxies. The differences between field and clusters, though, are smaller than for SFR_1. Taking all the morphological types together (leftmost panel), galaxies within 1 R_{200} show a roughly flat SFR_2 at any mass. Unlike what is observed for SFR_1, when separating by morphology, the SFR-mass relation is again in place, with a clear trend between mass and SFR.

The run of SFR_2 with distance is again flat for Es (second panel) of all masses. As for S0 galaxies (third panel), SFR_2 is higher for larger distances and high and intermediate masses. In spiral galaxies, SFR_2 increases slightly between the cluster outskirts and distances of 0.5 R_{200}, but it drops closer to the cluster center.

Despite the tenuous environmental effects, the quenching indices can help disentangle the influence of environment and mass. We hence analyze quenching indices as a function of stellar mass, separated into four bins of clustercentric distance and for the field, both for all the galaxies in the sample at once, and separated by morphology (Figure 5.6).

We obtain several interesting results. $S_{4,3}$ does not show important differences between field and cluster galaxies, at any clustercentric radius, again hinting at a common formation scenario for most galaxies in the past. Quenching at these ages is

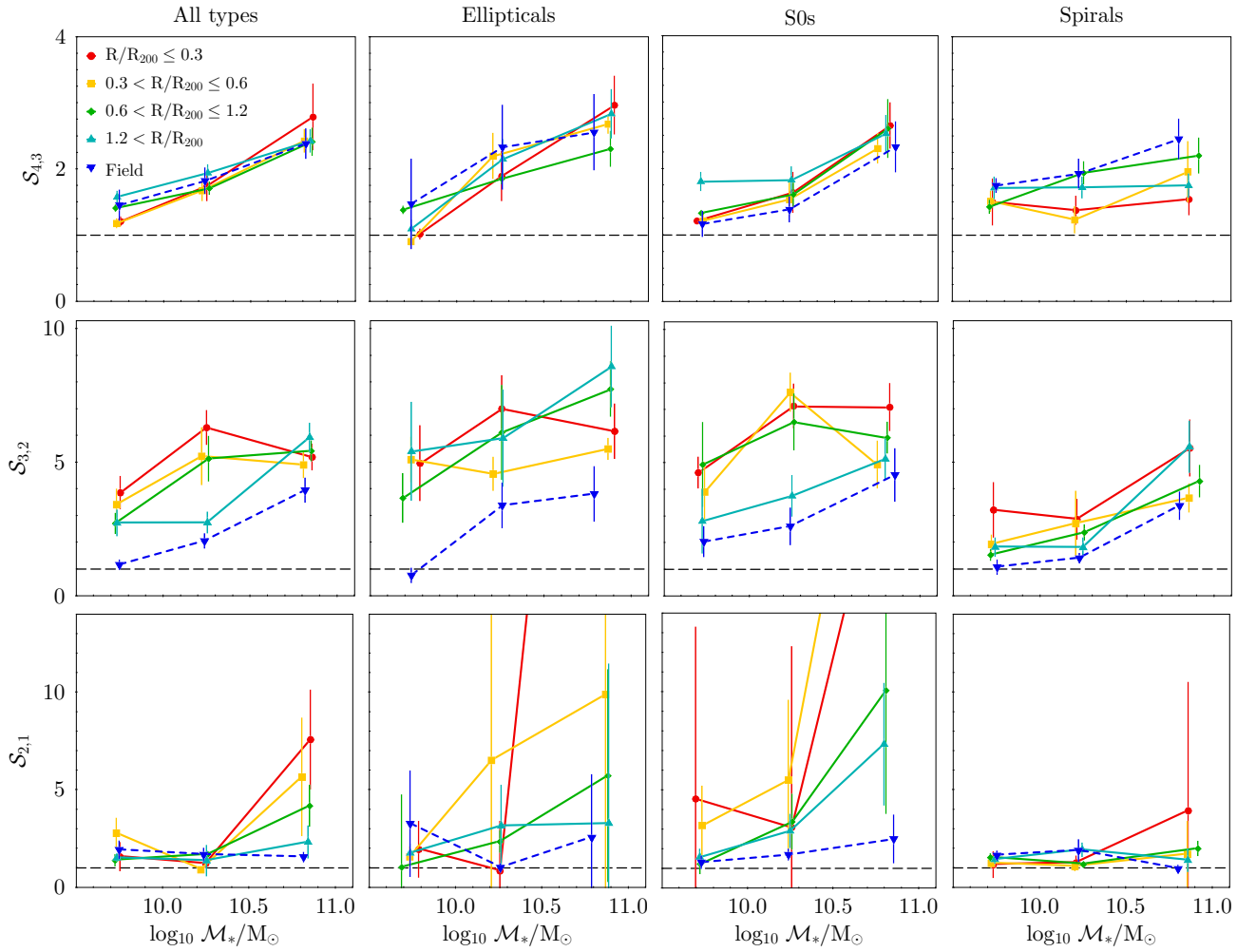

Figure 5.6: Quenching indices $S_{4,3}$ (*top row*), $S_{3,2}$ (*middle row*), and $S_{2,1}$ (*bottom row*), as a function of stellar mass, for the galaxy sample in clusters (*solid lines*, divided into bins of clustercentric distance, indicated by different colors) and the field (*dashed lines*). *Left:* all morphological types together; *center left:* ellipticals; *center right:* S0s; *right:* spirals. The long-dashed black horizontal line separates quenching (above) from enhancement (below).

a function of stellar mass for early types (i. e., downsizing), while for late types it is flatter, consistent with a less steep SFH. For $S_{3,2}$, a mild tendency with clustercentric distance is observed for every morphology. The largest differences in this index between cluster and field galaxies occur for early types, which have been highly affected by the cluster environment. As for late types, we start to see a stronger quenching closer to the cluster center, in projection; for field spirals, on average, quenching is lower. This is somewhat expected: the location of a spiral galaxy with respect to the cluster center is a transient property. Finally, the most recent quenching

index ($S_{2,1}$) acquires its higher values for early types, being highest for the most massive galaxies located very close to the cluster center. Once again, spiral galaxies display no clear trend with distance, and quenching is similar for both cluster and field late types in these age bins.

We can say that *stellar mass quenching* (as mentioned at the end of Section 1.3) is the most important factor turning off star formation activity at almost all epochs. On the other hand, *environment quenching* is a secondary agent, but once the effect of mass is isolated, the quenching effects of the environment are still discernible.

5.4 SFH AND LOCAL DENSITY

Controversial results have been found when analyzing the relation between SFR and LD [see, e. g., Pintos-Castro et al. (2019)]. Tyler et al. (2013) found no differences in the SFR distribution as a function of LD between cluster and field galaxies, while, e. g., Calvi et al. (2018) did.

The existence of a relation between LD and SFH might provide insights into the mechanisms that affect stellar populations, whether due to the influence of the cluster in general or caused by the higher density of galaxies. Of course, the LD of galaxies is a function of clustercentric distance (see Figure 2.3, left column): the closer to the cluster center, the probability of finding a high number of galaxies per unit area is higher [Fasano et al. (2015), and also our Figure 2.3]. Thus, disentangling the possible effects of galaxy position within the cluster from those of the higher galaxy density is definitely not straightforward.

To explore the possible influence of the LD, we look at the mean SFR_1 of SF galaxies, and at SFR_2 for the whole galaxy sample, separated into bins of stellar mass, as a function of LD, divided into three ranges: $\log_{10}\ \Sigma_{10}/\mathrm{Mpc}^2$ = -0.05 – 1.0, 1.0 – 1.5, and 1.5 – 3.0 (as shown in Figure 2.3). We present the result in Figure 5.7, for both cluster members (solid lines) and field galaxies (dashed lines). For the latter, the average SFR_1 and SFR_2 do not change significantly with LD, but the span of LD values is significantly smaller (the mean $\log_{10}\ \Sigma_{10}/\mathrm{Mpc}^2 = 1.4$ for cluster members, while it is 1.0 for field galaxies). For this reason, for field galaxies, we ignore the LD and consider only the average SFR in each stellar mass bin.

When not separated by morphology, the SFR_1 (Figure 5.7, top row) of field galaxies is always higher, at fixed LD and mass, than for their cluster counterparts. This is also true for ellipticals and S0, examined separately, but not for spirals. Taking all morphological types together, SFR_1 is insensitive to LD for galaxies in the lowest mass bin, while a decreasing trend with increasing LD is observed for intermediate and high mass objects ($\log_{10} \mathcal{M}_*/\mathrm{M}_\odot \gtrsim 10.0$). This effect is strongest for the most massive bin. As for ellipticals, trends of SFR_1 with LD are not clear. For the low and high mass bins, SFR_1 seems flat, while it decreases for intermediate mass galaxies in the highest

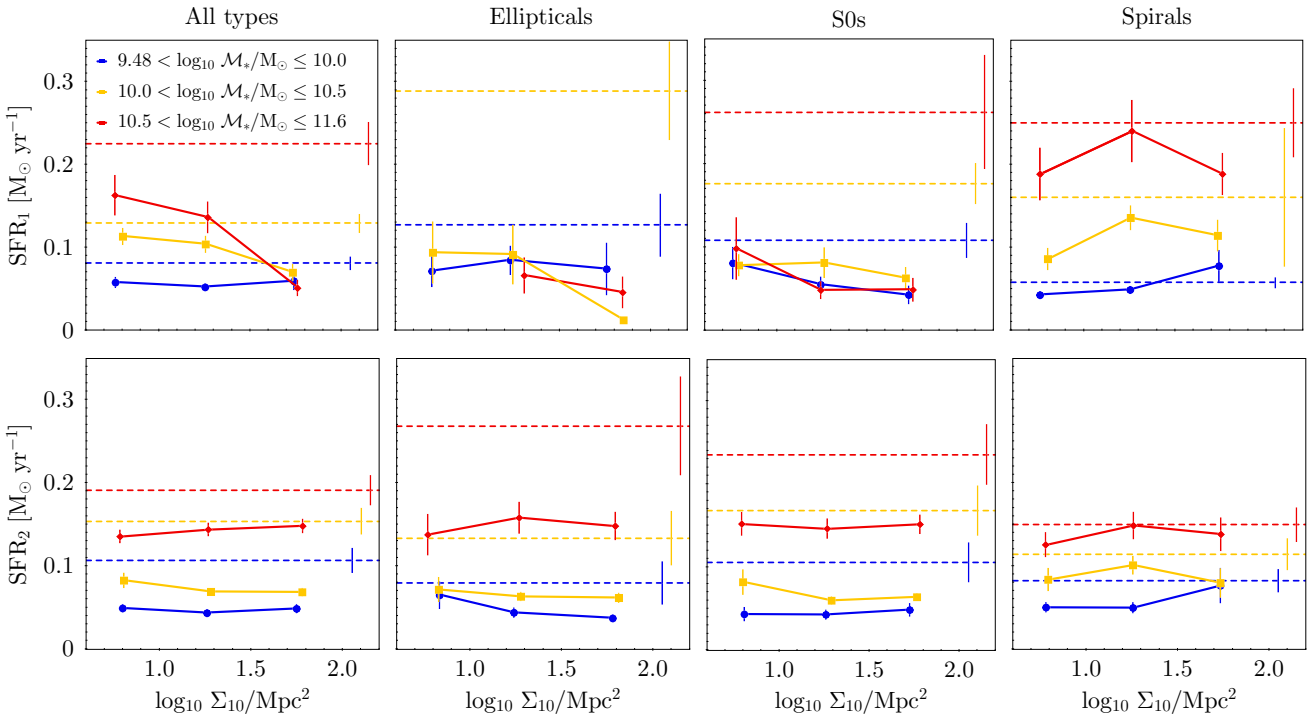

Figure 5.7: SFR_1 of SF galaxies (*top row*), and SFR_2 for the whole galaxy sample (*bottom row*), *versus* LD, separated into bins of stellar mass, as in Figure 5.5.

LD bin. The lack of a trend at high mass may be due to the scarcity of such objects at low LD.

Regarding S0s, the result mirrors the one found for distance: SFR_1 decreases in denser regions and does not depend on stellar mass. Ellipticals and S0s, being the most numerous types, drive large-scale trends. Concerning spirals, SFR_1 grows with increasing density in low- and intermediate-mass galaxies. In the case of massive ones, the confidence intervals are larger and we only have a few objects. This result, once again, reflects the trends already spotted for late-type galaxies as a function of clustercentric distance.

When the SFR_2 is inspected (Figure 5.7, bottom row), no correlation with LD is detected: even when galaxies are divided according to their morphologies, the run of SFR_2 with LD is consistent with being flat. A possible explanation is that LD is a quantity that varies with time; what we see is highly dependent on the past LD values, averaged over time. It is clear, instead, that SFR_2 is different for cluster and field galaxies: cluster galaxies have systematically lower SFR_2, at all masses. This is especially evident for earlier types. For spirals, the difference is more subtle, and it almost vanishes for the highest mass bin.

5.5 THE INFLUENCE OF THE NEAREST GALAXY

Park & Hwang (2009) have used the distance to the most luminous neighboring galaxy as a means to study the effects of galaxy–galaxy interactions –hydro-dynamical, gravitational, and of tidal nature–, versus those of the large scale environment, on the properties of galaxies in clusters [but see also Park & Choi (2009), for an analysis of galaxies in lower-density environments]. Those papers explore the influence of the closest neighbor galaxy on properties, such as luminosity, color, and $EW_{H\alpha}$. Park & Choi (2009), in particular, find that: "late-type neighbors enhance the star formation activity of galaxies while early type neighbors reduce it, and [...] these effects occur within $R_{vir,\,neig}$". Here, we carry out a similar analysis, by testing the occurrence of variations in luminosity, color (*u*-r), and SFH, as a function of the morphology of the nearest cluster member galaxy and its projected distance, normalized by its virial radius, as defined in subsection 2.2.2.

It should be highlighted that, here, we only use galaxies that are spectroscopically confirmed members, and we do not restrict by the relative radial velocities of the galaxy pairs, as we do not know the real 3D velocities. Since the spectroscopic completeness is not 100%, the results we present in what follows are to be considered as lower limits to the ones we would be able to detect in ideal conditions. We define four bins for the distance to the nearest neighbor: $R/R_{vir} = 0.1-1.0$, $1.0-2.5$, $2.5-6.0$, and > 6.0 (as shown in the right column of Figure 2.3). Regarding morphology, we only separate into early and late types, for both subject galaxies and neighbors, to compare with the results of Park & Hwang (2009) and Park & Choi (2009).

First, we analyze whether the luminosity of a given galaxy is affected by its closest neighbor, given its distance and morphology. We do not find any remarkable dependence of the weighted mean (or median) luminosity (absolute magnitude in the *V* and *B* bands), as a function of either morphology or distance of the closest neighbor.

On the other hand, when rest-frame colors ($M_B - M_V$; Figure 5.8) are considered, late-type galaxies with an early-type neighbor closer than one virial radius are, on average, slightly redder (~ 0.034 mag) than those with a late-type neighbor within the same distance. For the closest early-type neighbors located further away than one virial radius, the average color is practically unchanged. No differences are found for early-type galaxies, regardless of the type and distance of their neighbors.

Repeating the same analysis for the SFH, we do not observe any significant trend or difference in the median SFR_2, SFR_3 or SFR_4, neither for early nor for late-types, as a function of neighbor morphology or distance. The distribution of SFR_1 instead, does show significant differences in the average weighted values. For early-types (Figure 5.9, top left), the average SFR_1 decreases with diminishing neighbor distances, both for early- (the number of galaxies is 387, and 884 when weighted) and late-type (115 galaxies, 259 weighted) neighbors. The effect is slightly more pronounced for early types with an early-type neighbor within one virial radius, albeit the trend is

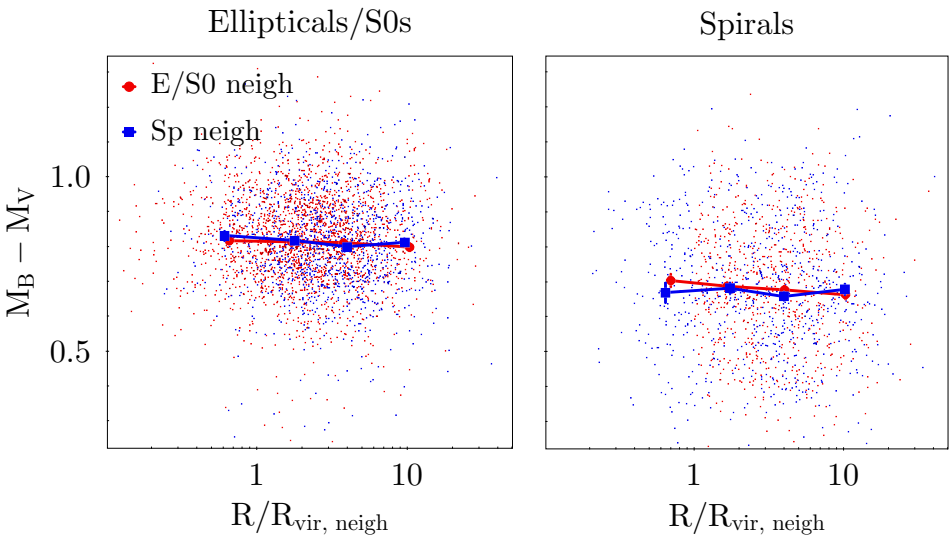

Figure 5.8: Rest-frame color of galaxies with early (*left*) and late (*right*) morphologies, as a function of normalized separation. *Red/blue* points indicate whether the closest neighbor is an early-/late-type galaxy. *Solid red/blue lines:* color weighted means. Error bars are calculated with the bootstrap resampling method. The color distribution is flat, as a function of neighbor distance.

only marginal, as accounted for by the large confidence intervals estimated by the bootstrap resampling method.

For late-type galaxies (Figure 5.9, top right), the mean SFR_1 increases for close pairs, when the target galaxy is within one virial radius of a late-type (46 galaxies, 78 weighted), but it remains constant as a function of distance if the neighbor is an early-type (116 objects, 201 weighted). The mean SFR_1 is twice higher for a late-type companion than for an early-type neighbor. The same behavior is observed when the median value of the SFR_1 is considered.

If the $S_{2,1}$ index is evaluated instead (Figure 5.9, bottom row), quenching increases monotonically for early-type galaxies with diminishing distance to the closest neighbor, regardless of neighbor type, up to one virial radius. If the companion is another early type, quenching increases significantly within one virial radius; if the companion is a spiral, quenching flattens. As for late types (bottom right panel), $S_{2,1}$ is also mostly flat with neighbor separation, and independently of companion morphology, with values close to 1, unless the target galaxy is located within one virial radius of the companion: spirals with early-type neighbors have quenching indices higher than those with another spiral neighbor.

In Figure 5.10, we report the fraction of SF galaxies as a function of neighbor distance and type. In the case of early types (left panel), the fraction of SF galaxies drops, from approximately 29% to 19%, when a galaxy is closer than 1 neighbor virial radius, regardless of neighbor type. As for late-type galaxies (right panel), the SF fraction

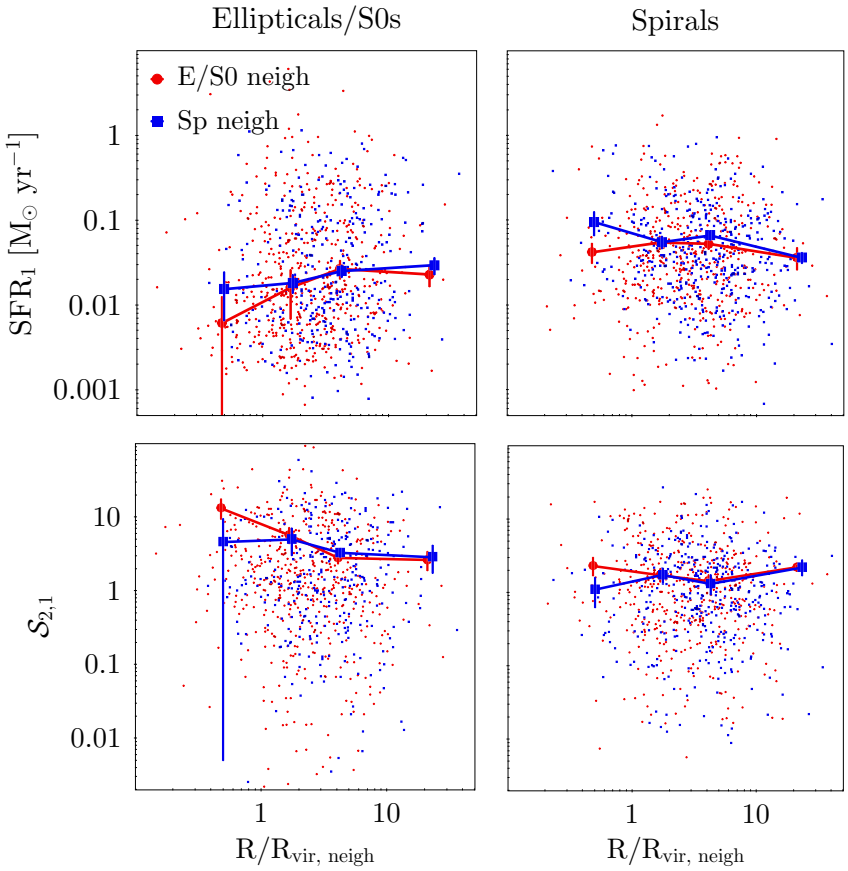

Figure 5.9: Weighted means of SFR$_1$ (*top row*) and quenching index $S_{2,1}$ (*bottom row*), for galaxies with early (*left column*) and late (*right column*) morphologies, as a function of normalized neighbor separation. Colors and error bars as in Figure 5.8.

is higher for a late-late pair than for a late-early pair, by a factor of about 10%, at all neighbor distances. However, independently of neighbor type, the SF fraction is lower when the pair separation is smaller than one virial radius of the companion. Fractions of actively SF galaxies decrease with diminishing distance, from 65% to 51% for spiral–spiral pairs, and from 58% to 41% for spiral–early-type pairs.

This analysis seems to indicate that the distance and morphological type of the closest neighbor have a clear influence on the current star formation rate of a given galaxy. However, we have found no dependence of $S_{4,3}$ and $S_{3,2}$, the oldest quenching indices, on neighbor distance and/or morphology. This would be consistent with the fact that galaxy encounters are short-lived events that might leave signatures only on short time scales; some encounters will have a positive effect, and others a negative one, on the SFR. Also, close neighbors today were not necessarily so a few Gyr ago.

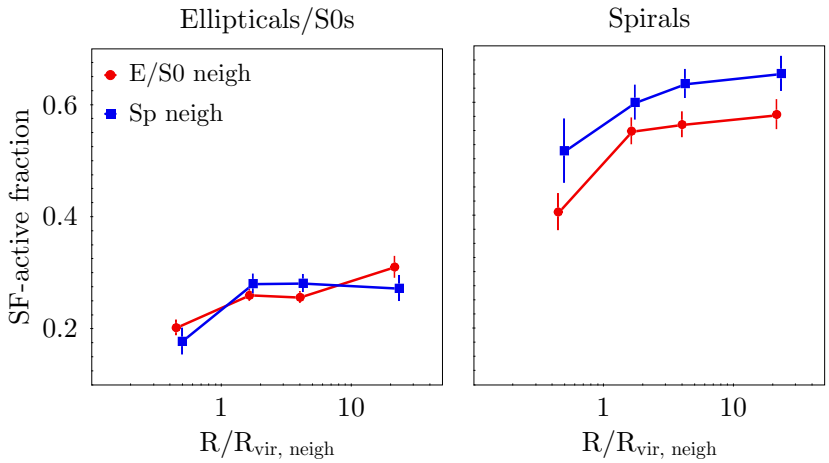

Figure 5.10: Fractions of SF early- (*left*) and late-type (*right*) galaxies, as a function of distance to the closest neighbor. Colors as in Figure 5.8. Error bars represent binomial errors.

5.5.1 *Local environment or neighbor proximity?*

A direct effect of the morphology–density relation (see Section 4.2) is the fact that early-type galaxies are more likely found towards the centers of clusters. Hence, reversing the argument, there is a higher probability that a galaxy with an early-type closest neighbor is located in the innermost parts of clusters. In an attempt to account for the modulation of the environment on the influence of neighbor galaxies, we now analyze the stellar population properties of early-type and spiral galaxies, as done before, but this time separated into low ($\log_{10}\,\Sigma_{10}/\mathrm{Mpc}^2 \leqslant 1.2$) and high LD ($\log_{10}\,\Sigma_{10}/\mathrm{Mpc}^2 > 1.2$) bins.

In the top row of Figure 5.11, we show the dependence of the average SFR_1 on the distance and morphology of the closest neighbor, for early-types and spirals, in both low and high LD environments. Early types in a low LD environment, with another early-type closest neighbor, present only slightly lower SFR_1 than those early types with a spiral closest companion, for all neighbor separations. At high LD and one virial radius or less neighbor separation, however, the SFR_1 of an early-type with an early-type nearest neighbor is 3.7 times smaller than for an early-type with a spiral companion.

Now, for spirals in low LD, SFR_1 grows by a factor of three when the neighbor galaxy is another spiral with a separation smaller than one virial radius of the companion. Statistics for spiral-spiral pairs in low LD are lowest, with 14 target galaxies, and 20 weighted. If, however, the neighbor is an early-type (24 objects, 31 weighted), SFR_1 drops by up to a factor of seven (in both cases, the comparison is made with the average SFR value when the neighbor is ~ two or more virial radii away).

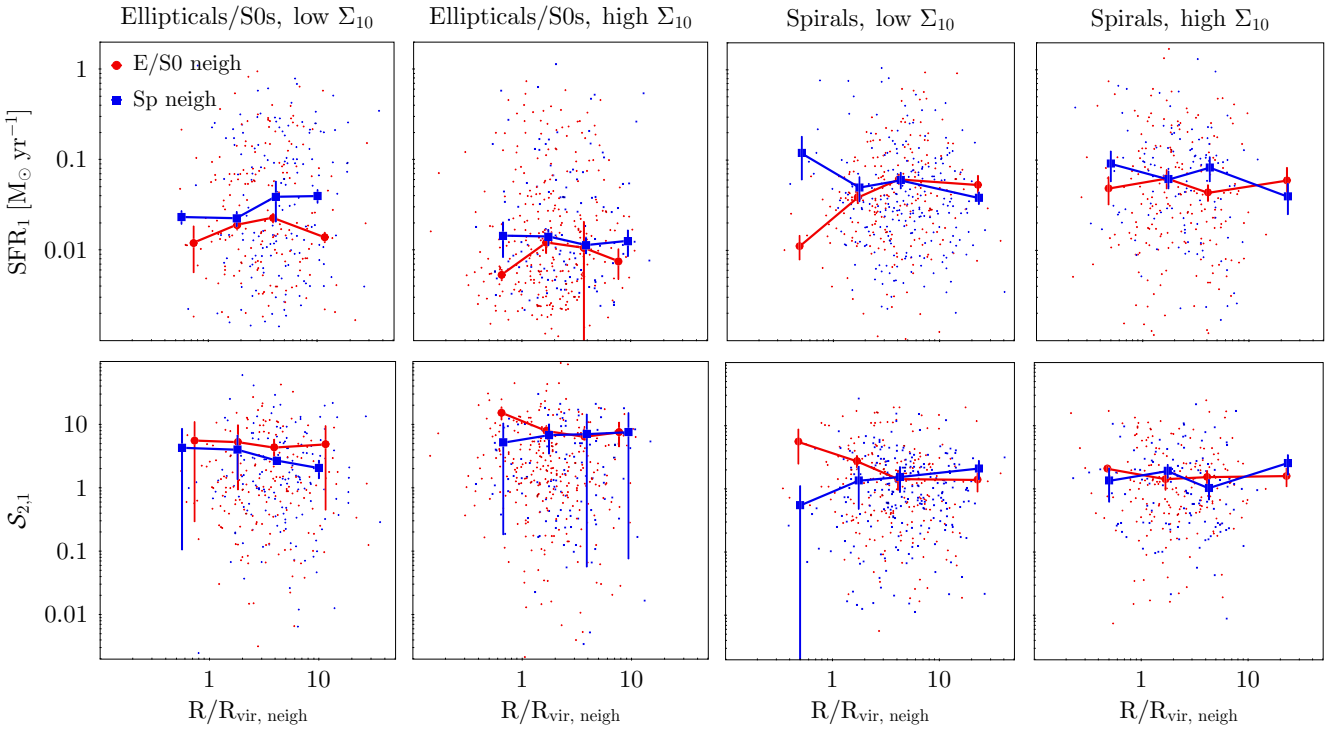

Figure 5.11: Weighted means of SFR_1 (*top row*) and quenching index $S_{2,1}$ (*bottom row*), as a function of normalized separation to the closest neighbor. *Left:* early-types, low LD; *center left:* early-types, high LD; *center right:* late-types, low LD; *right:* late-types, high LD. Colors and error bars as in Figure 5.8.

Conversely, for spirals in high LD environments, SFR_1 is flat, on average, regardless of the morphology and distance of the closest neighbor (in this environment, 30 target spirals, 55 weighted, have a late-type neighbor, while 88 spirals, 182 weighted, have an early-type companion).

On the other hand, SFR_2, SFR_3, and SFR_4 are on average flat, for both spirals and early-types, independently of the distance and morphology of the closest neighbor, and regardless of the LD. SFR_3 measures the star formation activity more than 1 Gyr ago; with typical cluster crossing times of $\sim$ 1 Gyr, spirals are likely to be at their first passage within the cluster, and the LD might have been changing throughout this period. Even though SFR_2 measures star formation only $\sim$ 0.5 Gyr ago, our time resolution is likely not enough to discern multiple galaxy interactions, each of which may both enhance and quench the SFR during a relatively short time.

Quenching indices $S_{4,3}$ and $S_{3,2}$ do not display any dependence on the closest neighbor, neither for spirals nor for early types. At high LD, the $S_{2,1}$ index (Figure 5.11, bottom row), however, is three times stronger for early-types with an early-type closest neighbor within one virial radius of the companion, than if the neighbor is a spiral. At low LD, there are no differences in $S_{2,1}$ for early-type target galaxies, within the

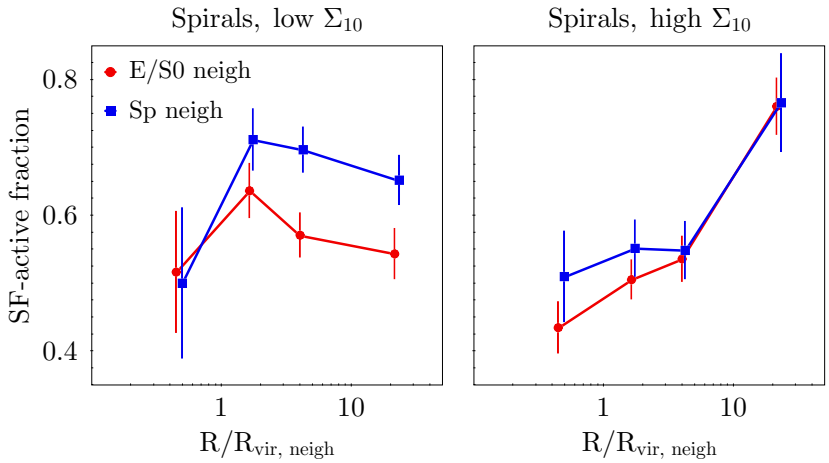

Figure 5.12: Fractions of SF spiral galaxies as a function of distance to the closest neighbor, separated in two bins of LD, as in Figure 5.11. Colors as in Figure 5.8. Error bars represent binomial errors.

error bars. Conversely, for spirals at low LD, quenching is up to 1 dex higher if the closest neighbor is an early type, than when it is another spiral. When the companion galaxy is farther away than four virial radii, the quenching index is almost flat, with an average value identical to that of spirals at high LD, regardless of neighbor type. That $S_{2,1}$ is on average flat at high LD values may be because interactions can both favor and suppress star formation.

We also analyze the fractions of SF spirals in the two bins of LD (most early-type galaxies are quenched, as seen in the left panel of Figure 5.10). The result is shown in Figure 5.12. SF fraction is lowest when target spirals are located within one virial radius of the closest neighbor, regardless of its morphology and the LD. At high LD, the SF fraction grows with companion distance, independently of neighbor morphology. This suggests that, in this regime, any effect induced by the presence of a close neighbor is convolved with those produced by other mechanisms. Additional discussion on this topic is given in Chapter 8, where we aim to synthesize our results.

5.6 SFH AND CLUSTER MASS

In the previous sections, we analyzed the influence of local environmental properties on the stellar content of galaxies. Here, we repeat this analysis, but now taking into account the cluster environment as a whole. We analyze possible effects of cluster mass, parameterized by cluster galaxy velocity dispersion (σ_{cl}) and by cluster X-ray luminosity (L_X), on the SFHs and the quenching of galaxies. Of course, large-scale and local properties of the environment are not clearly separated: massive clusters (large-scale property) will be, in general, richer, both in ICM and in galaxies (local

properties). The next step will be to analyze if and which aspects of the stellar populations are affected. Just like for the morphology, we know that a dense environment strongly affects the star formation process; in what follows, we try to "globally" quantify how.

In subsection 4.7.2, we concluded that cluster mass has a minimum effect on the fractions of SF galaxies. Hereafter, we investigate whether the large-scale environment affects the ability of a galaxy to form stars not only in the present but also in earlier cosmic epochs. Once again, we limit the analysis to spirals because these galaxies have most likely spent the shortest amount of time in the cluster, and since star formation dominates in this morphological class. We first calculate the average SFH of SpE and SpL galaxies, separated in three ranges of cluster σ_{cl} and L_X, and find no significant differences as a function of these cluster mass proxies. Even when we divide the spiral sample into low and high mass bins (threshold at $\log_{10} \mathcal{M}_*/M_\odot = 10.2$), there is no evidence that more massive clusters influence the SFH more effectively.

Quenching and cluster mass

Possible differences in the quenching induced by the environment as a whole can be amplified by using quenching indices. In this instance, we have selected clusters with both WINGS and OmegaWINGS data, with a minimum weighted number of 30 spirals (or approximately more than 20 spirals). We thus are left with a total of 28 clusters, for whose spiral galaxies we calculate the error-weighted mean $S_{3,2}$ and $S_{2,1}$, in bins of σ_{cl} and L_X; we also estimate the uncertainties by bootstrapping.

The results are shown in Figure 5.13. In the top panels, we present the relation between $S_{3,2}$ and the two cluster mass proxies. We do see that $S_{3,2}$ grows with increasing cluster velocity dispersion; a flat trend with X-ray luminosity is also observed. If we compare these relations with the average value found for galaxies in the field (dashed blue lines in Figure 5.13), we conclude that, in the cluster halo mass range probed by our sample, the environment boosts the quenching by a factor ranging from 1.36 to 1.73, for low- and high-mass clusters (gauged by σ_{cl}), respectively. This cannot be due to differences in the galaxy stellar mass (i. e., mass quenching), given that the mass distribution of spirals is very similar in clusters and the field (see Figure 4.2, bottom left panel).

On the other hand, a flat trend is observed for $S_{2,1}$ versus L_X, with values very close to those encountered in the field. A different result is found when considering $S_{2,1}$ as a function of growing σ_{cl}: in this case, the average index decreases, from marginally above to marginally below the value for the field galaxies. This result seems to contradict the evidence showing that a number of physical mechanisms halt, or at least hamper, star formation processes in clusters, leading to significant differences concerning field galaxies.

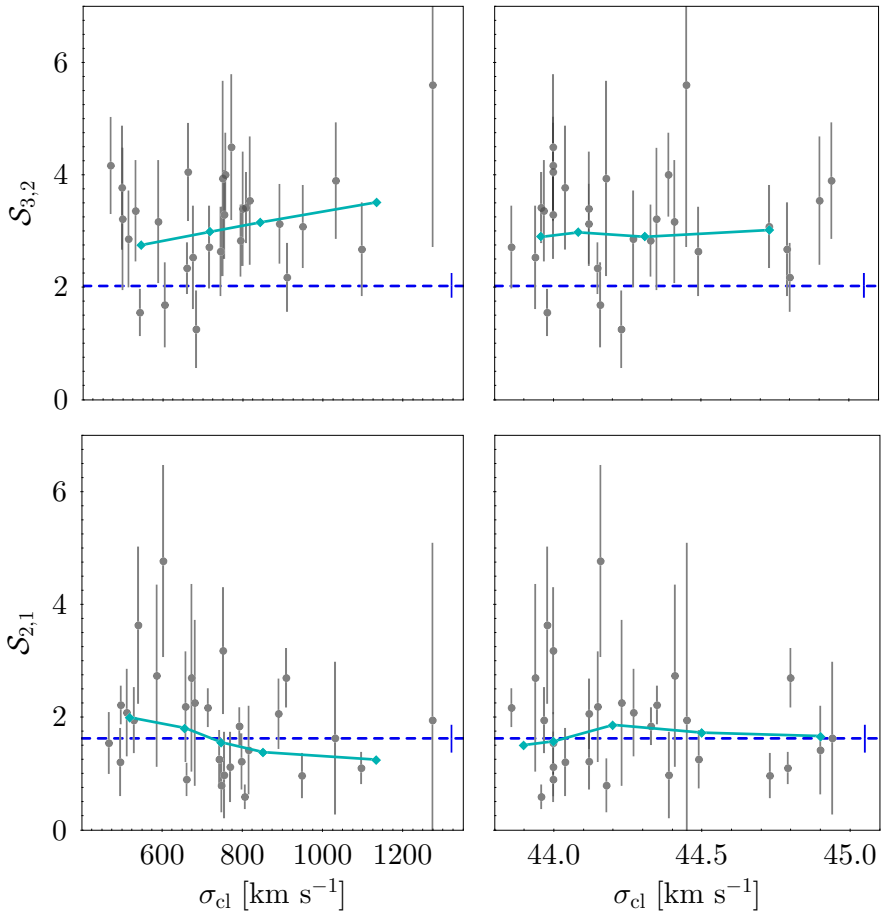

Figure 5.13: Average quenching indices $S_{3,2}$ (*top row*) and $S_{2,1}$ (*bottom row*), for spiral galaxies in a sample of clusters (each gray point is a cluster, see text), as a function of cluster velocity dispersion (*left-hand panels*) and X-ray luminosity (*right-hand panels*). *Solid cyan lines:* index weighted mean; *dashed blue line:* index weighted mean for the field spiral sample. Error bars are calculated through bootstrapping.

Various interpretations can be offered to explain this result. One is stochasticity, due to the fact that the recent SFR is characterized by the presence of nebular emission lines that are representative of a very small range of stellar ages ($\sim 10^7$ yr), and whose intensities are also very sensitive to stellar age within this very range. Having kept the SFR of stellar populations with emission lines constant in the last 20 Myr (see Section 3.1), we cannot detect SFR variations within such a short period. For example, a low SFR at age 4 Myr is somewhat equivalent to a higher SFR at slightly older ages. At older epochs, our observations sample and average SF processes over much longer timescales. The loss of time resolution in the star formation process is amplified by the fact that we only observe the central regions of all galaxies, while star formation is actually patchy and spatially discontinuous.

Secondly, not all interaction processes happening in clusters will lead directly to quenching. RP, for example, besides eventually causing star formation to stop through gas removal via hydrodynamical interactions, can be responsible for inducing moderate bursts of star formation at the beginning of the interaction, as observed in, e. g., Poggianti et al. (2016), Vulcani et al. (2018). This effect is also seen in simulations [e. g., Fujita & Nagashima (1999), Roediger & Hensler (2005)], according to which the intensity of the burst depends on several factors: the relative velocity between the galaxy and the intracluster gas, the gas density, the galaxy inclination relative to its velocity vector. The combination of all these elements may result in the absence of a clear sign of decline in the most recent SFR of cluster spirals.

Last but not least, RP is not the only mechanism that can enhance star formation: as proposed by Park & Hwang (2009), Hwang et al. (2018), and as we have also seen in Section 5.5, galaxy evolution can be affected by interactions with neighbor galaxies, which can both quench and enhance the SFR, depending on the morphology of the neighbor. Early types are quenching agents because they are usually surrounded by a halo of very hot gas, which can both prevent gas cooling and promote gas evaporation, eventually shutting down star formation in a previously SF neighbor. On the other hand, a late type can share its cold gas with a neighbor, thus enhancing the SF activity of the latter.

6

OTHER MECHANISMS AFFECTING STELLAR PROPERTIES

In this chapter, we present the results of other works that have been published or are in preparation, to which this thesis has contributed. In Section 6.1, we use the GASP sample to study stellar evolution, through the effects of RP, of the so-called jellyfish galaxies. RP is an external mechanism that we have already referenced in the last chapter. Here, we find evidence of its impact on galaxies. In Section 6.2, we use observations of disk galaxies in the OmegaWINGS clusters to determine the fraction of barred galaxies, and how the presence of a bar affects the stellar properties. Finally, Section 6.3 analyzes a sample of three post- (major) merger clusters and compares it to eight relaxed clusters. All the clusters belong to the WINGS/OmegaWINGS survey. Although the cluster samples used in this section are small, we obtain clues about how the cluster dynamical state affects galaxy stellar properties.

6.1 THE ROLE OF RAM PRESSURE

Ram-pressure stripping (RPS) is perhaps the most efficient hydrodynamical mechanism to remove the gas reservoir of galaxies, while the dynamics of their stars are left completely unaffected. It happens when galaxies fall into a cluster and cross through the hot intracluster gas. This interaction can sweep the cold gas of the galaxy, star formation gets quenched, and galaxies eventually become passive. According to Gunn & Gott (1972), the classical criterion to have RP is given by:

$$P_{ram} = \rho v^2; \tag{6.1}$$

its efficiency depends on the density (ρ) of the ICM and the infalling velocity (v) of the galaxy with respect to the cluster. RP commonly occurs for galaxies moving at $v \sim 1000$ km s^{-1} in a dense ($n \sim 10^{-3} - 10^{-4}$ cm^{-3}) and hot ($T \sim 10^7 - 10^8$ K) ICM. The efficiency also depends on the gas surface density of the disk and its inclination with respect to the trajectory: RP is more effective for face-on than for edge-on [Vollmer et al. (2001), Roediger & Bruggen (2007)] or highly inclined interactions [Jachym et al. (2009)]. RP is also more effective in low-mass systems since the potential well is shallower, so dwarf and irregular galaxies are expected to be more stripped of their gas than giant spirals [Mori & Burkert (2000)].

In this section, we refer to the analysis undertaken by Fritz et al. (in prep.). Here, we study to what degree RP can affect the recent SFH of cluster galaxies. This is done by identifying galaxies in the same WINGS and OmegaWINGS data exploited throughout this thesis, for which RP effects are clearly established by means of integral field spectroscopy data from the survey GASP. Spatially resolved data, which by default include data of the whole disk of galaxies, will also help us to further strengthen the interpretation of results we have given in Chapter 5, where we identify the role of RP on the different trends we observe.

RP is the physical mechanism responsible for the formation of a peculiar morphological class of galaxies, whose study has been exponentially growing in the last two decades. Dubbed as "jellyfish" galaxies by Smith et al. (2010) because of the presence of long tails of ionized gas unilaterally departing from the galaxy disk, these galaxies are mainly (but not only) found in galaxy clusters, both at low [e. g., Merluzzi et al. (2013), Fumagalli et al. (2014), Poggianti et al. (2017)] and high redshift [e. g., Ebeling et al. (2014), Moretti et al. (2022)]. These galaxies also present filaments and knots, in the process of being stripped from the galaxy. In Figure 6.1, we show the images of two jellyfish galaxies from to the GASP sample: JW100 [studied by Poggianti et al. (2019), Moretti et al. (2020)], located in the cluster A2626, and JO204 [analyzed by Gullieuszik et al. (2017)], in A957.

Figure 6.1: Two examples of jellyfish galaxies: JW100 (*left*) and JO204 (*right*). Tails of gas and stars resembling tentacles extending beyond the bright disk of the galaxies are observed. Images captured by the Wide Field Camera 3 (WFC3) onboard the NASA/ESA HST, at ultraviolet and visible light. Credits: ESA/Hubble & NASA, M. Gullieuszik, and the GASP team.

The study of jellyfish galaxies should not be limited to their main bodies but, rather, include their outer regions, where the "tentacles" are found. Even though morphologies and characteristics such as the one described above can only be produced by RP, their absence does not imply that there is no RP at play at the moment of the observation. Hence, instead of calling them "jellyfish galaxies", which refers only to a particular phase of this phenomenon –the peak stripping–, we will refer to them as "RP affected".

6.1.1 *The GASP sample*

The GAs Stripping Phenomena in galaxies with MUSE (GASP) sample of RP-affected galaxies was selected from the parent catalogs WINGS/OmegaWINGS (described in Section 2.1) and PM2GC [Calvi2011 et al. (2011)], in the redshift range $0.03 < z < 0.07$. The original sample consists of 114 late-type galaxies, 94 as primary objects, and 20 as control sample. The 94 primary galaxies were selected from the atlas of Poggianti et al. (2016), through a visual inspection of *B*-band images in the mentioned surveys. The selected objects display tails, debris tails, asymmetric or disrupted morphologies, and/or one-sided star formation regions or knots. These are clear signs of RPS, and hence galaxies that exhibit them were considered as candidate RP-affected galaxies. The range of their stellar masses is $\sim 10^9 - 10^{11.5}$ $M_\odot$; they are mostly SF, with SFRs a factor of two larger than non-candidate galaxies in the same stellar mass range, on average. The control sample includes 12 galaxies in clusters and 8 in the field that do not show optical signs of stripping.

Spectroscopic observations were carried out using the Multi Unit Spectroscopic Explorer (MUSE) spectrograph at the Very Large Telescope (VLT), UT4. The spectral range is $\lambda = 4,800 - 9,300$ Å, with a resolution FWHM ~ 2.6 Å and a plate scale of 1.25 Å pixel^{-1}. We refer to Poggianti et al. (2017) for more details on the data acquisition, reduction, and analysis of the GASP sample.

For the rest of this section, when we refer to the GASP sample, we mean only the 34 galaxies that are common to WINGS+OmegaWINGS. These galaxies have been confirmed to be RP stripped. We compare these 34 galaxies with all the remaining spirals in WINGS+OmegaWINGS. As we have already explained above, GASP data here are merely used to identify galaxies affected by RP, while the analysis is performed, for the sake of consistency with the other parts of this thesis, on fiber spectra. This will also provide the opportunity to check if and how fiber spectra can actually detect changes induced by RP on the SFH, hence further supporting the findings so far reported.

6.1.2 *The main sequence*

We first examine the effects of RP on the current SFR by comparing the GASP sample to the WINGS+OmegaWINGS datasets. To begin with, we look at the 34 RP-affected galaxies in GASP for which we have obtained stellar properties with the SINOPSIS code (see Chapter 3).

In Figure 6.2 (left panel), we show the sSFR (i. e., $SFR_1/\mathcal{M}_*$), as a function of stellar mass, for both actively SF spirals in WINGS/OmegaWINGS and the 34 RP-affected galaxies in GASP. Mean sSFR values of stellar mass bins are plotted with large squares; they were obtained through the bootstrap resampling method (see Appendix C). Although this result is derived only with the stellar populations sampled within the fibers (i.e., at the centers of galaxies), RP-affected galaxies present a MS clearly above the average relation for SF spiral galaxies. Besides, the enhancement of SFR seems to be independent of the stellar mass (although the statistics are poor for the RP-affected galaxies at the high end of the stellar mass distribution). We can better appreciate this increase through the distribution of differences between the sSFR of each galaxy and the mean value in its corresponding stellar mass bin, as shown in Figure 6.2 (right panel). The RP-affected galaxy sample is above the general cluster sample.

This result is in agreement with Poggianti et al. (2016), who performed a similar analysis using the same data, and confirms that even fiber spectroscopy is able to detect this effect, at least for part of the WINGS/OmegaWINGS–GASP sample. Such

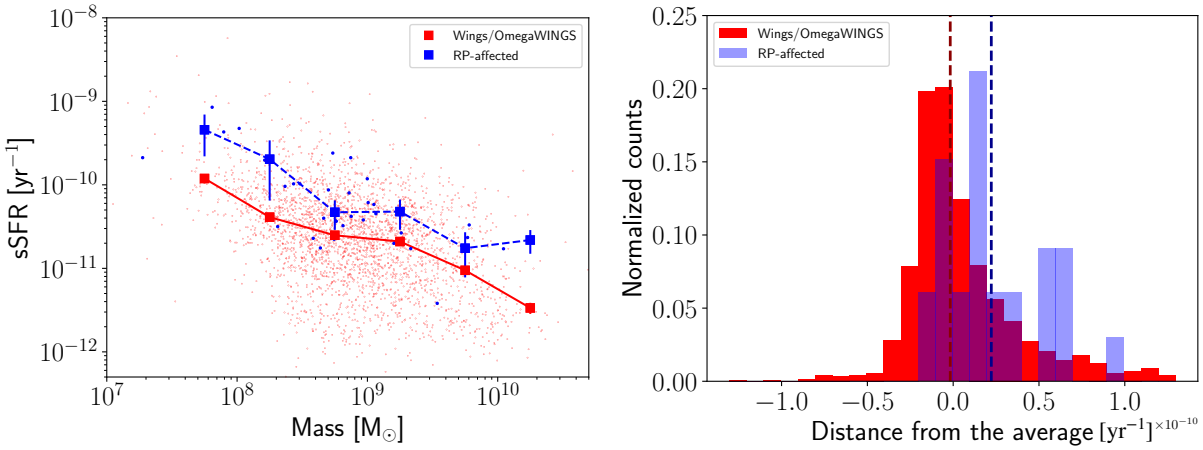

Figure 6.2: *Left:* sSFR as a function of stellar mass. *Blue dots:* RP-affected galaxies in GASP; *red dots:* SF spirals in the WINGS/OmegaWINGS dataset. *Large squares:* mean sSFRs of both samples, calculated with the bootstrap method. *Right:* Distribution of differences between the sSFR of each galaxy and the average in its stellar mass bin. *Vertical dashed lines:* median values of each sample. Colors as in the left panel. Plots taken from Fritz et al. (in prep.).

trends were also corroborated by Vulcani et al. (2018) with integral field unit (IFU) data, hence sampling the whole disk of the galaxies. They compared the SFR-mass relation of RP-affected galaxies with the MS of a control sample. We note that the *bona fide* RP-affected galaxies displayed in Figure 6.2 are most likely not the only ones suffering RP in the GASP sample. Some of the galaxies above the average relation might not have been detected as possible RP-affected candidates by visual inspection.

Using WINGS+OmegaWINGS data, Vulcani et al. (2022) found that, at any given time, approximately 35% of blue, late type, non-interacting, cluster galaxies show in optical bands signals of stripping in their morphology. They infer that almost all cluster galaxies experiment a stripping phase during their lifetime. This means that other galaxies may be suffering RP phenomena but are not detected as RP-affected because no IFU data are available. If more galaxies were observed with IFUs, sampling external regions as well, the differences between "normal" galaxies and those affected by RP would probably be stronger. Hence, these differences in sSFR may be a lower limit to the real effect.

6.1.3 *The SFH of RP-affected galaxies*

One of the most clear-cut effects of RPS is the partial or even complete removal of the ISM of a galaxy, eventually resulting in the creation of tails of neutral and ionized gas. This happens as an infalling galaxy travels through the ICM, and affects most galaxies that are located within a half virial radius of the cluster center [Zinger et al. (2018)]. Nevertheless, the first effect a galaxy would experience is a compression of its ISM, which will eventually lead to a burst of star formation [Lee et al. (2022)]. Hence, a galaxy displaying long ionized gas tails has already gone through this phase several millions of years ago and, before that, has begun to experience this gas compression.

Since the RP-affected galaxies in our sample were selected visually to exhibit tails, star formation knots, or asymmetries, they must have spent already enough time within the cluster to develop these characteristics through the interaction with the ICM. Hence, RP may have enhanced the SFR at ages older than the recent 20 Myr used to derive the sSFR plotted in Figure 6.2, and its effects may have been possible even stronger than the ones observed in the current SFR.

To examine this hypothesis, we compare the SFHs of the RP-affected galaxies with those of all the cluster spirals in WINGS+OmegaWINGS, again using the fiber spectra results from SINOPSIS. We compare the four SFRs as a function of present-day stellar mass for the RP-affected and spiral samples. The result is presented in Figure 6.3. Mean SFRs in six stellar mass bins are indicated with large squares, while error bars are obtained with the bootstrapping method. We see that both samples present a similar "MS" in the third and fourth age bins, as expected. At the oldest ages, spiral galaxies have not been yet affected by mechanisms due to the environment, like RPS. In

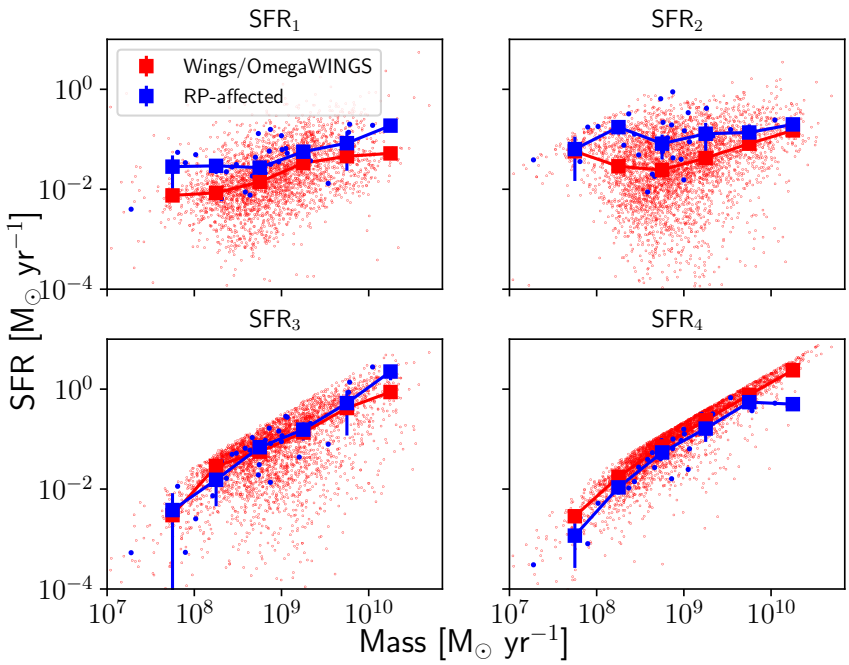

Figure 6.3: SFR in four age bins, as a function of stellar mass, for RP-affected galaxies (*blue squares*) and the spiral sample in WINGS/OmegaWINGS (*red squares*). The SFRs were calculated using the bootstrap method in bins of stellar mass. Plots taken from Fritz et al. (in prep.).

the two youngest age bins ($0-20$ Myr and $20-570$ Myr; see Table 3.1), the SFR-mass relation for RP-affected galaxies is well above the one for "normal" spirals; the offset is greater for SFR_2 than for SFR_1 by a factor of four, on average, and even larger for low-mass galaxies. This is even more easily detected if we plot the distribution of differences between the SFR of each galaxy and the mean value of its stellar mass bin, for both the RP-affected and the WINGS/OmegaWINGS spiral sample (Figure 6.4).

Vulcani et al. (2018) performed an analysis of the SFR-mass relation using MUSE data for 42 RP-affected galaxies in the GASP sample, with 32 isolated spiral galaxies as the control sample. The advantage of that work is that they use IFU spectra (sampling the whole galaxies), unlike our spectra dataset, which only covers the central part of galaxies (i. e., $2-3$ kpc). On the other hand, the advantage of our study is that we have a much larger control sample (around 1,400 spiral galaxies). Furthermore, here we consider the SFHs at older epochs as well, and hence we examine the effects of RPS, not only on the present-day SFR, but at the outset of the hydrodynamic interactions between galaxies and the ICM. As is clear from both our analysis (Figure 6.3) and the one performed on spatially resolved data [see Fig. 1 in Vulcani et al. (2018)], while RPS-affected galaxies do display an enhancement of star formation, if this is quantified only employing the ionized gas intensity, the effects of RP may be substantially

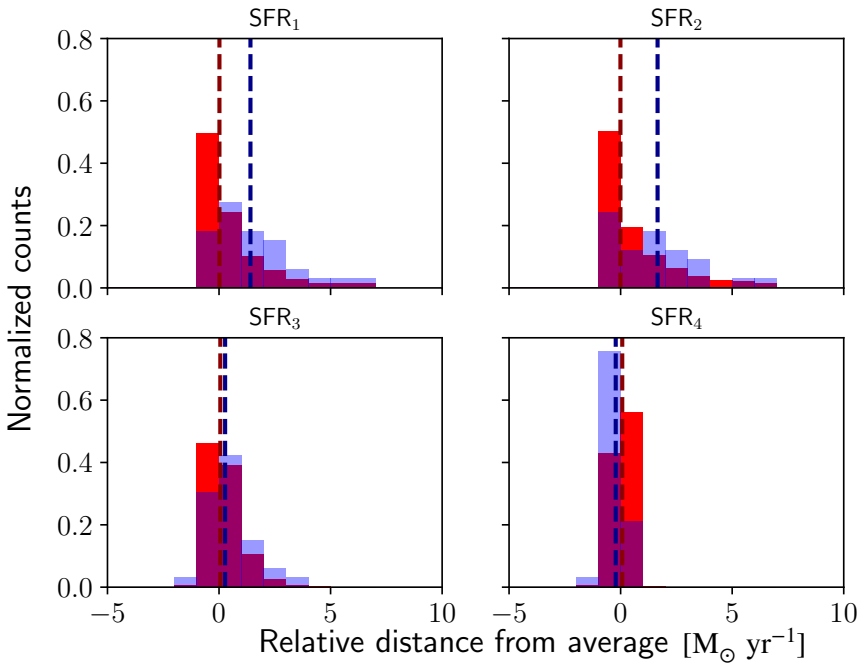

Figure 6.4: Distribution of differences between the SFR of each galaxy and the mean of its mass bin (see Figure 6.3). Colors and vertical lines as in Figure 6.2. Plots taken from Fritz et al. (in prep.).

underestimated. In fact, galaxies that display the most striking gas tails may be past the phase characterized by the strongest star formation enhancement and on their way to quenching, after having lost a substantial fraction of their gas. Indeed, both our analysis and the one based on spatially resolved data suggest that the peak of star formation has happened already between ~ 20 and ~ 570 Myr ago, and would be completely lost if only emission lines were taken into account.

6.2 INVESTIGATING THE EFFECT OF STELLAR BARS

The spectral analysis of the OmegaWINGS cluster galaxies allowed a further contribution: the study of galaxies with morphologies later than S0 and hosting a stellar bar. This work was published in Tawfeek et al. (2022). Its most important goals were the analysis of the correlation between the cluster environment and the presence/absence of stellar bars, and to study the effects of the stellar bar on the stellar populations.

Stellar bars are elongated structures that cross the galaxy center. Depending on the classification method, in the local universe, bars are found in ~ 30% of disk galaxies in the optical [Sellwood & Wilkinson (1993), Lee et al. (2019)], and ~ 65% in the IR [Eskridge et al. (2000)]. The fraction increases with galaxy stellar mass and is lower

for galaxies with large gas content and bluer colors [Cervantes Sodi (2017)]. Bars are slightly more frequently observed in the field (~ 30%) than in clusters (~ 30%) [see Tawfeek et al. (2022), for local clusters, and Barazza et al. (2009), for intermediate redshifts ($z \sim 0.6$)], and tidal interactions between galaxies can influence the formation of bars [Noguchi (1987), Athanassoula & Bureau (1999)].

Different models are used to explain the formation of bars. In isolated galaxies, the orbits of stars can become unstable and lose their circular path. Elongations in orbits grow, and orbital resonances related to global instabilities shape a stellar bar [Athanassoula (2013)]. The merger model can also explain, through simulations, bar formation [Di Matteo et al. (2010)], and minor mergers (mass ratio ~ 0.1) are more conducive to the formation of bars [Cavanagh & Bekki (2020)]. Stellar bars can be destroyed by the action of central mass concentrations, such as supermassive black holes [Sellwood & Wilkinson (2004), Athanassoula et al. (2005)]. This means that disk galaxies that are currently observed as non-barred may have been barred in the past [Kormendy & Kennicutt (2004)]. Minor mergers can weaken or destroy bars, due to the accumulation of stars from satellites towards the galaxy center, which may cause an increase in both the central mass and the specific angular momentum [Ghosh et al. (2021)].

Stellar bars are believed to have a strong influence on the formation of bulges: they can redistribute the gas content and angular momentum between the components of galaxies [Weinberg (1985)], and can trigger star formation in the inner regions; these effects are stronger in galaxies with stronger bars [Wang et al. (2012)]. Another side of the coin is that bars can also deplete the infalling gas and quench star formation quickly [Bournaud & Combes (2002)]. This may explain the fact that strong bars decrease with increasing HI gas content [Cervantes Sodi (2017)]. Similarly, Kim et al. (2017) find that star formation is lower in strongly barred galaxies than in non-barred ones. They also report that there are no significant differences between the stellar populations in both kinds of galaxies, thus the influence of a bar on the star formation may be a local effect.

Stellar bar hosts in clusters can provide very useful clues about the combined effects of internal mechanisms (the stellar bar) and external ones (RPS), on both nuclear activity and star formation. Recently, Sánchez-García et al. (2023) presented results on the combined effects of these two mechanisms on infalling galaxies, with an analysis based on GASP data. Galaxies showing the most extreme cases of enhanced central star formation activity are found among barred galaxies in extreme RP conditions, such as jellyfish galaxies.

Given this picture, it is easily understood how stellar bars constitute another parameter that should be taken into account when discussing galaxy evolution. Here, we present a global study of the effect of bars on the stellar populations for only OmegaWINGS cluster disk galaxies.

6.2.1 *Sample selection and bar identification*

The galaxy sample used here is based on the V-band images of 32 OmegaWINGS clusters with spectroscopic observations. The sample is restricted to galaxies with morphological types $T_M > -5$ (to exclude most ellipticals; see subsection 2.1.5), ellipticities $\epsilon < 0.5$, and surface brightnesses larger than 21.5 mag arcsec^{-2} in the V-band, where isophotes are difficult to fit in the outer galaxy regions. The sample contains 3,456 galaxies that fulfill these criteria, to which the bar identification procedure described below was applied.

There are several methods to detect bars, such as visual inspection, isophotal analysis, ellipticity profiles, multicomponent decomposition, and kinematic maps of both stellar orbits and molecular gas, among others. Some methods may not be efficient to use with large databases. It is known from observations that bars affect the surface brightness of host galaxies: they produce isophotes with an approximately constant (within $\pm 20°$) position angle (PA), and an ellipticity that first increases monotonically with galactocentric distance and then drops sharply where the bar ends. In this work, we have developed a tool to automatically classify barred galaxies; it uses the task `photutils.isophote` in Python and fits iteratively elliptical isophotes to the galaxy image. Similarly to other works, a galaxy is identified as barred if the maximum and minimum values of the ellipticity differ by $\Delta\epsilon \geqslant 0.1$, while the PA varies by $< 20°$ [e. g., Lee et al. (2019), Yoon et al. (2019)]. This technique can be applied to large databases and was validated by visual inspection. Details of the method can be found in Tawfeek et al. (2022). 906 galaxies in the sample (26%) were identified as barred. This result is in agreement with the barred fractions obtained by Barazza et al. (2009) (24%) and Yoon et al. (2019) (27%), who used a similar methodology.

6.2.2 *Bar fractions and galaxy properties*

The $(B-V)$ (rest frame) color is a broad proxy for the stellar population properties of galaxies. Hence, as a first step, we analyze a possible dependence of the barred galaxy fraction on their (total) color, using the absolute magnitudes obtained in Section 4.4. Interestingly, we find (Figure 6.5, left panel) that the fraction of barred galaxies is higher in bluer galaxies. This is in agreement with some works [e. g., Barazza et al. (2008), Aguerri et al. (2009)], but conflicts with other studies [e. g., Masters et al. (2010), Lee et al. (2012)], which find a higher bar fraction in redder galaxies. This apparent inconsistency may be because we use cluster galaxies, and the cluster environment produces transformations in both the stellar populations and the morphology.

The fraction of galaxies hosting a bar is known to be a function of stellar mass [Cervantes Sodi (2013)]. Hence, we now check if this is also valid for galaxies in the OmegaWINGS sample. The results are presented in Figure 6.5, right panel. We obtain

a very good agreement with what is expected from similar studies: an increasing barred galaxy fraction with stellar mass, starting from 21% for the least massive galaxies (the lower limit of the sample we defined in this thesis) to ~ 41% for the most massive ones. This result is comparable to the one in Yoon et al. (2019), who used SDSS data and a similar method for the bar detection.

We now plot the fraction of barred galaxies as a function of morphology (see subsection 2.1.5 for the nomenclature of types), as shown in Figure 6.6. We observe a clear trend of increasing bar fraction from early types (S0s; ~ 20%) to later types (late spirals; ~ 56%). This dependence is what we expect, as bars need a dynamically cold disk to form and grow [Sheth et al. (2012), Yoon et al. (2019)]. The higher fraction of bars in later types explains the finding that bluer galaxies are more likely to be barred.

According to some works, the cluster environment can enhance/suppress the stellar bar formation. A good way to check this point is to look for the fraction of barred galaxies as a function of cluster global properties, taking X-ray luminosity as a proxy for the cluster mass. The result obtained is a slightly decreasing trend in the bar fraction, from ~ 28% in less luminous clusters to ~ 20% in those more luminous. While these results might seem to indicate that the cluster environment as a whole does influence the life of stellar bars, this trend can be easily explained as a secondary effect of two relations: the one between morphology and bar, and the one between morphology and cluster mass. As already shown in Figure 6.6, the probability for a galaxy to host a stellar bar is a function of the morphological type.

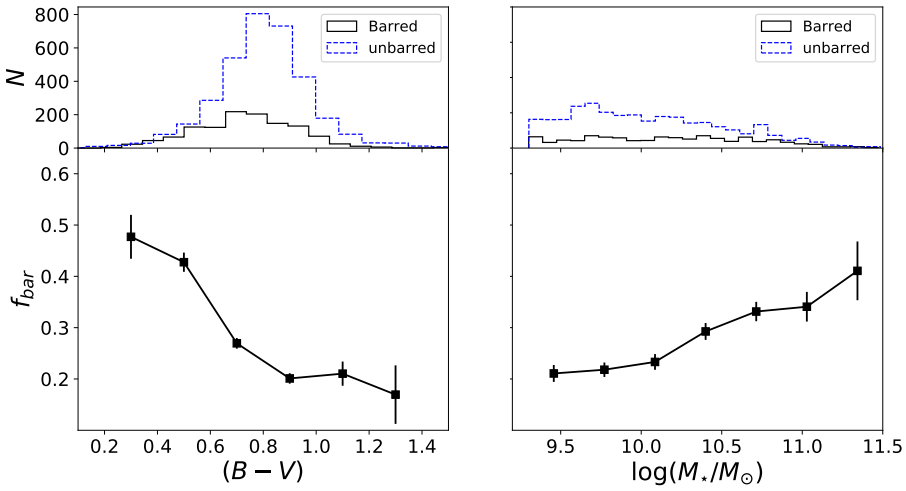

Figure 6.5: Fractions of barred galaxies as a function of total color (*left*) and stellar mass (*right*). Error bars are obtained through bootstrapping. The distributions of barred (*black solid line*) and non-barred (*blue dotted line*) galaxies are shown in the top panels. Plots taken from Tawfeek et al. (2022).

On the other hand, both Poggianti et al. (2009) and this thesis (see Figure 2.5, right panel) have demonstrated that there is a slight tendency for more massive clusters to host proportionally fewer spiral (or, more in general, late-type) galaxies. According to this scenario, the barred galaxy fraction in clusters is mainly driven by (or is a secondary effect of) the morphology–density relation (see Figure 4.1).

6.2.3 *Quenching indices and stellar bars*

The role of bars in the star formation activity is not clear. Some studies find that bars can enhance the SFR [e. g., Hawarden et al. (1996), Lin et al. (2020)], while others state otherwise [e. g., Chapelon et al. (1999), George & Subramanian (2021)]. Sánchez et al. (2014), using data from the Calar Alto Legacy Integral Field Area [CALIFA; Sánchez et al. (2012)] survey, found no differences in the stellar metallicity and age gradients of spirals with and without bars. The discrepant findings between diverse works may be due to the choice of galaxy samples. Properties such as morphology, redshift, stellar mass, and LD environment should match, to ensure the best possible control over the properties of the samples [Vera et al. (2016)].

As we have mentioned, a quite intuitive and effective way to quantify the SFHs of galaxies is by means of the quenching indices (defined in Equation 5.1). Here, we analyze quenching indices as a function of stellar mass for barred and non-barred galaxies, as shown in Figure 6.7.

The $S_{4,3}$ index (top panel) is, on average, very similar for barred and non-barred galaxies. At these early epochs, stellar bars probably have not been yet formed. There

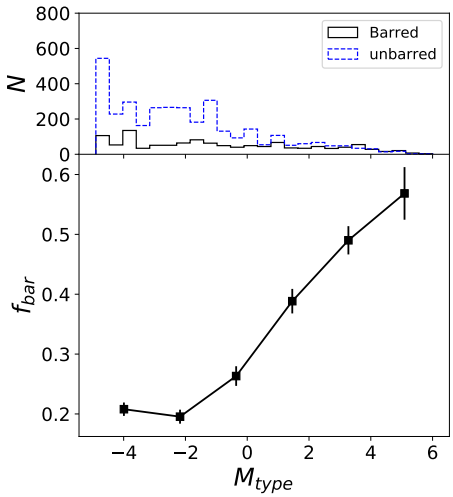

Figure 6.6: Fractions of barred galaxies as a function of morphological type. Error bars and top distributions as in Figure 6.5. Plot taken from Tawfeek et al. (2022).

is a small difference in the most massive bin, where non-barred galaxies present a slightly higher quenching. A possible explanation for this is that bars can redistribute the gas content, slightly increasing the SFR.

As for the $S_{3,2}$ index (Figure 6.7, middle panel), we find a lower quenching for barred galaxies in all mass bins. The difference with non-barred galaxies is largest for

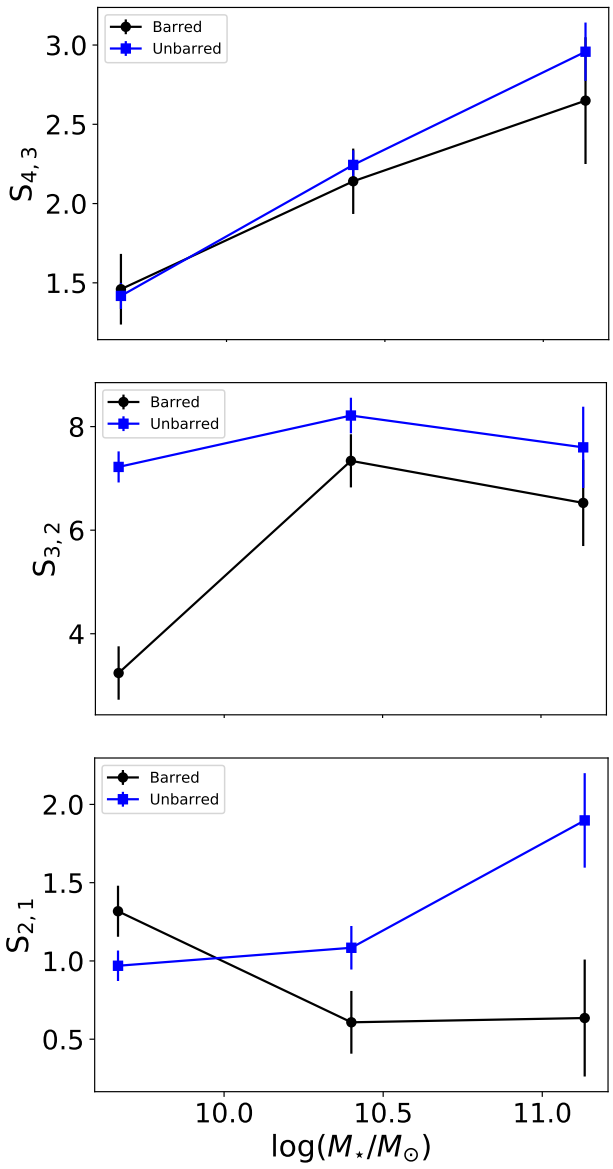

Figure 6.7: Quenching indices of the spiral galaxy sample as a function of stellar mass. *Black lines:* barred galaxies; *blue lines:* non-barred galaxies. Error bars as in Figure 6.5. Plots taken from Tawfeek et al. (2022).

the least massive galaxies: in this mass bin, the quenching index is ~ 3.2 times higher for non-barred than for barred galaxies. For intermediate and high-mass galaxies differences are marginal, but the quenching index values are always higher for those without a bar. The reduced quenching in barred galaxies may be accounted for by the gas transfer from the outer disk to the inner galaxy by the bar. This favors the onset of star formation and the rejuvenation of the galaxies towards their inner regions.

Quenching in recent ages, given by the $S_{2,1}$ index (Figure 6.7, bottom panel), is stronger for non-barred galaxies of intermediate- and high-mass. A star formation enhancement is evident for barred galaxies of these masses. In the case of low-mass galaxies, where the fraction of barred galaxies is lowest, the quenching is inverted, i. e., it is higher for barred galaxies. While all low-mass galaxies are prone to be more affected by external agents, due to their shallower gravitational wells, barred ones can exhaust their gas reservoir more rapidly than their non-barred counterparts, hence causing a stronger quenching.

Finally, we conclude that the probability for a cluster galaxy to host a stellar bar is mainly driven by its morphology; it is higher for more massive, later types, and for those located in the cluster outskirts. Tidally induced bars can be triggered by encounters between galaxies [Łokas (2018)] and by cluster pericenter passages [Smith et al. (2021)]. Stellar bars can also be weakened or even destroyed when the galaxy is perturbed by external agents, and this is likely to happen when a galaxy enters the cluster. Once gravitational interactions are sufficiently strong to cause morphological transformations, the stellar bar may be dissolved. Before that, however, it may help transport gas toward the galaxy center and induce central star formation activity (Kelkar et al., submitted).

6.3 POST-PROCESSING IN MAJOR CLUSTER MERGERS

Throughout this work, we have used a broad definition of cluster and field environments. New studies [e. g., Vulcani et al. (2019), Kuchner et al. (2022)] have demonstrated that galaxies can undergo pre-processing phenomena in intermediate environments, such as those of filaments and walls. Cosmic filaments are large structures in the universe, along the edges of walls bounding giant voids of matter [Colberg et al. (2005)]. They contain most of the mass and galaxies in the universe and are connected through galaxy clusters. Galaxy clusters accrete and increase their mass and galaxy content through them.

Furthermore, clusters can grow through cluster–cluster mergers as well. These violent events can perturb the ICM and the cluster as a whole [Botteon et al. (2018)]. Post-merger clusters may retain possible traces of these episodes, such as a higher fraction of stripped galaxies by RP (Lourenço et al., submitted), and different kinds of environments, unlike relaxed clusters [Shim et al. (2011)]. Major cluster mergers present evidence of both quenched [Pranger et al. (2014)] and enhanced [Stroe et

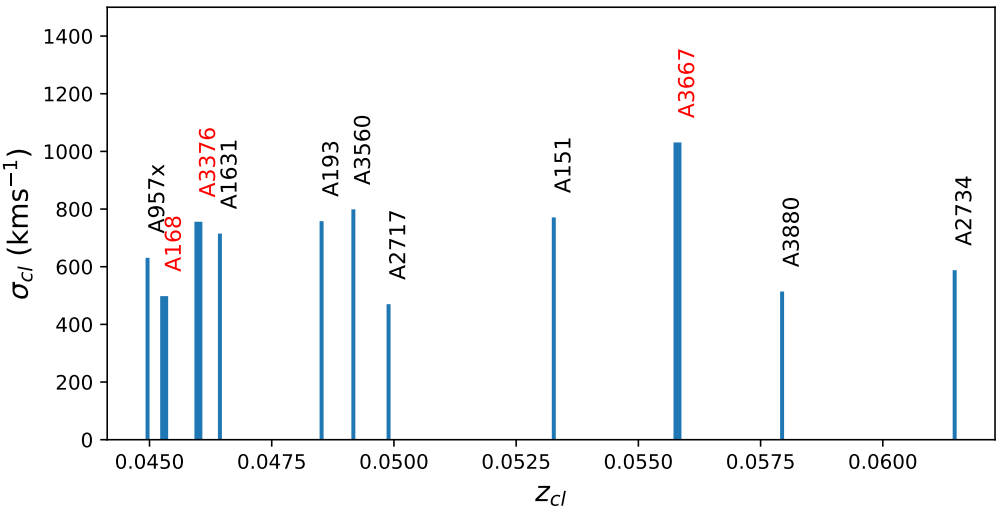

Figure 6.8: Velocity dispersion as a function of redshift. *Thick bars with red names*: post-merger clusters; *narrow bars with black names*: relaxed clusters. Image taken from Kelkar et al. (submitted).

al. (2015)] SFRs, as well as other characteristics not present in relaxed clusters, e. g., the presence of two BCGs, an offset between both the (main) BCG velocity and position in comparison with the overall cluster structure, and a difference between the BCG(s) position and the peak(s) of the X-ray emission [Lopes et al. (2018)]. Thus, the study of stellar population properties in pre- and post-processed galaxies is key to understanding the evolution of cluster mergers [Kelkar et al. (2020)].

This section is based on the work of Kelkar et al. (submitted), to which this thesis has substantially contributed, the study of galaxy properties such as morphology and star formation activity in three post-merger clusters: A3367, A3376, and A168. These clusters belong to the WINGS/OmegaWINGS parent sample (Section 2.1), and were chosen for showing evidence of a relatively recent collision/interaction ($\sim 0.6-1$ Gyr ago). In addition, a control sample of eight dynamically relaxed and non-merging clusters was selected. These are regular, with small substructures: A151, A1631, A193, A2717, A2734, A3560, A3880, and A957. The analysis of the dynamical stages of WINGS/OmegaWINGS clusters was performed by Lourenço et al. (submitted), using X-ray data and optical proxies. The contribution of this thesis to Kelkar et al. (submitted) consisted mainly in providing the stellar population properties of galaxies in the aforementioned clusters, and in assessing the possibilities and limitations of using such properties to study the effects of cluster mergers.

The galaxy sample used from these clusters is the same as the one defined in Section 4.1, except that this time only galaxies located within a clustercentric distance of 0.7 R_{200} were chosen. In Figure 6.8, we show the cluster velocity dispersion as a function of redshift, for both the post-merger and relaxed cluster samples used here.

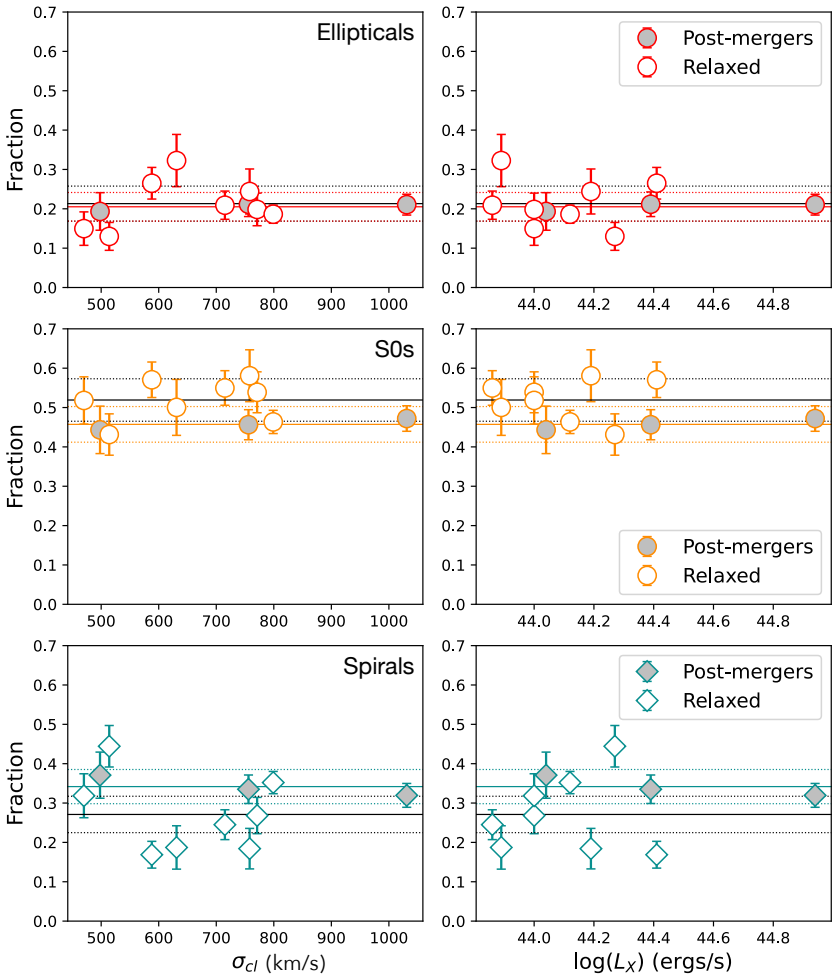

Figure 6.9: Morphological fractions of galaxies, as a function of cluster velocity dispersion (*left*) and X-ray luminosity (*right*), for ellipticals (*top*), S0s (*middle*), and spirals (*bottom*). *Grey symbols:* merging clusters; *white symbols:* relaxed clusters. *Black* and *colored solid lines* indicate mean fractions for post-merger and relaxed clusters, respectively. *Light dotted lines:* 1σ errors in the mean fractions. Image taken from Kelkar et al. (submitted).

6.3.1 *Morphological fractions in merging clusters*

Morphological fractions as a function of cluster mass proxies were studied in Section 2.3 for WINGS/OmegaWINGS clusters. These can provide information about the processes leading to morphological transformations [Poggianti et al. (2009)]. Here, we review these fractions for the post-merger and relaxed cluster samples, as shown in Figure 6.9, again, as a function of σ_{cl} and L_X, but this time for galaxies within 0.7 R_{200}. This is one of the first studies to explore morphological fractions in these extreme environments.

While the fraction of ellipticals in both cluster samples is the same (~ 21%), we note a slight difference in the fractions of S0 and spiral galaxies. The fractions of S0s are, on average, $\sim 52 \pm 5\%$ in relaxed clusters, versus $\sim 46 \pm 4\%$ in post-merger clusters, while for spirals these fractions are $\sim 27 \pm 5\%$ and $\sim 34 \pm 4\%$, respectively. Although this result is obtained with only three post-merger clusters, it suggests that cluster merging hinders the transformation of cluster spirals into S0s, at least in the short timescales probed by these mergers (~ 1 Gyr ago).

6.3.2 *Quenching in merging clusters*

In Section 5.6, we analyzed the $S_{3,2}$ and $S_{2,1}$ quenching indices of a sample of cluster spirals in WINGS/OmegaWINGS as a function of cluster global properties. This time, we repeat the analysis on the relaxed and post-merger cluster samples. On the one hand, the SFR_3 value is calculated over stellar ages between ~ 0.57 and 5.75 Gyr (see Table 3.1). Based on the results obtained in Chapter 5, the SFHs of WINGS/OmegaWINGS galaxies are characterized by a steady decline (see e. g., Figure 5.1), but given the wide age range covered by SFR_3, any possible evolution may not be detectable in this index. On the other hand, the three post-merger clusters used here are estimated to have collided about 1 Gyr ago, which sets a fairly strong upper limit to the dating of possible effects on the stellar populations of their galaxies. 1 Gyr ago is also towards the beginning of the time interval sampled by SFR_3. Hence, it is likely that the $SFR_{3,2}$ and $S_{2,1}$ quenching indices may show traces of the evolution of the stellar populations during the merging process.

In Figure 6.10, we present the $S_{3,2}$ and $S_{2,1}$ indices, as a function of σ_{cl} and L_X, as we have done over the course of this work (see Figure 5.13), for the three post-merger clusters and the eight relaxed clusters. The $S_{3,2}$ indices of post-merger clusters (green squares) are systematically higher than the average trend (cyan line in the figure), even though the dispersion of each cluster value is somewhat large, while relaxed clusters (red triangles) present values scattered around the average relation. Other clusters (gray circles) are not used in this section because they lack a clear dynamical classification[1], show quenching values similar to the already relaxed clusters, while also possibly hinting at the presence of minor dynamical processes still ongoing. On the other hand, the $S_{2,1}$ index, at more recent ages, is similar for all clusters, independently of their dynamical state. There is a possible indication of a slightly higher quenching level in relaxed clusters, even though this effect may be triggered by several different factors, such as RP, neighbor interactions, and local environment, which may be more effective depending on the dynamical status of the cluster.

From this simple and still preliminary analysis, we conclude that cluster–cluster interactions can indeed provide another way to accelerate the turning off of star

1 Lourenço et al. (submitted), find evidence of a small number of substructures/inhomogeneities.

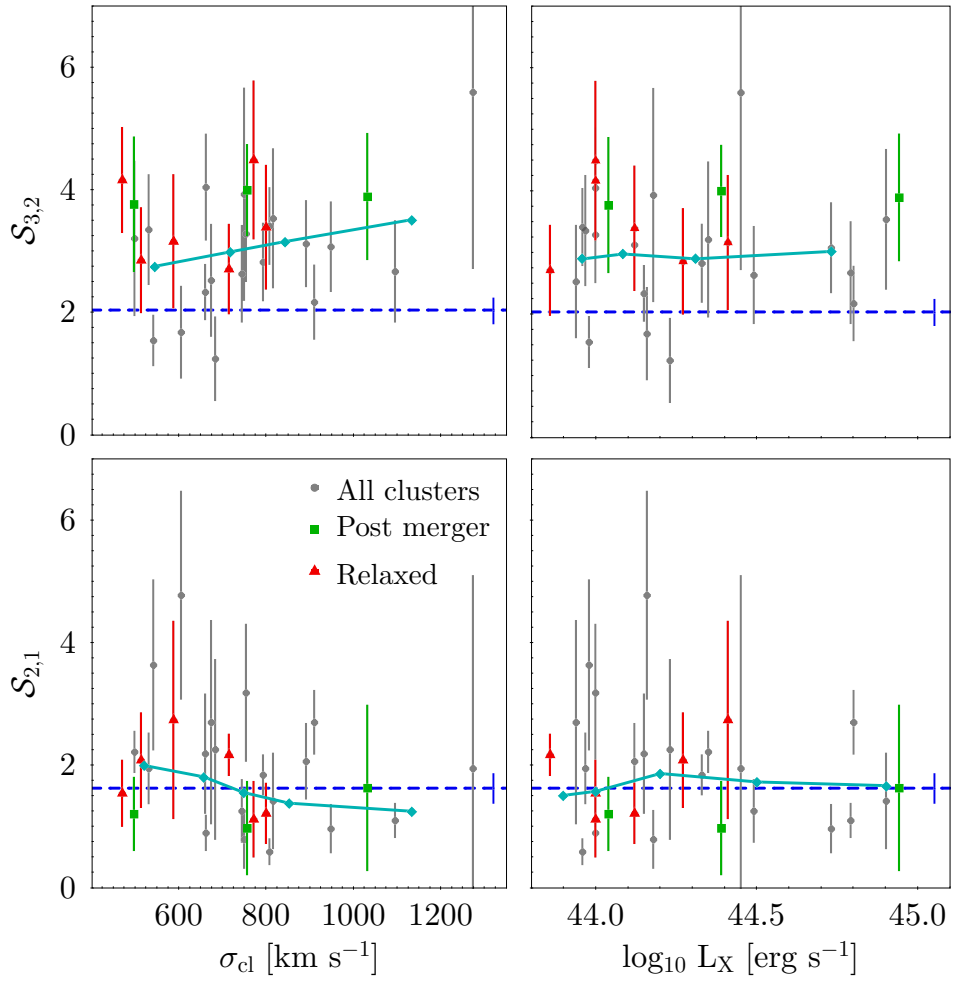

Figure 6.10: Average quenching indices $S_{3,2}$ (*top row*) and $S_{2,1}$ (*bottom row*), for spiral galaxies in the post-merger (*green squares*) and relaxed (*red triangles*) clusters, as a function of cluster velocity dispersion (*left-hand panels*) and X-ray luminosity (*right-hand panels*). *Solid cyan lines:* index weighted mean for all clusters together; *dashed blue line:* index weighted mean for the full field spiral sample. Error bars are calculated through bootstrapping.

formation in their galaxies, even though the details of the responsible mechanisms are far from being established. What is quite clear, instead, is that processes on very large scales, like these, which we have not explicitly taken into account, add a further complication to the kind of analysis we have performed in Chapter 5. They can, in principle, be accountable for weakening or even canceling observed trends.

7

CLUSTER GALAXIES AT HIGH-Z

In this chapter, we investigate stellar properties such as SFRs and SFHs of cluster galaxies, for the first time using the WINGS/OmegaWINGS (low-z) and EDisCS (intermediate-high z). These two surveys include clusters in a very similar mass range and have a galaxy morphological classification. We also use the SINOPSIS code to obtain the stellar population properties of EDisCS galaxies. The results that we present below are unpublished yet, but they constitute another goal for which the WINGS/OmegaWINGS survey was designed, i.e., to provide a dataset that could be used as a reference for subsequent studies at higher redshifts. In the following, we present the EDisCS dataset; their observations, such as imaging and spectroscopy (together with the instruments and the facilities that were used to acquire them); and cluster properties. We then determine the galaxy sample at intermediate-high redshift and compare their main stellar population properties with a newly defined WINGS/OmegaWINGS sample.

7.1 THE EDISCS DATASET

The ESO Distant Cluster Survey (EDisCS) [White et al. (2005)] is a multi-wavelength survey of 20 fields that contain galaxy clusters. The objective of the project is to study cluster and galaxy evolution, the structure of galaxies and clusters, and to characterize the stellar populations, mass, luminosity, and kinematics of galaxies in high-redshift clusters.

The sample of 20 fields was built from the 30 cluster candidates with the highest surface brightness in the Las Campanas Distant Cluster Survey [LCDCS; Gonzalez et al. (2001)]. These 20 fields were confirmed as cluster candidates, and classified into 10 clusters with $0.5 < z < 0.8$ [intermediate-z; Desai et al. (2007)], and 10 clusters at $0.8 < z < 1.2$ [high-z; Postman et al. (2005)]. For these 20 fields, optical data were obtained with FORS2 at the VLT, covering a $6.5' \times 6.5'$ region for each cluster. Images through the B, V, I bands were taken for the 10 intermediate-z clusters, and V, R, I frames were acquired for the 10 high-z ones. As an example, we show in Figure 7.1 two clusters (cl 1354-1230 and cl 1216-1201) from the EDisCS sample. Near-IR photometry in the J and K bands was taken for most clusters, using SOFI at the New Technology Telescope (NTT).

Figure 7.1: Composite *VRI* images of the clusters cl1354 (*left*; $z = 0.762$) and cl1216 (*right*; $z = 0.7943$). The images were captured by VLT/FORS2, and taken from https://wwwmpa.mpa-garching.mpg.de/galform/ediscs/.

Mosaic imaging of the 10 highest-redshift clusters was acquired using the F814W filter with the Advanced Camera for Surveys (ACS) on the Hubble Space Telescope (HST) [see Desai et al. (2007), for details]. The ACS has a field of view of roughly $3.5' \times 3.5'$. Using these images, visual morphological classification was undertaken for all galaxies brighter than $I_{\rm auto} = 23$ mag [Desai et al. (2007)], and structural parameters were obtained as well [Simard et al. (2009)]. The correspondence between the parametric morphological classification and the Hubble types is as follows:

- ✯ Ellipticals (E): t = -5;
- ✯ Lenticulars (S0): t = -2;
- ✯ Early spirals (SpE): $t = 1 - 4$;
- ✯ Late spirals and irregulars (SpL): $t = 5 - 11$.

Independent comparisons and simulations of these visual morphologies have demonstrated that ACS images allow differentiating between E, S0, and Sp morphologies below a magnitude limit of $z_{850\ \rm nm} < 24$ mag [Postman et al. (2005)], and these morphologies have been demonstrated to be comparable to those obtained by Fasano et al. (2012) for WINGS and OmegaWINGS, as used in the comparisons performed by Poggianti et al. (2009).

Optical and near-IR data were exploited to measure photometric redshifts used to constrain subsequent spectroscopic observations [Pello et al. (2009)]. These were first

performed in 5 fields and presented in Halliday et al. (2004), while galaxies in another 15 fields were observed with the long-slit multi-object FORS2 spectrograph mounted on VLT UT1 [Milvang-Jensen et al. (2008)]. The field of view of this instrument covers R_{200} for all clusters, except for cl 1232.5–1250, for which it only covers a half virial radius [Poggianti et al. (2006)]. The spectroscopic targets were selected from the I-band catalogs. Typical exposure times were 1-2 hours for the mid-z and 4 hours for the high-z samples. The success rate for the spectroscopic redshifts is 97% above the magnitude limit, thanks to the long exposures. The typical wavelength covered is $\lambda \sim 5300 - 8000$ Å. The size of the slit was 10×1 arcsec^2, with a spectral dispersion of 1.32 or 1.66 Å per pixel. The spectral resolution is FWHM ~ 6 Å, which corresponds to rest-frame 3.8 Å at $z = 0.6$. Cluster and field galaxies were identified through spectroscopic redshifts. Galaxies within $\pm 3\sigma_{cl}$ at the z_{cl} rest-frame were considered as cluster members, while outside that range were flagged as field objects [Halliday et al. (2004), Milvang-Jensen et al. (2008)]. According to these results, the EDisCS clusters have velocity dispersions of $\sigma_{cl} \sim 400 - 1100$ km s^{-1} [Poggianti et al. (2009)].

In addition, three of the fields were imaged in Hα [cl 1040-1155, cl 1054-1255, and cl 1216-1201; Finn et al. (2005)], and another three in X-rays with the XMM-Newton telescope [cl 1216-1201, cl 1054-1145, and cl 1040-1155; Johnson et al. (2006)]. Table B.1 in Appendix B lists the EDisCS clusters, together with their main properties, highlighting those for which stellar characteristics were obtained with SINOPSIS.

7.2 PHYSICAL PROPERTIES OF THE EDISCS SAMPLE

Throughout this thesis, we have controlled for and fixed two of the most important factors in galaxy evolution, namely, stellar mass, and morphology. We now proceed similarly, with the goal of carrying out a meaningful comparison between the low-z, and the mid- and high-z samples. With this in mind, hereinafter we present results only for galaxies for which we have a morphological classification and a spectrum. The total number of galaxies complying with these requirements is 243, and they belong to the following clusters: cl1037.9-1243, cl1040.7-1155, cl1054.4-1146, cl1054.7-1245, cl1103.7-1245, cl1138.2-1133, cl1216.8-1201, cl1227.9-1138, cl1232.5-1250, and cl1354.2-1230, which are marked with a ✓ in the last column of Table B.1. For these galaxies, we run the SINOPSIS code with the same configuration adopted for the WINGS+OmegaWINGS galaxies, as explained in Section 3.5.

7.2.1 *Galaxy sample*

Once we ran SINOPSIS on all the galaxies in the EDisCS dataset fulfilling the aforementioned requirements, we visually inspected all the 243 spectra and corresponding models as a sanity check. In this examination, we discovered that the

redshifts given in the catalog were wrong for ten galaxies, and we recalculated them, based on both absorption and emission lines (when the latter were present). We ran the code again for these spectra, with the corrected redshift, and obtained a good fit for nine of them. In the end, we only discarded five galaxies for having a bad SNR. From the remaining set, we defined our galaxy sample with those objects complying with the following specifications:

1. Stellar mass $\mathcal{M}_* > 1 \times 10^{10}$ $M_\odot$, approximately the same value used by Vulcani et al. (2013), and roughly equivalent to an absolute magnitude limit $M_V < -19.5$ mag, which corresponds to the limit of the survey at these redshifts, as also used by Poggianti et al. (2009) for the same dataset.

2. A good spectral fit from a visual inspection.

3. Cluster membership (i. e., within $\pm 3\sigma_{cl}$ of the z_{cl} in the rest-frame). However, we also include as members those galaxies in secondary groups of the main clusters.

As EDisCS spectra do not cover the red side, we could not measure the Hα and [NII] lines to exclude a possible AGN contribution. However, we have checked the [OIII]/Hβ ratio and found it to be below the AGN separation line in BPT diagrams [Baldwin et al. (1981)], in a very wide range of [NII]/Hα ratios. Hence, a possible contribution of an AGN to line ionization must be very small. SFRs were estimated by measuring the Hβ line, and the [OII] doublet. Other lines mentioned in Section 3.1 were also measured by the code to fit the spectrum.

For the comparison between high- and low-z samples to be meaningful, we redefine the WINGS/OmegaWINGS sample (first built and presented in Section 4.1), using the same stellar mass limit applied to EDisCS galaxies, while keeping the previous definitions of cluster membership and goodness of fit ($\chi^2 < 5$). The final EDisCS sample contains 161 galaxies. The quantities and fractions by morphology are presented in Table 7.1, as well as the numbers and fractions for the newly defined WINGS+OmegaWINGS galaxy sample used here. We also plot the distributions of redshifts for the galaxies selected in both samples in Figure 7.2.

7.2.2 *Stellar mass distribution*

The stellar mass function of cluster and field galaxies at $z \sim 1.5$ was analyzed by Nantais et al. (2016), who found no difference between the two environments. We studied the stellar mass distribution of WINGS+OmegaWINGS galaxies, and compared cluster and field galaxies separated by morphology, in Section 4.3. Now, once we have defined the sample of EDisCS galaxies and the new WINGS+OmegaWINGS sample, we compare their total stellar mass distributions. The resulting histograms are shown in Figure 7.3 (left), normalized to their heights. In the right panel, we show the

Table 7.1: Numbers and fractions of galaxies by morphological type in the EDisCS and WINGS+OmegaWINGS galaxy samples used here. The uncertainties correspond to binomial errors.

Type	EDisCS		WINGS/OmegaWINGS	
	N	Fraction	N	Fraction
E	34	$21.1 \pm 3.2\%$	872	$29.8 \pm 0.8\%$
S0	28	$17.4 \pm 3.0\%$	1235	$42.2 \pm 0.9\%$
SpE	69	$42.9 \pm 3.9\%$	699	$23.9 \pm 0.8\%$
SpL	30	$18.6 \pm 3.1\%$	119	$4.1 \pm 0.4\%$

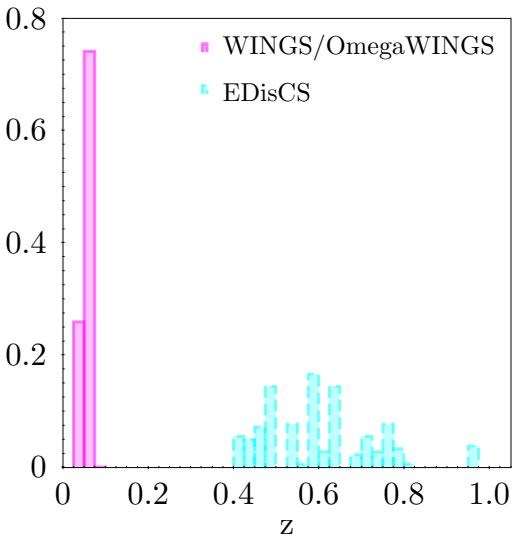

Figure 7.2: Redshift distributions, normalized to the total height of histogram bars, for both WINGS/OmegaWINGS (*magenta solid line*) and EDisCS (*cyan dashed line*) galaxy samples.

cumulative mass distributions, for which we implement the K-S test. The values obtained are $P = 0.174$, $D = 0.090$, meaning that both distributions are drawn from the same parent one. Therefore, in the following, we can compare the results for low and intermediate-high redshift, without being affected or biased by mass-dependent effects. A very small excess of very massive galaxies is present in local clusters, but their number is very small and hence will not influence the comparison.

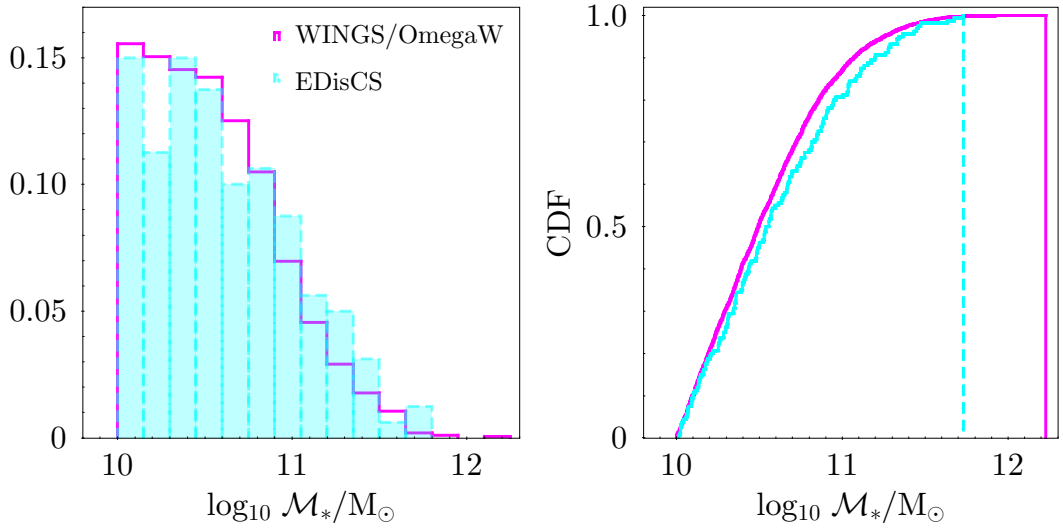

Figure 7.3: Stellar mass distributions normalized by the total histogram height (*left*), and cumulative mass distributions (*right*), for the WINGS/OmegaWINGS (*magenta solid lines*) and EDisCS (*cyan dashed lines*) galaxy samples.

7.2.3 *Color–magnitude and color–mass diagrams*

Colors and magnitudes of WINGS/OmegaWINGS galaxies were studied in Section 4.4. Here, we use absolute magnitudes calculated by SINOPSIS to obtain the $M_B - M_V$ (rest-frame) colors of EDisCS galaxies. As we have mentioned, EDisCS spectra were taken through long-slit spectroscopy, and one of the outputs generated by SINOPSIS is the magnitude (apparent and absolute) at different photometric bands. Similarly to Equation 4.3, we can approximate the total color of the galaxy by the color in the slit, as follows:

$$\text{Color} : M_B^T - M_V^T \approx M_B^S - M_V^S, \tag{7.1}$$

with the super indices T corresponding to total, and S to slit. Note that, in this case, we are less prone to effects from possible color gradients within the galaxies, since the slit samples their outer parts as well. In this way, we can plot the color–mass and color–magnitude diagrams for the EDisCS galaxy sample broadly separated into early and late morphologies. The result is shown in Figure 7.4.

We recover the well-known red and blue clouds. While early-type galaxies are constrained to a small range in color, colors of late types are distributed in more extended regions, with higher densities in bluer colors. Compared to low-z (Figure 4.4), where the color peak of late types falls around 0.7 mag, high-z late types are bluer, with their peak around $0.5 - 0.65$ mag. Results are similar to Cerulo et

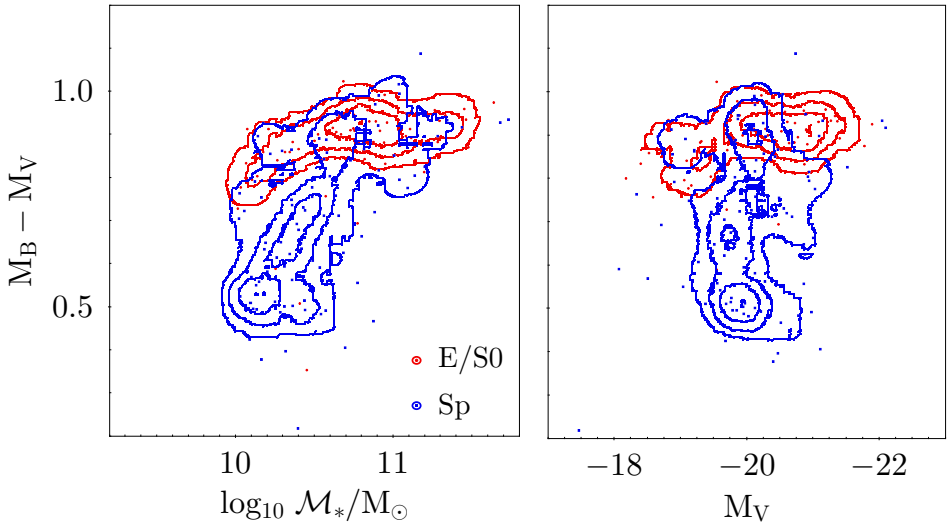

Figure 7.4: Color–mass (*left*) and color–magnitude (*right*) diagrams for the EDisCS galaxy sample. *Red points and number density isocontours:* early-type galaxies; *blue points and number density isocontours:* late-type galaxies.

al. (2016), who found that local clusters host redder galaxies than clusters at higher redshifts. However, our statistics are too poor for a reliable comparison. For this reason, this time we only classify galaxy morphologies into early or late types, but we cannot divide galaxies by bins of stellar mass or luminosity.

We witness the well-known Butcher-Oemler effect, [e. g., Butcher & Oemler (1978)], i. e., the scarcity of blue, SF, galaxies in the core of local clusters, while they are abundant in high redshift ones. More in general, we attest to the evolution of the blue galaxy fraction in clusters with redshift. This result has also been confirmed by Hudson et al. (2010) and, for higher redshifts ($z > 0.5$), by, e. g., Cantale et al. (2016), as well.

7.3 ACTIVELY STAR-FORMING GALAXIES

Nantais et al. (2016), using four galaxy clusters between $1.37 < z < 1.63$, studied the fraction of actively SF galaxies with a limit in stellar mass similar to ours. They found that passive galaxies in clusters constitute roughly 50% at all masses, while in the field this fraction is only 20% at low masses, but higher for high-mass galaxies. These results highlight the relevance of environmental quenching, even at these high redshifts.

We presented the fractions of SF cluster and field WINGS/OmegaWINGS galaxies in Table 4.5. We remind the reader that SF galaxies are defined as those having an $\mathrm{SFR}_1 > 10^{-3}\ M_\odot \mathrm{yr}^{-1}$ (Equation 4.5). We now use the new samples to estimate the

Table 7.2: Fraction of actively SF galaxies by morphological type in the EDisCS and WINGS+OmegaWINGS galaxy samples used here. The uncertainties correspond to binomial errors.

Type	EDisCS	WINGS+OmegaWINGS
All	$59.6 \pm 3.9\%$	$28.8 \pm 0.8\%$
E	$23.5 \pm 7.3\%$	$19.5 \pm 1.3\%$
S0	$42.9 \pm 9.4\%$	$21.9 \pm 1.2\%$
SpE	$72.5 \pm 5.4\%$	$46.2 \pm 1.9\%$
SpL	$86.7 \pm 6.2\%$	$67.2 \pm 4.3\%$

SF galaxy population and obtain the quenching factors in the cluster environment. Results are listed in Table 7.2, divided by morphology. Going from high- to low-z, for all types together, the population of galaxies with star formation decreases by half. The SF fraction of ellipticals is barely changing, while substantial differences are observed for the other morphological types: SF S0s are twice as common at high-z, and the SF fraction is substantially higher also for spirals. If we interpret early spirals as a population of objects recently accreted into clusters (as we did for WINGS/OmegaWINGS), this would lead us to conclude that high-z clusters, either are less efficient at turning off star formation or have not had enough time to shut it down. Almost three out of four early spirals are still forming stars at high-z, a considerably higher fraction than the SF half we find at low-z. The same difference, even though less dramatic, is encountered in late spirals, the vast majority of which are still SF in high-z clusters.

7.3.1 *Phase–space diagram*

We now explore the position of SF and quenched galaxies in phase space, as we studied in Section 4.6 for local cluster galaxies. For the rest of this section, we only use the galaxy sample with membership one, i. e., galaxies belonging only to the main cluster and not to other bound groups. We do not separate by morphology, as statistics are not good enough to also divide into SF/quenched. In Figure 7.5, we present the phase–space diagram (i. e., the absolute value of the difference between galaxy velocity and mean cluster velocity, in units of cluster velocity dispersion, as a function of projected distance to the cluster center, in units of cluster virial radius).

Like at low-z, high-z quenched cluster galaxies are located closer to the cluster center, at only 0.64 R_{200}, on average and in projection. SF galaxies are located almost

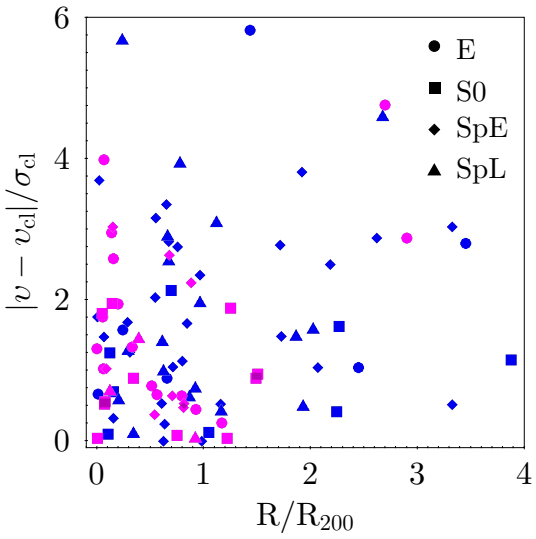

Figure 7.5: Phase–space diagram for galaxies in the EDisCS sample. *Blue symbols:* SF; *magenta symbols:* quenched. Morphologies are indicated by different symbol shapes, as labeled.

everywhere in this diagram, on average, at 1.1 R_{200}. Regarding the velocities, the average values are $|\Delta v|/\sigma_{cl} = 1.35$ and 1.66 for quenched and SF, respectively.

Using simulations, Mahajané et al. (2011), Oman et al. (2013) established that galaxies already found in an advanced state of dynamical equilibrium within clusters are sitting at small radii ($R/R_{200} < 1.0$) and small velocities ($|\Delta v|/\sigma_{cl} < 2$), while outside this region galaxies are either falling for the first time or have just passed through the cluster center (the so-called backsplash galaxies). In Figure 7.5, we can see in the innermost region the majority of the quenched and older galaxies, while in the outskirts most of the galaxies have young populations and harbor emission lines, as also found by Rudnick et al. (2017) for EDisCS clusters.

7.3.2 *Star-forming fraction and projected distance*

We now analyze the galaxy fraction with ongoing/recent star formation, as a function of distance to the cluster center, similarly to what we have done in subsection 4.7.1. We compare, in Figure 7.6, the SF and quenched fractions of galaxies in the EDisCS and WINGS/OmegaWINGS samples, taking three bins of projected distance. First, we have that the galaxy sample at high-z spans a higher range in R/R_{200} than the low-z sample. Although error bars in the EDisCS fractions are much larger than in WINGS/OmegaWINGS, clearly galaxies at high-z are more actively SF than their low-z counterparts. The population of SF galaxies at high-z is considerably reduced, from 71% in the outermost bin, to 44% in the innermost region. On the other hand, the SF

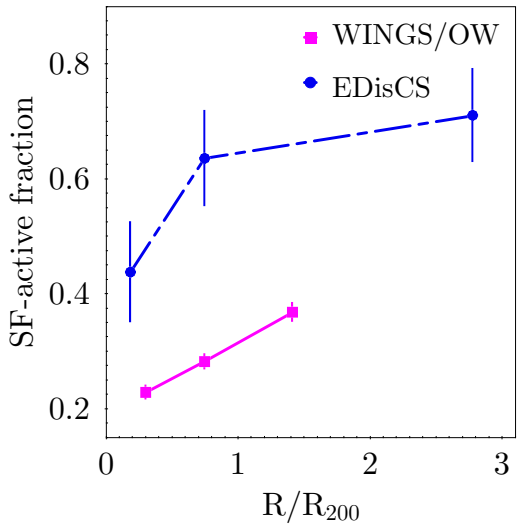

Figure 7.6: Actively SF fractions of galaxies, as a function of clustercentric distance. *Blue circles* and *short-long dashed line:* EDisCS; *magenta squares* and *solid line:* WINGS+OmegaWINGS. The uncertainties correspond to binomial errors.

fraction in WINGS/OmegaWINGS goes from 37% to 23% between the outskirts and the cluster centers.

Our results are in very good agreement with Barsanti et al. (2018), who used a galaxy sample in clusters/groups with $0.05 < z < 0.2$, and obtained that SF fraction drops from $R/R_{200} \sim 3.0$ towards the cluster center. Even though we do not have enough galaxies in the sample to simultaneously separate by morphologies, projected distances, and SF activity, it is possible to compare SF fractions at different redshifts. This comparison seems to suggest that the reason for the higher fractions of SF galaxies at all clustercentric distances in high-z clusters is that, essentially, the SF population was more numerous in the past. This is consistent with the cosmic SFR density as a function of z [see, e. g., Madau & Dickinson (2014)]. These galaxies might hence be feeding the cluster. Additionally, this fraction of SF galaxies at high-z suddenly drops just at 1 R_{200}, indicating a higher cluster efficiency as compared to the ones in the local universe.

7.3.3 *Star-forming fraction and cluster mass*

In subsection 4.7.2, we studied the SF fraction of WINGS+OmegaWINGS galaxies, as a function of cluster mass proxies (σ_{cl}, L_X). We obtained that more massive clusters are slightly more efficient in quenching star formation. Here, we repeat this analysis and compare galaxy samples in the two redshift ranges used, as displayed in Figure 7.7. We do not possess cluster X-ray luminosities, but we use the σ_{cl} values listed in

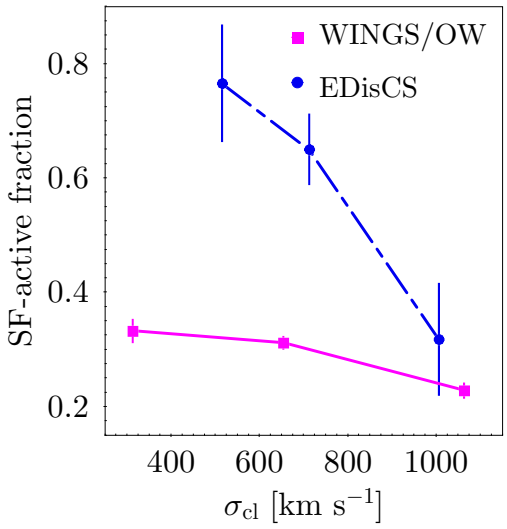

Figure 7.7: Actively SF galaxy fraction, as a function of cluster velocity dispersion. *Blue circles* and *short-long dashed line:* EDisCS; *magenta squares* and *solid line:* WINGS+OmegaWINGS. The uncertainties correspond to binomial errors.

Table B.1 (Appendix B) for EDisCS clusters. The SF fraction decreases with increasing σ_{cl}, and this decline is much stronger in high-z clusters, where it goes from 77% to 32% between small- and large-σ_{cl} bins. Conversely, in low-z clusters, the SF fraction falls from 33% to 23%. Despite the range of cluster masses being slightly smaller for the EDisCS sample, this result seems to be pointing at mechanisms that quickly shut down star formation in younger clusters.

Our results are in very good agreement with Poggianti et al. (2006), who also used EDisCS to study galaxies whose spectra displayed an [OII] line emission with EW $>$ 3 Å, as a signature of ongoing star formation. Their results show a broad inverse correlation with some scattering, suggesting that cluster mass determines the proportion of SF galaxies at these redshifts, with the possible fraction of SF galaxies decreasing with increasing cluster mass. This result is reminiscent of Rudnick et al. (2017), who found a similar outcome for the [OII]$-\sigma_{cl}$ relation.

7.4 THE MAIN-SEQUENCE

The MS of SF galaxies has been observed at both low- [e. g., Paccagnella et al. (2016)] and high-z [e. g., Pearson et al. 2018), but see also Noeske et al. (2007) for a comprehensive review of the topic]. It is well known that the MS evolves with redshift, such that, at fixed mass, galaxies have higher SFRs at larger redshifts [e. g., Lindholmer & Pimbblet (2019), Leslie et al. (2020), Popesso et al. 2023)].

We first studied the MS using WINGS/OmegaWINGS data in Section 4.8. Here, we plot sSFR against $\mathcal{M}_*$ for SF galaxies. To avoid different normalizations of total

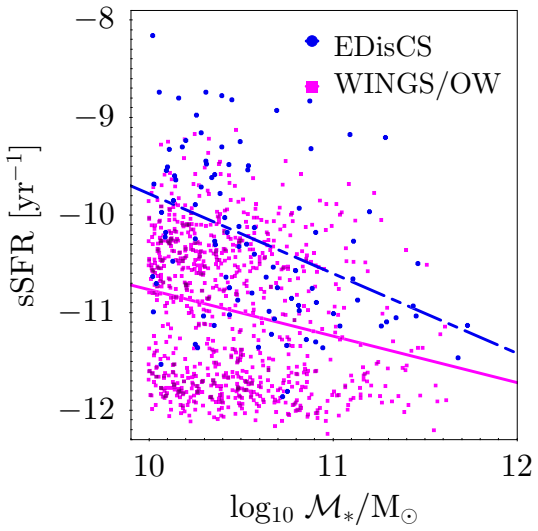

Figure 7.8: sSFR *versus* stellar mass. *Blue circles* and *short-long dashed line*: EDisCS; *magenta squares* and *solid line:* WINGS/OmegaWINGS. Lines represent the best-linear fit. MS of high-z galaxies is above low-z ones at all stellar masses.

stellar mass due to aperture corrections in both samples (the WINGS/OmegaWINGS galaxies have aperture spectra, while slit spectra were obtained for those in EDisCS), we normalize the sSFRs by the stellar mass in the aperture/slit, and not by the total mass. Hence, we cannot compare absolute values on the MS, but we can compare trends, taking into account this caveat.

We compare the MSs of both samples, as shown Figure 7.8. We observe the clear evolution of MS with redshift: the sSFR of low-mass galaxies is about 1 dex higher in EDisCS than in WINGS/OmegaWINGS. According to [Noeske et al. (2007)], this reduction of sSFR for all stellar masses seems to be gradual, with gas exhaustion as the main candidate cause. Another important result is that the MS at high-z presents a steeper slope than at low-z. This same finding is reported by Karim et al. (2011), for the same redshift range we explore, and by Pannella et al. (2015) up to $z = 1.5$. These last authors also found that beyond this redshift, the MS flattens out for all masses. It is worth saying that, in our case, the drop of the MS at high-mass galaxies could also be driven by the small number of galaxies and the poor statistics in the highest stellar mass range.

7.5 STAR FORMATION HISTORIES AT HIGH-Z

As we have seen in Chapter 5, for low-z galaxies SFHs depend mainly on morphology, stellar mass, and environment (cluster or field). We also found that there are other factors, such as LD, clustercentric distance, interactions with neighbor galaxies, and cluster mass, that are also able to affect, at least to some degree, the SFRs at different

ages, and can hence contribute to the quenching of star formation. In this section, we leverage the EDisCS dataset to construct SFHs and study how they are affected by the properties and factors mentioned above. At the same time, we compare with the WINGS/OmegaWINGS data to explore the impact of cosmological evolution on the SFHs of galaxies. We use the same galaxy samples defined in subsection 7.2.1.

As we saw in Table 3.1, SFR_4 extends from the onset of star formation until the age of the universe at the z of the data, which for WINGS/OmegaWINGS is about 12.8 Gyr (taking $z = 0.05$)[1]; hence SFR_4 samples a range of about 7 Gyr. On the other hand, EDisCS clusters are observed at an epoch in which the universe was much younger, and the oldest stellar populations are between 6 and 9 Gyr old (corresponding to $z \approx 0.4 - 1$). To construct SFHs of high-z galaxies, we take the mean z of the EDisCS galaxy sample ($z \approx 0.6$; see Figure 7.2), which corresponds to an age of the universe of 7.75 Gyr[2]. This age is much younger than the WINGS/OmegaWINGS limit used ($t_u \approx 12.8$ Gyr). Hence, in the SFHs plots, the maximum ages of EDisCS galaxies are shorter than for WINGS/OmegaWINGS.

7.5.1 *SFH by morphology*

We first analyze the SFHs of galaxies divided into the main four morphological types (Figure 7.9). The most evident difference between EDisCS and WINGS/OmegaWINGS is that the SFRs of high-z galaxies are higher than for those at low-z, for all ages and morphologies (the normalized SFH in the right panel avoids aperture effects in WINGS/OmegaWINGS spectra). This is another way to see the Butcher & Oemler (1978) effect (see Section 1.5). Early-type galaxies form their stars at the oldest ages and evolve to quiescence, as was found by Stanford et al. (1998) in rich clusters at $z = 0.9$. Between SFR_3 and SFR_2, the slope is approximately the same for early types. However, SFR_1 values are higher for early types at high-z, while at low-z the SFR of galaxies, even late types, exhibits a monotonic descent. This is evidence that local cluster galaxies are more quenched than objects at higher redshift. We also have that EDisCS galaxies of all morphologies display a higher SFR in the third age bin than in the fourth one, as the right panel in Figure 7.9 clearly shows. This does not happen for low-z galaxies, which formed most of their stellar mass in the fourth bin. EDisCS galaxies, especially late types, have flatter SFHs, and their present-day SFRs reach high values.

1 Here we utilize the cosmology calculator created by Wright (2006): https://www.astro.ucla.edu/~wright/CosmoCalc.html

2 For a flat universe with the Wilkinson Microwave Anisotropy Probe (WMAP) cosmology constants mentioned at the end of Section 1.6.

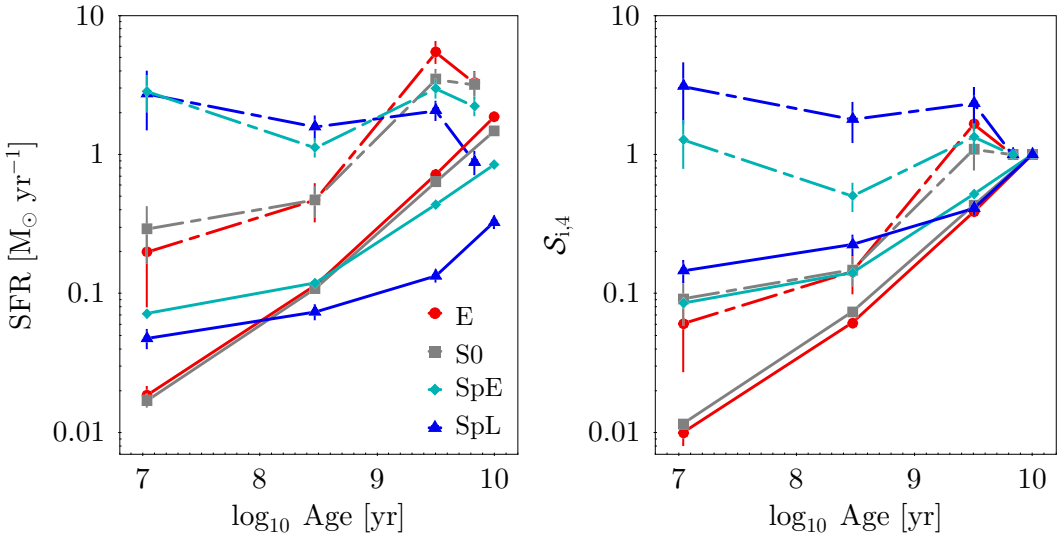

Figure 7.9: SFHs. *Solid lines:* WINGS/OmegaWINGS; *short-long dashed lines:* EDisCS. *Left:* for the main galaxy morphological types. *Right:* same SFHs, normalized by the oldest age bin (SFR_4).

7.5.2 *SFH by stellar mass*

When we study the SFHs of the galaxy samples divided into stellar mass bins, as shown in Figure 7.10 for early- and late-type galaxies, we are witnessing the downsizing effect. This was done in Section 5.2 for the WINGS/OmegaWINGS galaxy sample, and here it is visible in the early-type galaxies for all the redshift ranges available to our datasets. On the other hand, the SFHs of late types of all stellar masses are on average flat, and even enhanced for SFR_1. This effect marks a clear distinction with low-z late types, whose SFHs decrease monotonically.

These results are consistent with the findings of Pacifici et al. (2016) in many respects: stellar mass is one driving factor of galaxy evolution across cosmic time, with high-mass galaxies always evolving faster (i. e., downsizing). At all redshifts and stellar masses (and, from our results, one should also add morphologies), the SFH grows and reaches a peak to then decrease. At low-z, this decline depends on the stellar mass (and galaxy morphology, as observed in Figure 5.2). However, at high-z, the peaks of the SFHs depend on the sampled redshift. For the EDisCS redshift range, the SFR_3 peaks at even higher values than those achieved by the SFR_1. This effect is very likely due to the different age intervals sampled by SFR_4 at high- and low-z, as we have mentioned before.

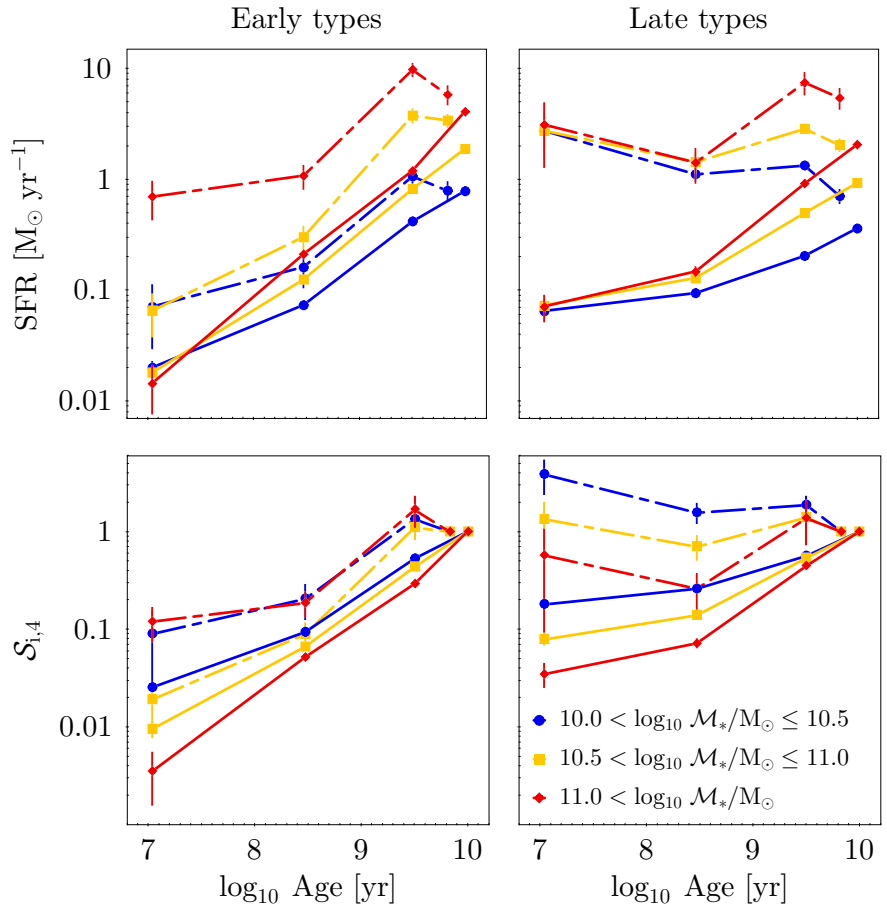

Figure 7.10: SFHs in three bins of stellar mass, as labeled by the colors. *Solid lines:* WINGS/OmegaWINGS; *long-short dashed lines:* EDisCS. *Top:* early- and late-type galaxies. *Bottom:* same SFHs, normalized by the oldest age bin (SFR_4). Error bars are calculated through the bootstrap method.

7.5.3 *SFH by projected distance*

In Section 5.3, we studied the SFRs of WINGS/OmegaWINGS galaxies in clustercentric distance bins. No great trends were found with this environment parameter for any of the four stellar ages used in the SFHs. We now analyze the SFHs of early- and late-type galaxies in three bins of clustercentric distance. The result is displayed in Figure 7.11. Low-z early-type galaxies show a trend only in the SFR_1, which is a bit higher for larger distances. This trend may be attributed to S0s. For late types in this sample, no tendency is seen. As for high-z, early types do not present a correlation with distance, while late types in the cluster outskirts have a higher SFR_1 than those close to the cluster center, in projection. This is better seen in the right-bottom panel of Figure 7.11.

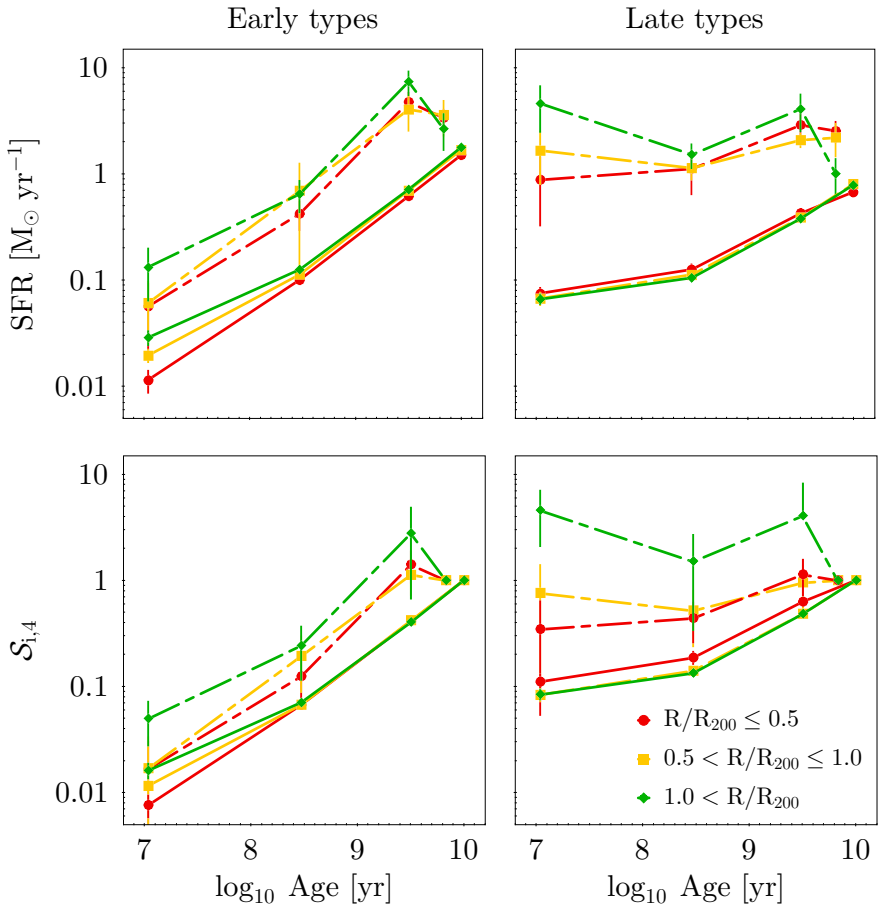

Figure 7.11: SFHs in bins of clustercentric distance, as labeled by the colors. Samples, line types, panels, and errors as in Figure 7.10.

Studying a sample of galaxies in 17 clusters, in a redshift range similar to ours, divided into SF and quenched, Lagana & Ulmer (2018) did not find any correlation between SFR or sSFR and clustercentric distance. However, they did find a correlation with stellar mass and concluded that stellar mass is the dominant factor, more influential than the environment (parameterized by projected distance), in quenching star formation, in agreement with our results. Additionally, McGee et al. (2009) concluded that the environment affects fewer than half of the galaxies with $z > 1.0$, i. e., in the limit of our dataset, and a fraction lower than 20% for $z > 1.5$.

We also tested whether the SFHs are affected by the global environment, parameterized by cluster velocity dispersion. For this, we divided the EDisCS galaxy sample into three bins of σ_{cl}. We did not find any trend in the SFRs at different ages with this property. This result is similar to the previously found with the WINGS/OmegaWINGS galaxy sample in Section 5.6.

Part IV

DISCUSSION AND CONCLUSIONS

8

DISCUSSION OF RESULTS

The analysis we have performed in this work aims at determining the relative and combined importance of stellar mass, morphology, and the environment when trying to detect and quantify the changes that are responsible for the observed properties of galaxies in clusters, especially focusing on the stellar population properties. A key open issue is disentangling the impact of the local and global environment in driving the fate of these galaxies. This is not an easy question to answer, since the characteristics of the local environment are somewhat influenced by those of the global one: for example, more massive clusters are both richer in ICM and galaxies, and this consequently raises the probability that an infalling galaxy will find itself embedded in a denser and hotter medium, with a higher likelihood of galaxy–galaxy interactions as well. For these reasons, recent environmentally–induced changes are more easily visible in later morphological types.

When we consider the morphological fractions of galaxies in local clusters, we do find evidence of a mild effect as a function of total cluster mass, as parameterized either by L_X or σ_{cl}, with hints suggesting that more massive clusters host a larger fraction of S0 galaxies, at the expense of the spiral population (see Figure 2.4 and Figure 2.5 in Section 2.3). This effect may be an indirect consequence of the fact that more massive clusters host a larger number of galaxies, which makes galaxy–galaxy interactions more frequent and galaxy–cluster interactions more efficient. This finding, however, is somewhat different from what Poggianti et al. (2009) concluded, analyzing WINGS data, i. e., that morphological fractions were not significantly different in clusters with different masses. These discrepant results can be explained by the sample used in this work, which includes galaxies that are both fainter and farther from the cluster centers (up to 1 R_{200} and beyond).

Taking into account morphological type fractions is of crucial importance when looking for differences in the stellar populations, in order to properly understand and quantify pure environmental effects. An early-type galaxy located in a cluster is such either because it was born like this, or because it has been transformed. This can happen if the galaxy has spent a significant amount of time in this dense environment. A broad way to study this effect is by looking at the rest-frame colors, at fixed mass: ellipticals and late spirals are almost indistinguishable from their field counterparts in this respect, while early spirals and S0s are found to be systematically and significantly redder in clusters, at all masses. The most straightforward interpretation of the two aforementioned results (morphological type fraction and colors) is that

changes in the stellar populations happen faster than morphological transformation [Balogh et al. (2004)]. On the other hand, the fact that late spirals look alike (in color and also in recent SFR) in clusters and the field, possibly suggests that most of them are relatively new to the cluster environment, as already proposed by Cava et al. (2017), and their overall properties have not been significantly affected yet. Similarly, massive ellipticals may have already been quenched (either by stellar mass or by the environment) at high-z, and their current colors are independent of their present-day environment. Note also that the quenching fraction of the most massive ellipticals does not depend on LD (Figure 5.4), as they are quenched in all environments.

Given that dense environments will eventually quench star formation, differences between cluster and field galaxies should be traceable in their SFH (Figure 5.1), and these effects should be stronger in those galaxies that have spent the longest time in clusters. Indeed, once the stellar mass is taken into account, the mean SFH of cluster galaxies is steeper (i. e., displaying faster quenching) than in the field for all morphologies, directly suggesting a higher quenching efficiency in clusters. This effect is more clearly seen with the quenching indices (see Table 5.1 and Table 5.2): $S_{4,3}$, which reflects the star formation conditions at the earliest epochs of galaxy life, shows, in general, the smallest differences when various morphologies and environments are considered, reflecting a common formation scenario in the distant past. Only when separating by stellar mass, significant and important discrepancies are spotted, which is consistent with galaxy birth and growth in a downsizing scenario [Cowie et al. (1996)]. In fact, from Figure 5.3, it is clear that the most massive galaxies present a higher $S_{4,3}$ index, indicative of faster early growth, compared with less massive ones. Furthermore, from the same figure, $S_{3,2}$ is on average higher for cluster early types and decreases monotonically for late types. This latter trend can be roughly viewed as a consequence of the time a galaxy has spent in the cluster environment, which we expect to be –on average– increasingly larger when going from the earliest to the latest morphological types. The differences encountered for cluster and field ellipticals and S0s might be due to different formation channels for these galaxies. For S0 in particular, several studies point to the existence of two types of lenticular galaxies: those that are born as such, and those that have been transformed into S0 because of environmental effects [Tapia et al. (2017), Fraser-McKelvie et al. (2018b)].

Concerning the star formation in ellipticals, as highlighted in Figure 5.1, the finding that the SFR_1 of elliptical galaxies is significantly higher in the field than in clusters is consistent with the results of Huan & Gu (2009), who found hints that ellipticals in lower-density environments may be more prone to hosting some levels of star formation.

In the comparison between the cluster and field populations, when galaxy stellar mass is taken into account, the differences in quenching are only ascribable to the environment, and they are seen in all morphological types. The mean SFH of cluster spirals (these objects most likely dominate the recently infalling population) only

shows a mild dependence on total cluster mass. This effect is more easily spotted through the $S_{3,2}$ index, whose average values increase with larger cluster mass (i. e., cluster velocity dispersion; Figure 5.13). The $S_{2,1}$ index, where more recent effects (and on a much shorter timescale) should be visible, presents values that are remarkably similar for spirals in clusters and the field. We believe this can be interpreted as a hint that local (both in space and time) effects are the ones driving the ability to form stars, while correlations with global ones are much more difficult to spot: global effects are likely blurred by the collection of different mechanisms acting simultaneously but with different time scales, intensities, and consequences. On the other hand, the fraction of SF spirals is always lower in clusters than in the field, with no correlation with total cluster mass (Figure 4.13).

Both the redder colors and the higher fractions of quenched galaxies in clusters clearly show that a dense environment is hostile to star formation, and will eventually lead galaxies to stop forming stars. Nevertheless, the aforementioned results for $S_{2,1}$ in cluster and field spirals seem at least a first sight, to be inconsistent with this picture. A likely explanation for the behavior of $S_{2,1}$ may lie in the very short timescale probed by emission lines, which are the observable used to calculate the current SFR. This makes the SFR_1 calculation subject to the probability of observing a galaxy in a SF or in a quenched phase which, in turn, depends on currently ongoing interactions. For example, the presence of a nearby companion may both trigger and suppress a certain level of star formation activity (see also discussion below), and RP has been demonstrated to be able to induce star formation as well. Conversely, SFR_2 probes a timescale more than 20 times longer, and hence it may be a better tracer of the cumulative effects of the mechanisms at play, which will eventually lead to quenching and we seem able to observe through $S_{3,2}$.

This picture is supported by the characteristics of the MS relation observed for SF cluster galaxies. While the dispersion of the MS in ellipticals is the same in cluster and field, the relation for S0s, SpEs, and SpLs in clusters exhibits a larger scatter than in the field (Figure 4.14). Although the slope by morphology is similar in the two environments, the steepest slope corresponds to SpEs, a signal of a stronger dependency of star formation on stellar mass. Cluster galaxies, especially spirals, show both higher and lower star formation levels than field ones, something that can be attributed to the different interactions that cluster galaxies undergo, both enhancing and suppressing the SFR (note that this phenomenon is likely to be short-lived since we only see it in SFR_1). The presence of a population of galaxies with significantly higher SFR in particular, seems odd, given that the cluster environment is notoriously adverse to maintaining star formation. However, it may be explained as the product of the first stages of interaction with the cluster during which RP, before stripping away the ISM from the galaxies, induces a star formation episode, as has been observed both in numerical simulations [e. g., Fujita & Nagashima (1999), Kronberger et al. (2008), Kapferer et al. (2009)] and in real data [e. g., Vulcani et al. (2018), Roberts

& Parker (2020), Fritz et al., in prep.]. This should be the case as long as interactions do not affect the morphology so much that early spirals cease to be classified as such [Lambas et al. (2012)].

In an effort to study the role played by the environment, we searched for possible differences in SFR_1 and SFR_2, at various projected clustercentric distances and LD values. We have done so for the different morphological types and separated by stellar mass as well, to better isolate the influence of each factor (Figure 5.5 and Figure 5.7). Firstly, we found no significant variations in SFR_1 as a function of stellar mass, neither for ellipticals nor S0s, at all clustercentric distances. Secondly, S0 galaxies, which represent the dominant cluster population, display somewhat increasing SFRs as a function of increasing distance to the cluster center, again independently of stellar mass. For ellipticals, however, the trend is not clear. The fact that the present SFR of early types is independent of the stellar mass is an indication that the star-formation mode/mechanism currently at play is different from that in spirals [e. g., Silk et al. (2014)]. Since early-type galaxies are gas-poor objects today, the most important factor to determine their SFR would not be the amount of available gas, but rather external agents, like RP [Sheen et al. (2017)], neighbor interactions, and the availability of wet mergers [Lee et al. (2023)], which may trigger star formation. This is further supported by the fact that an SFR–mass relation may exist for the SFR_2 of early types (see Figure 5.5), suggesting that processes that enhance and quench star formation are both at play in clusters, but that the former are much shorter-lived and less frequent.

In the case of spirals, separated into stellar mass bins, SFR_1 increases with decreasing radius. The rise in SFR_1 from the outskirts is, indeed, mild, but common to all mass bins. This is observed until about 0.5 R_{200}, after which SFR_1 decreases towards the innermost regions (note that, even though pronounced, the fall at high masses is characterized by large uncertainties). This decrement is more pronounced in more massive clusters, when σ_{cl} is taken as the cluster mass proxy. The result is not clear when L_X is considered.

Figure 5.5 also suggests that spirals closer in projection to the cluster center are more prone to quenching in the high- and intermediate-mass bins, although this result needs to be taken with some caution because of the uncertainties, to which projection effects might also be contributing. The results for SFR_2 strongly resemble those for SFR_1 (again Figure 5.5): the only difference is that the SFR_2 of the most massive cluster spirals can be as high as in the field, with a maximum at around 0.5 R_{200}. This is consistent with RP promoting star formation, and would naturally explain why at present the SFR of the most massive cluster galaxies is lower than in the field: their first SF episode would have consumed a significant fraction of their gas and, together with gas stripping, would more quickly lead to the halting of star formation, owing to gas depletion.

A similar analysis was conducted by taking into account the LD (Figure 5.7). If no distinction is made on morphological type, LD affects SFR_1, with higher densities

resulting in lower SFR_1. However, when the morphological class is considered, we see that the relation between SFR_1 and LD is driven by Es and S0s, while for spirals SFR_1 is flat or even increases with growing LD. On the other hand, SFR_2 seems to be quite unaware of LD, for all morphologies and stellar masses. The only clear difference is seen with respect to field galaxies, which display higher values of both SFR_2 and SFR_1.

The fact that SFR_2 shows no significant trend with LD can be interpreted as evidence that, at the age sampled by SFR_2, the local environment has already had a strong quenching effect on the star formation activity, something that is also supported by a high $S_{3,2}$ quenching index. $S_{3,2}$ would be, of course, stronger for early-type galaxies, which have spent, on average, the longest time within the cluster.

Exactly pinpointing the physical mechanisms responsible for this is, however, quite tricky: the inner regions of clusters are denser both in terms of the ICM and galaxy number, and interactions are thus potentially very effective. Recently, Vulcani et al. (2022), exploiting the same dataset used in this work, have shown that the large majority of spirals are very likely to be affected by RPS at some point during their accretion into clusters, and this mechanism is more efficient in the inner cluster regions [e. g., Zinger et al. (2018)]. Moreover, it is in these same regions that rapid encounters with early-type galaxies are expected to be more frequent and, hence, more effective to accelerate the quenching process.

Taken at face value, our results seem to imply that clusters quench star formation more drastically in early- than in late-types, as differences with the field are stronger in the former. This is likely a direct consequence of the amount of time spent within a cluster. An alternative interpretation is that early types are such because they have suffered more interactions with other galaxies and the environment than late types (see Section 1.4), and probably for a longer time, while late types are such because they have been less affected and, thus, able to keep their morphology, independently of their location in the cluster. Furthermore, in some cases, cluster late-types display average SFR values higher than in the field (see, e. g., the SFR–mass relation for spirals). This apparently counterintuitive, result can be understood when interactions within galaxy clusters are taken into account, as follows.

Several of the findings so far presented and discussed have a quite natural explanation in the frame of binary interactions mechanism. With the purpose of studying both the hydrodynamical and the gravitational/tidal effects of the galaxy–galaxy interactions, Park & Hwang (2009) and Park & Choi (2009) analyzed galactic properties in relation to the distance and the morphology of their closest neighbor. According to their results, a late-type galaxy located within a neighbor's virial radius is affected in different ways, depending on the neighbor's morphology: a late-type neighbor can provide gas and trigger star formation, while the extended hot gas halo of an early-type can act as a quenching agent, as also found by Patton et al. (2020) with simulations, and Cao et al. (2016) using observations.

We performed a similar analysis, looking for changes in the SFH, quenching indices, color, and luminosity of galaxies, separated by morphological type, as a function of clustercentric distance to and morphology (early- or late-type) of their closest neighbor. Unlike what we found for the clustercentric distance and the LD, a close encounter clearly affects the recent SFR: both early- and late-type galaxies display an enhancement in SFR_1 when they are located within the virial radius of a late-type closest neighbor. Similarly, the $S_{2,1}$ quenching index increases when a galaxy is within the virial radius of an early-type closest neighbor. These results are statistically more significant when spirals are considered, while for early types, even though trends are observed, average values are within the confidence intervals. Somewhat counter-intuitively, the fraction of SF spirals steeply declines when located within one virial radius of a companion, independently of its morphology (see Figure 5.10), while, at the same time, SFR_1 is higher in spirals when they are within one virial radius of another spiral. This apparent contradiction might indicate that the enhanced star formation activity triggered by the hydrodynamic interaction with the late-type companion is short-lived: the interaction initially produces an increase of the SFR that quickly consumes part of the available gas, which in turn quenches the galaxy and decreases the SF fraction.

SFR_2 and $S_{3,2}$ (as opposed to SFR_1 and $S_{2,1}$) do not seem to be affected by closest neighbor properties. This may actually be the consequence of three factors: (a) as demonstrated by Hwang et al. (2018), the timescales of galaxy–galaxy encounters are very short; (b) SFR_2 averages the stellar population properties and galaxy interactions over more than 0.5 Gyr; (c) at earlier epochs, spiral galaxies were likely in less dense environments, hence experiencing less frequent encounters. In the case of early-type galaxies, the reduction in the average SFR with decreasing neighbor distance is likely a secondary effect of the morphology–density relation: a denser environment is both more likely to host early-types and to be located in the innermost parts of a cluster. There, both the galaxy and the ICM densities reach their highest values and are hence more likely to negatively affect the onset of star formation.

The influence of the closest neighbor is indeed modulated by the local environment, particularly by the LD (see Figure 5.11): quenching effects are stronger at low LD values, while at high LD the trends with distance and morphology of the neighbor are, on average, flat. We can think of two possible explanations for this: firstly, since on average higher densities occur at smaller clustercentric radii, galaxies have likely already lost most of their cold gas; secondly, encounters among galaxies there, although more frequent, are faster and hence shorter-lived.

Supporting this idea, Hwang et al. (2018), using numerical simulations, found that high-speed multiple hydrodynamical interactions between a spiral and an early-type will eventually result in a loss of about 50% of gas after six edge-on collisions, and about 90% if the collisions are face-on. Interactions with the ICM will yield a similar gas loss, according to simulations [Jáchym et al. (2007)]. This result is confirmed by

Figure 5.12 (right panel): the SF fraction, at fixed neighbor distance, decreases more strongly at high than at low LD.

By the same token, while the average value of SFR_1 in spiral galaxies seems to be unaffected by either LD or by clustercentric distance, the fraction of SF spirals does show negative and positive correlations, respectively, with decreasing distance and LD (see Figure 4.12): eventually, dense environments (gauged both by the number of galaxies and ICM density) will lead to the quenching of star formation, but on timescales larger than those probed by SFR_1. Mechanisms, such as RP or binary interactions, can trigger a star-formation burst on short timescales, likely to be followed by a sudden quenching. The fact that we observe similar trends in the average SFR_1 and the quenched fraction, as a function of both LD and distance, is again consistent with a short duration and high intensity of this active phase. This is also reflected in higher SFR_1 for cluster than field spirals in the lowest mass bin, at both small cluster radii and high density (see Figure 5.5 and Figure 5.7).

This brings us to the question of whether it is the position within the cluster or LD the most important factor affecting galaxy properties. We have found an indication that, at least concerning the SF fraction, the effect of clustercentric distance is marginally stronger (see Figure 5.12). The two aspects are, however, not independent: the density of galaxies is higher in the cluster center, where the ICM also reaches its peak density, so the two effects would add up. On the other hand, a galaxy might be located in a substructure of high galaxy density at a large galactocentric distance, hence in a region of lower ICM density; in this case, the effects of high galaxy number density will not be aided as much by the ICM.

With the purpose of disentangling the two parameters, we analyzed the quenching indices for different morphologies, simultaneously taking into account clustercentric distance and LD.

As probed by $S_{3,2}$, clustercentric distance seems to play a larger part in star formation quenching for S0s, while SpEs seem to be equally affected by distance and LD, with the strongest quenching occurring at the highest LD and the shortest distances. This may indicate, not only that the combined effect of the two produces the most efficient quenching, but also that star formation suppression is more likely visible after about 0.5 Gyr, the average half-crossing time for galaxies in clusters. On the other hand, quenching at the most recent epochs (revealed by $S_{2,1}$) is significantly higher in clusters than in the field only for early-type galaxies; for late-types, quenching is on average very similar, if not indistinguishable, in clusters and the field.

The latter result is coherently explained by the other findings gathered so far: the cluster environment will ultimately act as a quenching agent of star formation in recently infalling, SF (gas-rich), galaxies. However, there are several mechanisms, such as RP and binary interactions, that might briefly boost star formation, hence

partially compensating –on average– for the quenching, and making star formation and quenching indicators similar to those in the field.

Since star formation is much rarer in ellipticals, the quenching index $S_{2,1}$ is highest for them among all morphologies, with a stronger dependence on LD than on clustercentric distance. The relations, however, show a quite width confidence interval. This is naturally explained by interactions with nearby late-type companions in cluster outskirts.

Differences in stellar content as a function of global cluster properties suggest that the local environment (e. g., interactions among galaxies) has stronger effects than the global large-scale one (e. g., cluster-galaxy interactions) in shaping present galaxy stellar properties, such as the stellar mass distribution [Vulcani et al. (2012)] and the SFR–stellar mass relation [Calvi et al. (2018)]. In fact, variations in stellar populations are more pronounced (even though sometimes subtle) relative to local properties, and their intensity/significance depends on morphology.

Clearly, different mechanisms can act at the same time, with different intensities and scale times. These include harassment, thermal evaporation, RPS, and starvation. They are correlated, either with the presence of nearby companions (i. e., the LD) or with the clustercentric distance (i. e., the local characteristics of the ICM), and affect both the content and the physical conditions of the gas and, hence, the ability of a galaxy to form stars. Our results indicate that the preferred processes are RPS (in the inner parts of clusters, preferably where $R/R_{200} < 0.5$), harassment (with repetitive galaxy encounters at low LD), and tidal interactions (which quench star formation if the companion is an early-type, or raise the SFR when the closest neighbor is a spiral). Preprocessing, acting in the cluster outskirts, may be playing a part too. All these phenomena can act on galaxies of all stellar masses [Bamford et al. (2009)], even on some located in the field, where there are both quenched spirals and early types with some degree of star formation activity.

Superimposed on all the effects and mechanisms analyzed and discussed above, which are all external in nature, we have also studied the effect of stellar bars, an internal property that is effective at redistributing the gas content in galaxies, possibly affecting their ability to form stars. In the paper by Tawfeek et al. (2022), we have applied an automatic stellar bar detection algorithm to the OmegaWINGS V-band images, to compile a catalog of barred galaxies.

While further separating galaxies based on this characteristic as well would probably add more noise, we clearly have found evidence of a morphology-driven effect in the presence of stellar bars. These structures are formed only in disk galaxies and are destroyed in morphological transformations from late to early types, such as those that happen in clusters. The first clear result is that the effects of cluster environment (in all of its aspects) on galaxy morphology are more pronounced when the galaxy has a bar. As for the stellar populations, if we expect any difference between barred and non-barred galaxies, this would be in the center, since stellar bars

are known to sweep gas within the disk and funnel it towards the center, possibly triggering star formation [Tawfeek et al. (2022)]. These effects should not go missing from our data, as fiber spectra are exactly sampling the central regions, the very place that is potentially affected by these mechanisms.

Indeed, barred galaxies show –on average– the tendency to host younger stellar populations (as probed by quenching indexes) and more active star formation. This would be, of course, something that is mostly affecting spiral galaxies, as the fraction of bars in early types is very small (and in any case only limited to S0). We do not expect that taking into account the presence/absence of a stellar bar should change any of the results presented and discussed so far. This is because, all the trends regarding the presence of bars found, analyzed, and discussed by Tawfeek et al. (2022), are traceable to morphology which we do take into account as a main parameter.

This particular effect was also analyzed by Sánchez-García et al. (2023) on a much smaller number of galaxies, but with spatially resolved data, from the GASP sample (see their Fig. 8). They found a clear central sSFR enhancement which, in galaxies that are barred and simultaneously strongly RP-affected, is the strongest, hinting for the first time at a combined effect of an internal (bar) and external (RP) enhancing the star formation.

8.0.1 *A comparison with galaxy clusters at high redshift*

Some of the most noticeable and remarkable effects of the environment on galaxy properties and evolution are surely those on morphology. Using HST data of 20 EDisCS clusters, Desai et al. (2007) did not find evidence of evolution in the morphological fraction over a redshift range $0.4 < z < 1.25$. On the other hand, Poggianti et al. (2009) compared the morphological fractions between local and more distant clusters ($z \sim 1$). The typical morphological fractions obtained were 0.3, 0.15, and 0.55, for ellipticals, S0s, and spirals (including irregulars), respectively. At lower redshifts (from $z < 0.5$) [e. g., Fasano et al. (2000)], the elliptical fraction remains constant, but the S0 fraction decreases by a factor of two, while the spiral fraction rises by a similar factor. Desai et al. (2007) agree that evolution in the S0 and spiral populations is observed up to $z \sim 0.4$, at least within the cluster mass range probed by their sample.

Furthermore, using both EDisCS cluster galaxies (within 0.6 R_{200}) and the results of Postman et al. (2005) for seven clusters with $0.8 < z < 1.27$ (within 1 R_{200}), Desai et al. (2007) studied the dependence of morphological content on cluster velocity dispersion, σ_{cl}. They found statistically significant (at the $\lesssim 3\sigma$ level) correlations for early and late types. While between $\sigma_{cl} \sim 200$ km s^{-1} and $\sigma_{cl} \sim 1200$ km s^{-1} the early-type fraction increases from $\sim$ 10% to $\sim$ 80%, the late-type content drops roughly in the same proportion.

These trends should be taken into account when comparing galaxies at different redshifts because, as extensively demonstrated in this thesis, disparate morphological types clearly present distinct SFHs and are susceptible to environmental influences in diverse ways and amounts. A one-to-one comparison between the SFHs of galaxies at different cosmic epochs is not an easy task, since the stellar populations sampled at various redshifts clearly are not the same: the oldest SSP is about 12.8 Gyr for WINGS/OmegaWINGS and goes from ~ 9 Gyr (at $z \sim 0.4$) to ~ 5.7 Gyr (at $z \sim 1.0$) for galaxies in the EDisCS sample.

Regardless, and taking advantage of the fact that the stellar mass distributions in the WINGS/OmegaWINGS and EDisCS samples are very similar, we can perform a qualitative comparison of the effects of the environment on the galaxy properties. Again, we focus on the stellar populations. We start with the color–mass (or color–magnitude) diagram (Figure 7.4). We need to consider that the stellar populations in the EDisCS galaxies are about $4 - 7$ Gyr younger than those in WINGS/OmegaWINGS, hence their colors are different, as well as their mass-to-light ratios. What we do observe in the EDisCS sample is a well-defined red cloud where ellipticals and S0 are found, while galaxies of later morphological types are spread across the whole range of colors. This finding is similar to that of Mei et al. (2009) at $0.8 < z < 1.2$, for rest–frame $(U - B)$ colors. The presence of an important population of red spirals, whose colors are basically identical to those of earlier types while keeping their late morphology, suggests that it can be an intermediate population before the galaxies are transformed into S0s. In this case, color changes seem to occur before morphological transformations, in agreement with McIntosh et al. (2004). Furthermore, the abundance of red late-types suggests that either high-z clusters are quite efficient and fast at quenching star formation, or dust obscuration is important at these redshifts [e. g., Haines et al. (2009), Finn et al. (2010), Vulcani et al. (2023a)].

Secondly, we can look at the SF fractions at the two redshifts, for different morphological types (see Table 7.2). The SF fraction diminishes by 30% from high- to low-z, for all galaxy types taken together. Analyzed separately, S0s and early spirals are the morphological types with the largest changes. When the SF fraction is inspected as a function of clustercentric distance (Figure 7.6), we do observe that EDisCS galaxies are more likely than WINGS ones to be SF and, although the SF population at high-z plummets within 1 R_{200}, it is still significantly higher (~ 43%) than at low-z (~ 22%). Our results are in very good agreement with Pintos-Castro et al. (2019), who studied quenching as a function of distance. They also suggest that close to the cluster center, both mass and environment quenching play a role, that they are not separable, and that an initial population of galaxies may be formed "in situ", in the cluster core.

Along the same lines, Moretti et al. (2022) observed galaxies in two clusters at $0.3 < z < 0.4$, to study the effect of RP at intermediate-z. This study reveals spectacular long tails of ionized gas in galaxies located in the inner regions of the clusters, which

led the authors to conclude that RPS is much more effective at this redshift than in the local universe. Their results would naturally explain why the SF fraction (Figure 7.6) of EDisCS galaxies drops rapidly towards the cluster core.

Even with the small number of objects in the EDisCS sample, this result indicates that the well-known Butcher–Oemler effect may originate from a higher fraction of SF galaxies, with larger SFR, at high-z. When these (spiral, in particular) galaxies are accreted onto a cluster, their star formation activity is definitely affected, mostly in the innermost cluster regions.

Another important difference between local and high-z clusters is the observed dependence of the SF fraction on cluster mass (parameterized by σ_{cl}). While a very weak dependence is found at low-z, in the cluster mass range probed by the EDisCS survey the SF fraction changes by a factor of two. Interestingly, this result seems to imply that, at high-z, the massive cluster environment is very effective in halting star formation, while less massive clusters (and groups) allow galaxies to form stars. This seems to be in contradiction with the Butcher–Oemler effect, i. e., the finding that high-z clusters are much richer in blue, SF spirals than local ones. This apparent inconsistency can be explained if we consider that field galaxies were more SF at earlier epochs than in the local universe. As they constitute a significant fraction of the accreted population, they are likely responsible for the richness of SF galaxies in high-z clusters even if, eventually, they will be quenched, similarly to what happens in local clusters, or even with greater efficiency.

9

SUMMARY AND CONCLUSIONS

9.1 SUMMARY

The build-up of the bulk of the baryonic mass in galaxies is known to have been driven by physical processes that depend on, at least, two intrinsic characteristics: their (final) total stellar mass and their morphology. Yet, at the same time, both morphology and the recent SFH of galaxies are known to be strongly dependent on the environment they inhabit. Among the long-known observational evidence of the effects of a dense environment on the properties of galaxies are the so-called morphology–density relation, and the fact that quenched galaxies dominate the populations of local clusters. The processes leading to these observed characteristics are still a matter of investigation.

We have implemented an in-depth analysis of the stellar population properties. To this end, we have used the WINGS/OmegaWINGS dataset of galaxies with spatially resolved data, taking a mass-limited sample ($\mathcal{M}_* > 3.0 \times 10^9$ $M_\odot$) of cluster and field (non-cluster member) galaxies in the local universe ($0.03 < z < 0.09$). We have leveraged galaxy properties, such as B and V photometry, redshift, cluster membership, morphology, and LD, as well as cluster properties like velocity dispersion and X-ray luminosity. We have used the spectrophotometric, non-parametric, code SINOPSIS, to derive fundamental properties of the stellar populations, such as stellar mass, SFRs, stellar ages, and SFHs.

Concerning SFHs, we have defined "quenching indices", $S_{i,j}$, as the ratio between the SFR in the two different age bins i and j. The quenching indices are effective in the detection of possible effects of the environment on the ability of a galaxy to form stars. We addressed the issue of the interaction between internal and external mechanisms and tried to include possible effects of variations in the large-scale environment. We have mostly focused on investigating possible interdependencies between the SFH, and both the local and large-scale environments. Through all this work, we control for and fix the two most important properties of galaxies: the stellar mass and the morphology, to quantify quenching by the sole environment.

We have also taken into account other mechanisms that affect stellar properties: RP, stellar bars, and major cluster mergers. For RP, we used data from the GASP sample, previously selected from the WINGS+OmegaWINGS catalog through particular features that characterize jellyfish galaxies. We analyzed the effects of RP on

this selected group, in comparison with the full WINGS+OmegaWINGS galaxy sample defined before, by studying the MS and the SFR-mass relation at different ages. The bar investigation was performed with the OmegaWINGS dataset; this time, we analyzed the fraction of barred galaxies as a function of color and stellar mass and morphology, as well as the influence of a bar on the SFR. Regarding cluster mergers, we compared two subsamples of clusters from the WINGS survey, one post-merger and one relaxed, utilizing morphological fractions and quenching indices.

Finally, we performed a comparison of our main results in the local universe with a cluster sample at intermediate-high redshift ($0.4 < z < 1.0$), taken from the EDisCS dataset. This time, we limited the galaxy samples in both datasets to objects with $\mathcal{M}_* > 1.0 \times 10^{10}\ \mathrm{M}_\odot$.

9.2 CONCLUSIONS AT LOW REDSHIFT

The main results of this work at low redshift can be summarized as follows:

1. At fixed stellar mass and morphology, the SFHs of cluster galaxies are steeper than those of field galaxies, indicating higher quenching efficiencies due to external agents. However, some mechanisms acting preferably in clusters, such as RP or hydrodynamical interactions with nearby late-type galaxies, can instead enhance star formation in recently acquired galaxies.

2. When studying the properties of stellar populations, and in particular the SFHs of cluster galaxies, morphology needs to be taken into account. The mode of star formation depends on the time spent within the cluster (on average, longer for early types and shorter for late types), and can, in turn, be roughly parameterized by morphology. Neglecting this property might lead to underestimating other mechanisms at play, such as preprocessing, close neighbor interactions, or RP.

3. At low values of LD, the distance and morphology of the closest neighbor can influence the properties of the current star formation activity. In a high LD environment, though, we cannot rule out a possible influence, as the presence of multiple nearby galaxies could play a role.

4. Quenching measured by the $S_{3,2}$ index on the recently accreted galaxy population (mainly spiral galaxies) is possibly stronger in more massive clusters (i.e., those with a higher velocity dispersion; see Figure 5.13), but this may instead be the result of combined local effects (see Figure 5.5 and Figure 5.11).

5. A study of the influence of cluster environment on star-formation activity limited to assessing the fraction of passive galaxies, based on the

presence/absence of emission lines, is bound to show only a partial picture, as star formation episodes in clusters can be both rapidly induced and quickly suppressed. A more complete portrayal arises by quantifying the star-formation activity still present in the fraction of active galaxies, and by looking at the full SFHs.

6. We find evidence that RP can enhance the SFR during the first interaction with the cluster, and hence accelerate galaxy quenching. This mechanism is more efficient close to the cluster center. Furthermore, even using fiber spectra, we obtained significant differences between RP-affected galaxies and the full cluster galaxy sample.

7. Stellar bars are more common in massive galaxies with later types, located in the cluster outskirts. Previous studies suggest that the bar can feed the innermost parts of a galaxy with gas. This supports our findings that stellar bars boost the SFR and slow down the quenching of star formation.

8. Cluster mergers seem to promote the quenching of spirals, something that is suggested by a comparison with clusters that appear relaxed at the time of the collision. An important caveat is that the statistics are poor and, we acknowledge, the signals of this effect are hints, at most. This is, however, more evident at epochs earlier than those sampled by emission lines, indicating a lack of dependence of the recent SFR on the dynamical state of the cluster.

We do find that cluster environment affects the ability of a galaxy to form stars, independently of morphological type. In an attempt to disentangle the environmental mechanisms, we tried to isolate the local interactions from the global effects of the cluster on galaxies. To shine more light on the issue, we have analyzed whether the morphology of the closest (massive) neighbor may affect the properties of a given galaxy. We find that, indeed, very close late-type neighbors promote star formation, while very close early-type neighbors can quench it. The cumulative effects of repeated encounters with early types, more frequent in the innermost cluster regions, will ultimately result in the shutting down of star formation. This result provides an observational context to the theoretical work of Hwang et al. (2018).

As for hydrodynamical phenomena, we find that RP may be the most efficient mechanism to strip galaxies of their gas. Galaxies can see their SFRs enhanced for a brief time while the gas compression happens, to subsequently have their star formation activity rapidly stopped. More massive clusters may have a slightly higher impact on the quenching. However, jellyfish galaxies with large tails are present even in low-mass clusters. One example is the jellyfish galaxy JO206 [Poggianti et al. (2017)], in the low-mass ($\sigma_{cl} \sim 500$ km s^{-1}) cluster IIZW108; the galaxy's tails extend for 90 kpc. RP, which can both increase and decrease star formation temporarily, also seems to be

stronger in merging clusters (Kelkar et al., submitted). Thus, signs of the relaxation state of a cluster should also be taken into account.

Finally, we would like to stress that, particularly in cluster galaxies, the characterization of star formation only through emission lines may give a very myopic vision of the situation. The age range probed by this observable is, in fact, very short and sensitive to the presence of massive stars that quickly disappear. When conditions are met, such as those for galaxies in clusters, in which large amounts of gas are stripped, and replenishing is prevented, star formation activity becomes an erratic event. In this thesis, we have demonstrated that clusters are home to physical mechanisms, such as RP and binary galaxy interactions, that can both enhance and suppress star formation on short timescales. Ultimately, their prolonged action, together with other typical mechanisms exclusive of clusters, will lead to the termination of the star formation activity.

9.3 CONCLUSIONS AT HIGH REDSHIFT

The main results obtained from the comparison between low-z (WINGS/OmegaWINGS) and high-z (EDisCS) galaxies are the following:

1. We confirm the well-known morphological galaxy evolution. Spirals are converted into S0s, which are more abundant in the local universe than at high-z (Table 7.1). On the other hand, the elliptical fraction is almost constant through cosmic time.

2. The sSFR-mass relation of high-z galaxies lies above its low-z counterpart (Figure 7.8). The fraction of SF galaxies is much larger at high-z, for all morphologies (Table 7.2), as well as SFRs at the ages 1, 2, and 3 (Figure 7.9).

3. At high-z, galaxies exhibit both higher SFRs and bluer colors than at low-z. When galaxies fall into a denser environment, like clusters, they lose their gas reservoir through different mechanisms, and become quenched and redder, as we see in local cluster galaxies.

4. Low-mass clusters are much less efficient at high-z than locally at turning-off star formation (Figure 7.7). Conversely, high-mass clusters are almost equally able, at high- and low-z, to quench galaxies.

These results bear to the Butcher-Oemler effect, whereby high-z clusters have galaxies that are bluer, more gas-rich, more SF, with higher SFRs, and a larger spiral fraction. Internal and external evolution convert galaxies into what we see today: redder, quenched, without gas, grouping into clusters, which are reaching a dynamical equilibrium.

9.4 FUTURE WORK

We believe that the present study has produced quite interesting new results on the mechanisms that affect galaxy evolution in clusters, at the same time highlighting the need to carefully and simultaneously take into account morphology, stellar mass, and environment. However, it has also exposed the limitations of the data we have used, as we discuss below. Several intriguing issues are worth studying in deeper detail, and there is room for substantial advances, regarding both the data and the analysis. Some points worth improvement are:

- ❏ It would be very useful to follow up fiber spectroscopy surveys with new ones, using integral field spectroscopy [similarly to the way the Mapping Nearby Galaxies at the Apache Point Observatory (MaNGA) survey is a natural extension of the SDSS]. This would allow not just the study of the properties of the whole galaxies, but also the detection of spatial signatures of interactions.

- ❏ A targeted IFU survey of rejuvenated early-type galaxies would help to better understand close interactions with gas-rich disk galaxies, as well as the timescales involved and the revival efficiency.

- ❏ In the next few years, more complete spectroscopy surveys of cluster galaxies will come to light, such as the WEAVE Wide-Field Cluster Survey (WWFCS; Kuchner et al., in prep.) for 20 local ($z \sim 0.05$) clusters up to 5 R_{200}. These new data will allow the study not only of galaxies as a whole but also of their stellar and gas dynamics, further helping to disentangle the different mechanisms at play.

- ❏ Moretti et al. (2022) studied two clusters at intermediate redshifts ($0.3 < z < 0.4$) and found that RP is still more efficient at this redshift range than in local clusters. Although we managed to compare low with intermediate-high redshifts, a similar investigation at intermediate ($0.1 < z < 0.3$) and higher redshifts ($z > 1.0$) is still missing.

- ❏ We compared the quenching effects and S0/spiral fractions of both post-merger and relaxed clusters. However, a similar investigation should be implemented with a larger cluster sample. A work approaching this problem, to which this thesis is contributing, is being carried out by Kelkar et al. (submitted).

- ❏ Include the influence of stellar bars on quenching/enhancing star formation through cosmic time.

- ❏ Taking into account galaxy membership in substructures when studying stellar population properties could provide new interesting insights about the roles

of LD and pre-processing. The same is for observing whether the scatter in the relation between LD and clustercentric distance depends on the number of substructures. Biviano et al. (2017) have already identified substructures for most of the WINGS/OmegaWINGS clusters.

- ❏ A field galaxy sample at intermediate-high redshift is still missing and should be gathered.

- ❏ Strengthen phase space analysis using regions from, e. g., Rhee et al. (2017), Pasquali et al. (2019), to constrain infall times of satellite galaxies of different morphological types.

- ❏ A comparison of our results with cosmological simulations, such as the IllustrisTNG project [Weinberger et al. (2017), Pillepich et al. (2018)], could be enlightening. TNG300 provides clusters, while TNG100 contains groups and galaxies with a higher spatial resolution. It should be possible to simulate SFHs with a high temporal resolution, in different environments.

Building on these points, a more complete analysis may be achieved with the ongoing observations from the Javalambre Physics of the Accelerating Universe Astrophysical Survey [J-PASS; Benitez et al. (2014)]. Using the dedicated 2.5 m telescope in the Observatorio Astrofísico de Javalambre, Spain, this survey will map about $1/5$ of the whole sky in 56 optical narrow-band filters, each with a width of ~ 145 Å and spaced by 100 Å, within the $\lambda \sim 3,500 - 10,000$ Å range and with a large field-of-view (4.2 $\deg^2$) camera. This new dataset will comprise a huge amount of objects, including spatially-resolved stellar populations of nearby galaxies and a large number of galaxy clusters and groups. It will boost the number of confirmed cluster members, and reach lower luminosities and hence stellar masses, and greatly improve the statistics of observed clusters and galaxies.

Finally, combined data from new facilities/instruments will further investigations on the topic of galaxy evolution. For instance, the study conducted by Vulcani et al. (2023a) of the intermediate-z cluster A2744, using VLT/MUSE observations together with new imaging data from the James Webb Space Telescope (JWST), led to the finding of a population of cluster and field galaxies with a red color excess. Thus, observations in different wavelengths will create synergies and shed light on different issues and conundrums in extragalactic astrophysics.

9.5 PUBLICATIONS

Most results of this thesis have been published or are in progress to be published:

- Chapter 4, Chapter 5, and Chapter 8 as Pérez-Millán et al. (2023).
- Section 6.1 as Fritz et al. (in prep.).
- Section 6.2 as Tawfeek et al. (2022).
- Section 6.3 as Kelkar et al. (submitted).
- The work in Chapter 7 is to be completed and published as Pérez-Millán et al. (in prep.).

Part V

APPENDIX

A

WINGS CLUSTERS

Some basic properties of the WINGS cluster sample defined in Section 2.1 are listed in Table A.1. Mean redshift (z) and velocity dispersion (σ_{cl}) were obtained from the data themselves [Biviano et al. (2017), Gullieuszik et al. (2020)], virial radius (R_{200}), and X-ray luminosity (L_X) taken from the ROSAT All-Sky Survey [Ebeling et al. (1996), Ebeling et al. (1998), Ebeling et al. (2000)].

Table A.1: Properties of the WINGS/OmegaWINGS cluster sample: redshift (z), number of confirmed cluster members, velocity dispersion (σ_{cl} in km s^{-1}), virial radius (R_{200} in Mpc), and X-ray luminosity (L_X in erg s^{-1}). WINGS and OmegaWINGS columns indicate if the cluster was observed in spectroscopy. The last column shows whether WINGS/OmegaWINGS spectra have sufficient signal-to-noise ratio to run the SINOPSIS code.

Cluster	z	N_m	σ_{cl}	R_{200}	$\log_{10} L_X$	WINGS	OmegaW	SINOPSIS
A1069	0.06528	180	542^{+38}_{-36}	1.180	43.98	✓	✓	✓
A119	0.04436	155	952^{+46}_{-49}	2.250	44.51	✓	–	✓
A1291	0.05090		413	0.860	43.64	✓	–	–
A133	0.06030		623	1.292	44.55	–	–	–
A147	0.04470		387	0.808	43.73	–	–	–
A151	0.05327	235	771^{+37}_{-39}	1.670	44.00	✓	✓	✓
A160	0.04317		738^{+59}_{-55}	1.600	43.58	✓	–	–
A1631a	0.04644	353	715^{+35}_{-36}	1.390	43.86	✓	✓	✓
A1644	0.04691	164	945^{+46}_{-48}	1.890	44.55	✓	–	✓
A1668	0.06340		654	1.354	44.20	–	–	–
A168	0.04518	134	498^{+29}_{-28}	0.970	44.04	–	✓	✓
A1736	0.04610		918	1.916	44.37	–	–	–
A1795	0.06291	29	731^{+38}_{-36}	1.720	45.05	✓	–	–
A1831	0.06340		444	0.919	44.28	✓	–	–
A193	0.04852	67	758^{+48}_{-45}	1.580	44.19	–	✓	✓
A1983	0.04517	31	407^{+25}_{-23}	0.950	44.67	✓	–	–

Continued on next page.

Table A.1 – *Continued from previous page.*

Cluster	z	N_m	σ_{cl}	R_{200}	$\log_{10} L_X$	WINGS	OmegaW	SINOPSIS
A1991	0.05860		570^{+38}_{-36}	1.330	44.13	✓	–	–
A2107	0.04166		519^{+32}_{-30}	1.150	44.04	✓	–	–
A2124	0.06692		733^{+45}_{-43}	1.090	44.13	✓	–	–
A2149	0.06750		459	0.948	43.92	–	–	–
A2169	0.05780		524	1.088	43.65	✓	–	–
A2256	0.05810		1376	2.856	44.85	–	–	–
A2271	0.05840		460	0.955	43.81	–	–	–
A2382	0.06442	378	807^{+39}_{-41}	1.730	43.96	✓	✓	✓
A2399	0.05793	274	662^{+32}_{-34}	1.550	44.00	✓	✓	✓
A2415	0.05791	191	683^{+43}_{-41}	1.190	44.23	✓	✓	✓
A2457	0.05889	243	605^{+39}_{-31}	1.310	44.16	✓	✓	✓
A2572a	0.03900		546	1.144	44.01	✓	–	✓
A2589	0.04217		1147^{+70}_{-66}	2.750	44.27	✓	–	–
A2593	0.04188		523^{+27}_{-26}	1.210	44.06	✓	–	–
A2622	0.06100		732	1.517	44.03	✓	–	–
A2626	0.05509	27	650^{+53}_{-49}	1.480	44.29	✓	–	✓
A2657	0.04000		829	1.735	44.2	–	–	–
A2665	0.05620		–	–	–	–	–	–
A2717	0.04989	130	470^{+27}_{-26}	1.170	44.00	–	✓	✓
A2734	0.06147	215	588^{+28}_{-30}	1.380	44.41	–	✓	✓
A311	0.06570		–	–	–	–	–	–
A3128	0.06033	462	793^{+38}_{-40}	1.580	44.33	✓	✓	✓
A3158	0.05947	417	948^{+46}_{-48}	1.940	44.73	✓	✓	✓
A3164	0.06110		991	2.054	–	–	–	–
A3266	0.05915	643	1095^{+53}_{-56}	2.310	44.79	✓	✓	✓
A3376	0.04652	250	756^{+37}_{-39}	1.650	44.39	✓	✓	✓
A3395	0.05103	339	1272^{+62}_{-65}	2.760	44.45	✓	✓	✓
A3490	0.06880	68	660	1.363	44.24	✓	–	✓
A3497	0.06800	74	724	1.496	44.16	✓	–	✓
A3528a	0.05441	251	891^{+43}_{-45}	1.880	44.12	–	✓	✓
A3528b	0.05350		–	–	44.30	–	–	–

Continued on next page.

Table A.1 – *Continued from previous page.*

Cluster	z	N_m	σ_{cl}	R_{200}	$\log_{10} L_X$	WINGS	OmegaW	SINOPSIS
A3530	0.05480	262	674	1.401	43.94	–	✓	✓
A3532	0.05536	89	662^{+32}_{-34}	1.550	44.45	–	✓	✓
A3556	0.04796	346	531^{+26}_{-27}	1.100	43.97	✓	✓	✓
A3558	0.04829	394	910^{+44}_{-46}	1.950	44.80	–	✓	✓
A3560	0.04917	275	799^{+39}_{-41}	1.790	44.12	✓	✓	✓
A3667	0.05528	365	1031^{+50}_{-53}	2.220	44.94	–	✓	✓
A3716	0.04599	312	753^{+36}_{-38}	1.720	44.00	–	✓	✓
A376	0.04752	43	832^{+56}_{-52}	1.660	44.14	✓	–	✓
A3809	0.06245	223	499^{+24}_{-25}	1.040	44.35	✓	✓	✓
A3880	0.05794	212	514^{+27}_{-25}	1.200	44.27	–	✓	✓
A4059	0.04877	247	744^{+36}_{-38}	1.580	44.49	–	✓	✓
A500	0.06802	220	660^{+34}_{-33}	1.800	44.15	✓	✓	✓
A548b	0.04410		842	1.759	43.48	–	–	–
A602	0.06210		834	1.728	44.05	–	–	–
A671	0.04939		730^{+49}_{-46}	1.490	43.95	✓	–	–
A754	0.05445	319	816^{+39}_{-42}	1.660	44.90	✓	✓	✓
A780	0.05650		–	–	44.82	–	–	–
A85	0.05568	165	859^{+42}_{-44}	2.020	44.92	–	✓	✓
A957x	0.04496	77	631^{+43}_{-40}	1.420	43.89	✓	✓	✓
A970	0.05872	213	749^{+44}_{-42}	1.630	44.18	✓	✓	✓
IIZW108	0.04889	144	575^{+33}_{-31}	1.199	44.34	✓	✓	✓
MKW3s	0.04470		604^{+38}_{-36}	1.580	44.43	✓	–	–
Rx0058	0.04840		696	1.451	43.64	✓	–	✓
Rx1022	0.05480		582	1.210	43.54	✓	–	–
Rx1740	0.04410		540	1.128	43.7	✓	–	–
Z1261	0.06440		–	–	–	–	–	–
Z2844	0.05027		425^{+34}_{-31}	0.880	43.76	✓	–	–
Z8338	0.04953	37	658^{+50}_{-46}	1.350	43.9	✓	–	✓
Z8852	0.04077	25	786^{+65}_{-60}	1.630	43.97	✓	–	✓

B

EDISCS CLUSTERS

Some basic properties of the EDisCS groups and clusters. Following to Rudnick et al. (2017), clusters are defined for having velocity dispersion $\sigma_{cl} > 400$ km s^{-1}, while groups with at least eight spectroscopic members and $160 < \sigma \leqslant 400$ km s^{-1}. Velocity dispersion values were calculated using the full EDisCS member sample, which is larger than the number of galaxies used for the analysis in this work.

Table B.1: Properties of the EDisCS cluster sample: redshift (z) taken from White et al. (2005), Rudnick et al. (2017), number of confirmed cluster members, velocity dispersion (σ_{cl} in km s^{-1}) [Desai et al. (2007), Rudnick et al. (2017)], virial radius (R_{200} in Mpc) [Desai et al. (2007), Barsanti et al. (2016)], and X-ray luminosity (L_X in erg s^{-1}) [Johnson et al. (2006)]. The last column shows if we have available spectra and they were run with the SINOPSIS code.

Cl/Group	Name	z	σ_{cl}	R_{200}	$\log_{10} L_X$	SINOPSIS
Cl	1018.8-1211	0.4734	486^{+59}_{-63}			–
Cl	1037.9-1243	0.4252	537			–
Gr	1037.9-1243	0.5783	319^{+53}_{-52}	0.57		✓
Cl	1040.7-1155	0.7043	418^{+55}_{-46}	0.7		✓
Gr	1040.7-1155a	0.6316	179^{+40}_{-26}			–
Gr	1040.7-1155b	0.7798	259^{+91}_{-52}			–
Cl	1054.4-1146	0.6972	589^{+78}_{-70}	0.99	44.163	✓
Gr	1054.4-1146a	0.613	227^{+72}_{-28}			–
Cl	1054.7-1245	0.7498	504^{+113}_{-65}	0.82		✓
Gr	1054.7-1245a	0.7305	182^{+58}_{-69}			–
Cl	1059.2-1253	0.4564	510^{+52}_{-56}	0.87		–
Cl	1103.7-1245	0.9586	534	0.42		✓
Gr	1103.7-1245a	0.6261	336	0.60		–
Gr	1103.7-1245b	0.7031	252			–
Gr	1119.3-1129	0.55	166			–
Cl	1138.2-1133	0.4796	732^{+72}_{-76}	1.4		✓

Continued on next page.

Table B.1 – *Continued from previous page.*

Cl/Group	Name	z	σ_{cl}	R_{200}	$\log_{10} L_X$	SINOPSIS
Cl	1138.2-1133a	0.4548	542^{+63}_{-71}	0.85		–
Cl	1202.7-1224	0.4240	518^{+92}_{-104}			–
Cl	1216.8-1201	0.7943	1018^{+73}_{-77}	1.61	44.387	✓
Cl	1227.9-1138	0.6357	574^{+72}_{-75}	1.0		✓
Gr	1227.9-1138a	0.5826	341^{+341}_{-46}			–
Cl	1232.5-1250	0.5414	1080^{+119}_{-89}	1.99		✓
Cl	1238.5-1144	0.4062	447			–
Cl	1301.7-1139	0.4828	687^{+81}_{-86}	1.14		–
Gr	1301.7-1139a	0.3969	391^{+63}_{-69}	0.67		–
Cl	1353.0-1137	0.5882	666^{+136}_{-139}	0.92		–
Cl	1354.2-1230	0.7620	648^{+105}_{-110}	1.05		✓
Cl	1354.2-1230a	0.5952	433^{+95}_{-104}			–
Cl	1411.1-1148	0.5195	710^{+125}_{-133}	1.26		–
Gr	1420.3-1236	0.4962	218^{+43}_{-50}			–

C

BOOTSTRAPPING

The bootstrapping technique is a statistical method used to estimate a sampling distribution by resampling the data. It is useful when it is difficult or impossible to obtain an expression for the sampling distribution. Traditional statistical inference often involves making assumptions about the underlying distribution of the population and using those assumptions to calculate the sampling distribution of a statistic. Nevertheless, in many real-world scenarios, the distribution of the population is unknown or too complex to model accurately. Here is where bootstrapping comes into play.

The term "bootstrapping" was coined by Efron (1979). This statistical tool is very powerful and widely used to quantify the uncertainty associated with an estimator in particular. Bootstrapping involves drawing repeated samples with replacements from the observed data to create a large number of resamples. Each replicate sample has the same size as the original dataset. Some resamples will be represented multiple times in the bootstrap sample, while others will not be selected at all.

By repeating this process multiple times, one can obtain a distribution of the resamples, called the bootstrap distribution, which represents an approximation of the sampling distribution's statistics. Thus properties, such as the standard error and the confidence intervals, can be derived from the bootstrap distribution. No specific assumptions about the distribution of the underlying population are needed.

We can summarize this procedure as follows:

1. Choose the parent sample.
2. Choose the number of bootstrap subsamples to select. We use N = 1,000.
3. Draw N subsamples with replacement.
4. Calculate the statistic (standard deviation) of each subsample.
5. Calculate the average of the 1,000 standard deviations.
6. The average obtained will be the error applied to the parent sample.

In this work, we use the method of bootstrapping to obtain the uncertainties applied to the mean SFRs and mean quenching indices. The error bars represent the 68% confidence interval drawn from 1,000 random realizations of the original sample. The minimum weighted number of galaxies used in each bin is 30 (around 20 objects), unless otherwise specified.

BIBLIOGRAPHY

Aguerri J. A. L., González-García A. C., 2009, A&A, **494**, 891.

Athanassoula E. & Bureau M., 1999, ApJ, **522**, 699.

Athanassoula E., Lambert J. C., Dehnen W., 2005, MNRAS, **363**, 496.

Athanassoula E., 2013, Secular Evolution of Galaxies, ed. J. Falcón-Barroso & J. H. Knapen, Cambridge Univ. Press, 305.

Baldry I. K., Glazebrook K., Brinkmann J., Ivezić v. et al., 2004, ApJ, **600**, 681.

Baldwin J. A., Phillips M. M., Terlevich R., 1981, PASP, **93**, 5.

Balogh M. L., Baldry I. K., Nichol R., Miller C. et al., 2004, ApJL, **615**, L101.

Bamford S. P., Nichol R. C., Baldry I. K., Land K. et al., 2009, MNRAS, **393**, 1324.

Baraffe I., Chabrier G., Allard F., Hauschildt P. H., 1998, A&A, **337**, 403.

Barazza F. D., Jogee S., Marinova I., 2008, ApJ, **675**, 1194.

Barazza F. D., Jablonka P., Desai V., Jogee S. et al., 2009, A&A, **497**, 713.

Barsanti S., Girardi M., Biviano A., Borgani S. et al., 2016, A&A, **595**, A73.

Barsanti S., Owers M. S., Brough S., Davies L. J. M. et al., 2018, ApJ, **857**, 71.

Baugh C. M., Cole S., Frenk C. S., 1996, MNRAS, **283**, 1361.

Beers T. C, Flynn K., Marmo C., Gebhardt K., 1990, AJ, **100**, 32.

Bender R., Kormendy J., Cornell M. E. & Fisher D. B., 2015, ApJ, **807**, 56.

Benitez N., Dupke R., Moles M., Sodre L. et al., 2014, arXiv e-prints, arXiv:1403.5237.

Bernardi M., Shankar F., Hyde J. B., Mei S. et al., 2010, MNRAS, **404**, 2087.

Berta S., Rubele S., Franceschini A., Held E. V. et al., 2006, A&A, **451**, 881.

Bertin E. & Arnouts S., 1996, AAPS, **117**, 393.

Binney J. & Tremaine S., 1987, Galactic dynamics, Princeton University Press.

Biviano A., Moretti A., Paccagnella A., Poggianti B. M. et al., 2017, AAP, **607**, A81.

Blanton M. R., Hogg D. W., Bahcall N. A., Brinkmann J. et al., 2003, ApJ, **592**, 819.

Bonoli S., Marín-Franch A., Varela J., Vázquez Ramió H. et al., 2021, A&A, **653**, A31.

Boselli A. & Gavazzi G., 2006, ApJ, **118**, 517.

Botteon A., Gastaldello F., Brunetti G., 2018, MNRAS, **476**, 5591.

Bournaud F. & Combes F., 2002, A&A, **392**, 83.

Brambila D., Lopes P. A. A., Ribeiro A. L. B., Cortesi A., 2023, MNRAS, **523**, 785.

Brinchmann J., Charlot S., White S. D. M., Tremonti C. et al., 2004, MNRAS, **351**, 1151.

Brodwin M., Greer C. H., Leitch E. M., Stanford S. A. et al., 2015, ApJ, **806**, 26.

Bruzual G. & Charlot S., 2003, MNRAS, **344**, 1000.

Burrows A., 2000, Natur, **403**, 727.

Butcher H., and Oemler A. Jr., 1978, ApJ, **226**, 559.

Butcher H., and Oemler A. Jr., 1984, ApJ, **285**, 426.

Byrd G. & Valtonen M., 1990, ApJ, **350**, 89.

Calvi R., Poggianti B. M., Vulcani B., 2011, MNRAS, **416**, 727.

Calvi R., Poggianti B., Fasano G., Vulcani B. et al., 2012, MNRAS, **432**, L14.

Calvi R., Poggianti B., Vulcani B., Fasano G. et al., 2013, MNRAS, **432**, 3141.

Calvi R., Vulcani B., Poggianti B. M, Moretti A. et al., 2018, MNRAS, **481**, 3456.

Calzetti D., Kinney A. L., Storchi-Bergmann T., 1994, ApJ, **429**, 582.

Cantale N., Jablonka P., Muzzin A., Courbin F., Rudnick G., et al., 2016, A&A, **589**, A82.

Cao C., Xu C. K., Domingue D., Buat V. et al., 2016, ApJS, **222**, 16.

Cardelli J. A., Clayton G. C., Mathis J. S., 1989, ApJ, **345**, 245.

Casado J., Ascasibar Y., Gavilán M., Terlevich R. et al., 2015, MNRAS, **451**, 888.

Cava A., Bettoni D., Poggianti B., Couch W. et al., 2009, A&A, **495**, 707.

Cava A., Biviano A., Mamon G. A., Varela J. et al., 2017, A&A, **606**, L108.

Cavanagh M. K. & Bekki K., 2020, A&A, **641**, A77.

Cerulo P., Couch W. J, Lidman C., Demarco R., et al., 2016, MNRAS, **457**, 2209.

Cervantes Sodi B., Li Cheng, Park C., Wang L., 2013, ApJ, **775**, 19.

Cervantes Sodi B., 2017, ApJ, **835**, 80.

Chabrier G., 2003, PASP, **115**, 763.

Chang Y.-Y., van der Wel A., da Cunha E., Rix H.-W., 2015, ApJS, **219**, 8.

Chapelon S., Contini T., Davoust E., 1999, A&A, **345**, 81.

Charlot S., Fall S. M., 2000, ApJ, **539**, 718.

Chen Y. M., 2009, American Institute of Physics, Conference Series Vol. 1201, AIPC, pp 45–48.

Chen Y., Bressan A., Girardi L., Marigo P. et al., 2015, MNRAS, **452**, 1068.

Cid Fernandes R., Pérez E., García B., González D. et al., 2013, A&A, **557**, A86.

Colberg J. M., Krughoff K. S., Connolly A. J., 2005, MNRAS, **359**, 272.

Conselice C. J., 2006, MNRAS, **373**, 1389.

Contini E., Gu Q., Kang X., Rhee J., Yi S. K. et al., 2019, ApJ, **882**, 167.

Contreras-Santos A., Knebe A., Pearce F., Haggar R. et al., 2022, MNRAS, **511**, 2897.

Cowie L. L. & Songaila A., 1977, Natur, **266**, 501.

Cowie L. L., Songaila A., Hu E. M., Cohen J. G. et al., 1996, AJ, **112**, 839.

Cybulski R., Yun M. S., Fazio G. G., Gutermuth R. A., 2014, MNRAS, **439**, 3564.

D'Onofrio M., Grado A., Bettoni D., Fritz J. et al., 2020, A&A, **637**, A54.

Debattista V. P. & Sellwood J. A., 2000, ApJ, **543**, 704.

Desai V., Dalcanton J. J., Aragón-Salamanca A., Jablonka P. et al., 2007, ApJ, **660**, 1151.

Di Matteo P., Qu Y., Lehnert M. D., van Driel W. et al., 2010, EAS Pub. Ser., **45**, 389.

Dressler A., 1980, ApJ, **236**, 351.

Eales S., de Vis P., Smith M. W. L., Appah K. et al., 2017, MNRAS, **465**, 3125.

Eales S. A., Baes M., Bourne N., Bremer M. et al., 2018, MNRAS, **481**, 1183.

Ebeling H., Voges W., Bohringer H., Edge A. C. et al., 1996, MNRAS, **281**, 799.

Ebeling H., Edge A. C., Bohringer H., Allen S. W. et al., 1998, MNRAS, **301**, 881.

Ebeling H., Edge A. C., Allen S. W., Crawford C. S. et al., 2000, MNRAS, **318**, 333.

Ebeling H., Stephenson L. N., Edge A. C., 2014, ApJL, **781**, L40.

Efron B., 1979, Annals of Statistics, **7**, 1.

Eskridge P. B., Frogel J. A., Pogge R. W., Quillen A. C. et al., 2000, AJ, **119**, 536.

Fasano G., Poggianti B. M., Couch W., Bettoni D. et al., 2000, ApJ, **542**, 673.

Fasano G., Marmo C., Varela J., D'Onofrio M. et al., 2006, A&A, **445**, 805.

Fasano G., Vanzella E., Dressler A., Poggianti B. M. et al., 2012, MNRAS, **420**, 926.

Fasano G., Poggianti B. M., Bettoni D., D'Onofrio M. et al., 2015, MNRAS, **449**, 3927.

Ferland G. J, Porter R. L., van Hoof P. A. M, Williams R. J. R. et al., 2012, RMxAA, **49**, 137.

Finn R. A, Zaritsky D., McCarthy D. W., Poggianti B. M. et al., 2005, ApJ, **630**, 206.

Finn R. A., Desai V., Rudnick G., Poggianti B. et al., 2010, ApJ, **720**, 87.

Flower P. J., 1996, ApJ, **469**, 355.

Fraser-McKelvie A., Brown M. J. I., Pimbblet K., Dolley T. et al., 2018a, MNRAS, **474**, 1909.

Fraser-McKelvie A., Aragón-Salamanca A., Merrifield M., Tabor M. et al., 2018b, MNRAS, **481**, 5580.

Fritz J., Poggianti B. M., Bettoni D., Cava A. et al., 2007, A&A, **470**, 137.

Fritz J., Poggianti B. M., Cava A., Valentinuzzi T. et al., 2011, A&A, **526**, A45.

Fritz J., Poggianti B. M., Cava A., Moretti A. et al., 2014, A&A, **566**, A32.

Fritz J., Moretti A., Gullieuszik M., Poggianti B. M. et al., 2017, A&A, **848**, 132.

Fujita Y. & Nagashima M., 1999, ApJ, **516**, 619.

Fujita Y., 2004, PASJ, **56**, 29.

Fumagalli M., Fossati M., Hau G. K. T., Gavazzi G. et al., 2014, MNRAS, **445**, 4335·

Gallazzi A., Charlot S., Brinchmann J., White S. et al., 2005, MNRAS, **362**, 41.

García-Benito R., González D. R. M, Pérez E., Cid Fernandes R. et al., 2017, A&A, **608**, A27.

George K. & Subramanian S., 2021, A&A, **651**, A107.

Ghosh S., Saha K., Di Matteo P., Combes F., 2021, MNRAS, **502**, 3085.

Gómez P. L., Nichol R. C., Miller C. J., Balogh M. L. et al., 2003, ApJ, **584**, 210.

González Delgado R. M., Rodríguez-Martín J. E., Díaz-García L. A., de Amorim A. et al., 2022, A&A, **666**, A84.

Gonzalez A. H., Zaritsky D., Dalcanton J., Nelson A. et al., 2001, ApJS, **137**, 117.

Goto T., Okamura S., Yagi M., Sheth R. et al., 2003, PASJ, **55**, 739.

Goto T., Yagi M., Tanaka M., Okamura S., 2004, MNRAS, **348**, 515.

Guglielmo V., Poggianti B. M., Moretti A., Fritz J. et al., 2015, MNRAS, **450**, 2749.

Gullieuszik M., Poggianti B. M., Fasano G., Zaggia S. et al., 2015, A&A, **581**, A41.

Gullieuszik M., Poggianti B. M., Moretti A., Fritz J. et al., 2017, ApJ, **846**, 27.

Gullieuszik M., Poggianti B. M., McGee S. L, Moretti A. et al., 2020, ApJ, **899**, 13.

Gunn J. E. & Gott J., 1972, ApJ, **176**, 1.

Haines C. P., Smith G. P., Egami E., Ellis R. S. et al., 2009, ApJ, **704**, 126.

Halliday C., Milvang-Jensen B., Poirier S., Poggianti B. M. et al., 2004, A&A, **427**, 397.

Hawarden T. G., Huang J. H., Gu Q. S., 1996, ASP Conf. Ser., **345**, 54.

Hou A., Parker L. C., Harris W. E., Wilman D. J. et al., 2009, ApJ, **702**, 1199.

Houghton R. C. W., 2015, A&A, **451**, 3427.

Huang S., Gu Q. -S, 2009, MNRAS, **398**, 1651.

Hudson M., Stevenson J. B., Smith R. J., Wegner G. A., et al., 2010, MNRAS, **409**, 405.

Hwang J.-S, Park C., Banerjee A., Hwang H. S., 2018, ApJ, **856**, 160.

Jáchym P., Palouš J., Köppen J., Combes F., 2007, A&A, **472**, 5.

Jáchym P., Köppen J., Palouš J., Combes F., 2009, A&A, **500**, 693.

Jacoby G. H., Hunter D. A., Christian C. A., 1984, APJS, **56**, 257.

Jaffé Y. L., Smith R., Candlish G. N., Poggianti B. M. et al., 2015, MNRAS, **448**, 1715.

Johnson O., Best P., Zaritsky D., Clowe D. et al., 2006, MNRAS, **371**, 1777.

Kannappan S. J., Guie J. M., Baker A. J., 2009, AJ, **138**, 579.

Kapferer W., Sluka C., Schindler S., Ferrari C. et al., 2009, AAP, **499**, 87.

Karim A., Schinnerer E., Martínez-Sansigre A., Sargent M. T. et al., 2011, ApJ, **730**, 61.

Katsianis A., Tescari E., Wyithe J. S. B., 2016, PASA, **33**, e029.

Kauffmann G., Heckman T. M., White S. D. M, Charlot S. et al., 2003a, MNRAS, **341**, 33.

Kauffmann G., Heckman T. M., White S. D. M, Charlot S. et al., 2003b, MNRAS, **341**, 54.

Kauffmann G., White S. D. M, Heckman T. M., Ménard B. et al., 2004, MNRAS, **353**, 713.

Kaviraj S., 2014, MNRAS, **437**, L41.

Kelkar K., Dwarakanath K. S., Poggianti B. M., Moretti A. et al., 2020, MNRAS, **496**, 442.

Kelvin L. S., Driver S. P., Robotham A. S. G, Taylor E. N. et al., 2014, MNRAS, **444**, 1647.

Kennicutt R. C. Jr., 1989, ApJ, **344**, 685.

Kennicutt R. C. Jr., 1998, ARAA, **36**, 189.

Khostovan A. A., Sobral D., Mobasher B., Best P. N. et al., 2015, MNRAS, **452**, 3948.

Kim E., Hwang H. S., Chung H., Lee G.-H. et al., 2017, ApJ, **845**, 93.

Kormendy J. & Kennicutt R. C. Jr., 2004, ARA&A, **42**, 603.

Krogager J.-K., Fynbo J. P. U., Ledoux C., Christensen L. et al., 2013, MNRAS, **433**, 3091.

Kronberger T., Kapferer W., Ferrari C., Unterguggenberger S. et al., 2008, A&A, **481**, 337.

Kroupa P., 2001, MNRAS, **322**, 231.

Kuchner U., Haggar R., Aragón-Salamanca A., Pearce F. R. et al., 2022, MNRAS, **510**, 581.

Kurtz, M. J., Mink, D. J., Wyatt, W. F., et al. 1992, Astronomical Data Analysis Software and Systems I, **25**, 432

Laganá T. F. & Ulmer M. P, 2018, MNRAS, **475**, 523.

Lambas D. G., Alonso S., Mesa V., O'Mill A. L. et al., 2012, A&A, **539**, A45.

Lara-López M. A., Bongiovanni A., Cepa J., Pérez García A. M. et al., 2010, A&A, **519**, A31.

Larson R. B., Tinsley B. M., Caldwell C. N., 1980, ApJ, **237**, 692.

Lee G.-H., Park C., Lee M. G., Choi Y.-Y., 2012, ApJ, **745**, 125.

Lee Y. H., Ann H. B., Park M-G., 2019, ApJ, **872**, 97.

Lee J. H., Lee M. G., Mun J. Y., Cho B. S. et al., 2022, ApJL, **931**, L22.

Lee Y. H., Hwang H. S., Hwang N., Lee J. C. et al., 2023, ApJ, **953**, 88.

Lequeux J., Peimbert M., Rayo J. F., Serrano A., 1979, A&A, **80**, 155.

Leslie S. K., Schinnerer E., Liu D., Magnelli B. et al., 2020, ApJ, **899**, 58.

Lewis I., Balogh M., De Propris R., Couch W., et al., 2002, MNRAS, **334**, 673.

Li H., Ge J., Mao S., Cappellari M. et al., 2017, ApJ, **838**, 77.

Lin L., Li C., Du C., Wang E. et al., 2020, MNRAS, **499**, 1406.

Lindholmer M. O. & Pimbblet K. A., 2019, A&A, **629**, A7.

Liu C.-X., Pan D. C., Hao L., Hoyle F. et al., 2015, ApJ, **810**, 165.

Liu C.-X., Hao L., Wang H., Yang X., 2019, ApJ, **878**, 69.

Łokas E. L., 2018, ApJ, **857**, 6.

Longhetti M. & Saracco P., 2009, MNRAS, **394**, 774.

Lopes P. A. A., Trevisan M., Laganá T. F., Durret F. et al., 2018, MNRAS, **478**, 5473.

Madau P. & Dickinson M., 2014, ARA&A, **52**, 415.

Mahajan S., Mamon G. A., Raychaudhury S., 2011, MNRAS, **416**, 2882.

Makarov D., Prugniel P., Terekhova N., Courtois H. et al., 2014, A&A, **570**, A13.

Mamon G. A., Cava A., Biviano A., Moretti A. et al., 2019, MNRAS, **631**, A131.

Mann A. W. & Ebeling H., 2012, MNRAS, **420**, 2120.

Mannucci F., Cresci G., Maiolino R., Marconi A. et al., 2010, MNRAS, **408**, 2115.

Marchesini D., van Dokkum P., Förster Schreiber N., Franx M. et al., 2009, ApJ, **701**, 1765.

Margoniner V. E., de Carvalho R. R., Gal R. R., Djorgovski S. G., 2001, ApJL, **548**, L143.

Marigo P., Bressan A., Nanni A., Girardi L. et al., 2013, MNRAS, **434**, 488.

Martin D. C., Wyder T. K., Schiminovich D., Barlow T. A. et al., 2007, ApJS, **173**, 342.

Martínez H., Coenda V., Muriel H., 2010, MNRAS, **403**, 748.

Marziani P., D'Onofrio M., Bettoni D., Poggianti B. M. et al., 2017, A&A, **599**, A83.

Masters K., Nichol R., Bamford S., Mosleh M. et al., 2010, MNRAS, **404**, 792.

McGaugh S. S. & Schombert J. M., 2014, AJ, **148**, 77.

McGee S. L., Balogh M. L., Bower R. G., Font A. S. et al., 2009, MNRAS, **400**, 937.

McIntosh D., Rix H.-W., Caldwell N., 2004, ApJ, **610**, 161.

McPartland C., Ebeling H., Roediger E., Blumenthal K., 2016, MNRAS, **455**, 2994.

Mei S., Holden B. P., Blakeslee J. P., Ford H. C. et al., 2009, ApJ, **690**, 42.

Mendel J. T., Saglia R. P., Bender R., Beifiori A. et al., 2015, ApJL, **804**, L4.

Merluzzi P., Busarello G., Dopita M. A., Haines C. P. et al., 2013, MNRAS, **429**, 1747.

Mihos A., 2004, cgpc.symp, 277.

Miller C. J., Nichol R. C., Reichart D., Wechsler R. H. et al., 2005, AJ, **130**, 968.

Miller Bertolami M. M., 2016, A&A, **588**, A25.

Milvang-Jensen B., Noll S., Halliday C., Poggianti B. M. et al., 2008, A&A, **482**, 419.

Moore B., Katz N., Lake G., Dressler A. et al., 1996, Natur, **379**, 613.

Morell D. F., Ribeiro A. L. B., de Carvalho R. R., Rembold S. B. et al., 2020, MNRAS, **494**, 3317.

Moretti A., Poggianti B. M., Fasano G., Bettoni D. et al., 2014, A&A, **564**, A138.

Moretti A., Bettoni D., Poggianti B. M., Fasano G. et al., 2015, A&A, **581**, A11.

Moretti A., Gullieuszik M., Poggianti B. M., Paccagnella A. et al., 2017, A&A, **599**, A81.

Moretti A., Paladino R., Poggianti B., Serra P. et al., 2020, ApJ, **889**, 9.

Moretti A., Radovich M., Poggianti B. M., Vulcani B. et al., 2022, ApJ, **925**, 4.

Morgan W. W., 1958, PASP, **70**, 364.

Mori M. & Burkert A., 2000, ApJ, **538**, 559.

Moster B. P., Somerville R. S., Newman J. A., Rix H.-W., 2011, ApJ, **731**, 113.

Mukherjee S., Koopmans L. V. E., Tortora C., Schaller M. et al., 2022, MNRAS, **509**, 1245.

Muldrew S. I., Hatch N. A., Cooke E. A., 2015, MNRAS, **452**, 2528.

Nantais J. B., van der Burg R. F. J., Lidman C., Demarco R. et al., 2016, A&A, **592**, A161.

Neistein E., van den Bosch F. C., Dekel A., 2006, MNRAS, **372**, 933.

Noeske K. G., Faber S. M., Weiner B. J., Koo D. C. et al., 2007, ApJL, **660**, L47.

Noguchi M., 1987, MNRAS, **228**, 635.

Oman K. A., Hudson M. J., Behroozi P. S., 2013, MNRAS, **431**, 2307.

Oman K. A., Hudson M. J., 2016, MNRAS, **463**, 3083.

Omizzolo A., Fasano G., Reverte Paya D., De Santis C. et al., 2014, A&A, **561**, A111.

Paccagnella A., Vulcani B., Poggianti B. M., Moretti A. et al., 2016, ApJL, **816**, L25.

Pacifici C., Kassin S. A., Weiner B. J., Holden B. et al., 2016, ApJ, **832**, 79.

Pan H.-A, Lin L., Hsieh B.-C, Sánchez S. F. et al., 2018, ApJ, **854**, 159.

Pannella M., Elbaz D., Daddi E., Dickinson M. et al., 2015, ApJ, **807**, 141.

Park C. & Choi Y.-Y, 2009, ApJ, **691**, 1828.

Park C. & Hwang H. S., 2009, ApJ, **699**, 1595.

Pasquali A., Smith R., Gallazzi A., De Lucia G. et al., 2019, MNRAS, **484**, 1702.

Patton D., Wilson K., Kieran D., Metrow C. J. et al., 2020, MNRAS, **494**, 4969.

Pearson W. J., Wang L., Hurley P. D., Małek K. et al., 2018, A&A, **615**, A146.

Peebles P. J. E., 1993, Principles of Physical Cosmology, Princeton University Press.

Pelló R., Rudnick G., De Lucia G., Simard L. et al., 2009, A%A, **508**, 1173.

Peng Y.-j, Lilly S. J., Kovač K., Bolzonella M. et al., 2010, ApJ, **721**, 193.

Pérez-González P. G., Rieke G. H., Villar V., Barro G. et al., 2008, ApJ, **675**, 234.

Pérez-Hernández E., Kemp S. N., Ramirez-Siordia V. H., Nigoche-Netro A., 2022, MNRAS, **511**, 201.

Pérez-Millán D., Fritz J., González-Lópezlira R. A., Moretti A. et al., 2023, MNRAS, **521**, 1292.

Pfeffer J., Cavanagh M. K., Bekki K., Couch W. J. et al., 2023, MNRAS, **518**, 5260.

Pillepich A., Springel V., Nelson D., Genel S. et al. 2018, MNRAS, **473**, 4077.

Pintos-Castro I., Yee H. K. C., Muzzin A., Old L. et al., 2019, ApJ, **876**, 40.

Plat A., Charlot S., Bruzual G., Feltre A. et al., 2019, MNRAS, **490**, 978.

Poggianti B. M., Bressan A., Franceschini A., 2001, ApJ, **560**, 195.

Poggianti B. M., von der Linden A., De Lucia G., Desai V. et al., 2006, ApJ **642**, 188.

Poggianti B., Fasano G., Bettoni D. et al., 2009, ApJL **697**, L137.

Poggianti B. M., Fasano G., Omizzolo A., Gullieuszik M. et al., 2016, AJ, **151**, 78.

Poggianti B. M., Moretti A., Gullieuszik M., Fritz J. et al., 2017, ApJ, **844**, 48.

Poggianti B. M., Ignesti A., Gitti M., Wolter A. et al., 2019, ApJ, **887**, 155.

Popesso P., Concas A., Cresci G., Belli S. et al., 2023, MNRAS, **519**, 1526.

Postman M. & Geller M. J, 1984, ApJ, **281**, 95.

Postman M., Franx M., Cross N. J. G., Holden B. et al., 2005, ApJ, **623**, 721.

Pranger F., Böhm A., Ferrari C., Maurogordato S. et al., 2014, A&A, **570**, A40.

Pratt G. W., Croston J. H., Arnaud M., Böhringer H. et al., 2009, A&A, **498**, 361.

Reddy N. A., Pettini M., Steidel C. C., Shapley A. E. et al., 2012, ApJ, **754**, 25.

Rhee J., Smith R., Choi H., Yi S. K. et al., 2017, ApJ, **843**, 128.

Roberts I. D. & Parker L., 2020, MNRAS, **495**, 554.

Roediger E. & Hensler G., 2005, A&A, **433**, 875.

Roediger E. & Brüggen M., 2007, MNRAS, **380**, 1399.

Rudnick G., Jablonka P., Moustakas J., Aragón-Salamanca A. et al., 2017, ApJ, **850**, 181.

Salim S., 2014, SAJ, **189**, 1.

Salmon B., Papovich C., Finkelstein S. L., Tilvi V. et al., 2015, ApJ, **799**, 183.

Salpeter E. E., 1955, ApJ, **121**, 161.

Sánchez-García O., Cervantes Sodi B., Fritz J., Moretti A. et al., 2023, ApJ, **945**, 2.

Sánchez S. F., Kennicutt R. C., Gil de Paz A., van de Ven G. et al., 2012, A&A, **538**, A8.

Sánchez S. F, Rosales-Ortega F. F., Iglesias-Páramo J., Mollá M. et al., 2014, A&A, **563**, A49.

Sánchez S. F., Barrera-Ballesteros J. K., Lacerda E., Mejía-Narvaez A. et al., 2022, ApJS, **262**, 36.

Sánchez-Blázquez, P., Peletier, R. F., Jiménez-Vicente, J., et al. 2006, MNRAS, **371**, 703.

Schawinski K., Lintott C., Thomas D., Sarzi M. et al., 2009, MNRAS, **396**, 818.

Schawinski, K., Urry C. M., Simmons B. D., Fortson L. et al., 2014, MNRAS, **440**, 889.

Schneider P., 2006, Extragalactic Astronomy and Cosmology, Springer.

Sellwood J. A. & Wilkinson A., 1993, Rep. Prog. Phys, **56**, 173.

Shan Y., McDonald M., Courteau S., 2015, ApJ, **800**, 122.

Sheen Y.-K., Smith R., Jaffé Y., Kim M., 2017, ApJL, **840**, L7.

Shen J. & Sellwood J. A., 2004, ApJ, **604**, 614.

Sheth K., Melbourne J., Elmegreen D. M., Elmegreen B. G. et al., 2012, ApJ, **758**, 136.

Shim H., Im M., Lee H. M., Lee M. G. et al., 2011, ApJ, **727**, 14.

Silk J. & Rees M. J., 1998, A&A, **331**, L1.

Silk J., Di Cintio A., Dvorkin I. et al., 2014, Proc. of the International School of Physics 'Enrico Fermi' Course 186 'New Horizons for Observational Cosmology' Vol. 186, p. 137.

Simard L., Clowe D., Desai V., Dalcanton J. J. et al., 2009, A%A, **508**, 1141.

Smethurst R. J., Lintott C. J., Simmons B. D, Schawinski K. et al., 2015, MNRAS, **450**, 435.

Smith R. J., Lucey J. R., Hammer D., Hornschemeier A. E. et al., 2010, MNRAS, **408**, 1417.

Smith R., Michea J., Pasquali A., Calderón-Castillo P. et al., 2021, ApJ, **912**, 149.

Sobral D., Best P. N., Smail I., Mobasher B. et al., 2014, MNRAS, **437**, 3516.

Somerville R. S. & Davé R., 2015, ARA&A, **53**, 51.

Somerville R. S., Lee K., Ferguson H. C., Gardner J. P. et al., 2004, ApJL, **600**, L171.

Speagle J. S., Steinhardt C. L., Capak P. L., Silverman J. D., 2014, ApJS, **214**, 15.

Stanek R., Evrard A. E., Böhringer H., Schuecker P. et al., 2006, ApJ, **648**, 956.

Stanford S. A., Eisenhardt P. R., Dickinson M., 1998, ApJ, **492**, 461.

Stroe A., Sobral D., Dawson W., Jee M. J. et al., 2015, MNRAS, **450**, 646.

Tacchella S., Diemer B., Hernquist L., Genel S. et al., 2019, MNRAS, **487**, 5416.

Tanaka M., Goto T., Okamura S., Shimasaku K. et al., 2004, AJ, **128**, 2677.

Tapia T., Eliche-Moral M. C., Aceves H., Rodríguez-Pérez C. et al., 2017, A&A, **604**, A105.

Taranu D. S., Hudson M. J., Balogh M. L., Smith R. J. et al., 2014, MNRAS, **440**, 1934.

Tawfeek A. A, Cervantes S. B., Fritz J., Moretti A., 2022, ApJ, **940**, 1.

Toomre A., 1977, egsp.conf, 401.

Tovmassian H. M. & Andernach H., 2012, MNRAS, **427**, 2047.

Tremonti C. A., Heckman T. M., Kauffmann G., Brinchmann J. et al., 2004, ApJ, **613**, 898.

Tyler K. D., Rieke G. H., Bai L., 2013, ApJ, **773**, 86.

Valdes, F., Gupta, R., Rose, J. A., et al., 2004, APJSS, **152**, 251.

Valentinuzzi T., Woods D., Fasano G., Riello M. et al., 2009, A&A, **501**, 851.

Valentinuzzi T., Fritz J., Poggianti B. M., Cava A. et al., 2010, ApJ, **712**, 226.

van der Wel A., Noeske K., Bezanson R., Pacifici C. et al., 2016, ApJS, **223**, 29.

Varela J., D'Onofrio M., Marmo C., Fasano G. et al., 2009, A&A, **497**, 667.

Vera M., Alonso S., Coldwell G., 2016, A&A, **595**, A63.

Vink J. S., Muijres L. E., Anthonisse B., de Koter A. et al., 2011, A&A, **531**, A132.

Vollmer B., Cayatte V., Balkowski C., Duschl W. J., 2001, MNRAS, **561**, 708.

Vulcani B., Poggianti B., Aragón-Salamanca A., Fasano G. et al., 2011, MNRAS, **412**, 246.

Vulcani B., Poggianti B. M., Fasano G., Desai V. et al., 2012, MNRAS, **420**, 1481.

Vulcani B., Poggianti B. M., Oemler A., Dressler A. et al., 2013, A&A, **550**, A58.

Vulcani B., Poggianti B. M, Gullieuszik M., Moretti A. et al., 2018, ApJL, **866**, L25.

Vulcani B., Poggianti B. M, Moretti A., Gullieuszik M. et al., 2019, MNRAS, **487**, 2278.

Vulcani B., Poggianti B. M, Smith R., Moretti A. et al., 2022, ApJ, **927**, 91.

Vulcani B., Treu T., Calabrò A., Fritz J. et al., 2023a, ApJL, **948**, L15.

Vulcani B., Poggianti B. M., Gullieuszik M., Moretti A. et al., 2023b, ApJ, **949**, 73.

Wang J., Kauffmann G., Overzier R., Tacconi L. J., 2012, MNRAS, **423**, 3486.

Weidner C. & Kroupa P., 2006, MNRAS, **365**, 1333.

Weinberg M. D., 1985, MNRAS, **213**, 451.

Weinberger R., Springel V., Hernquist L., Pillepich A. et al., 2017, MNRAS, **465**, 3291.

Werle A., Poggianti B., Moretti A., Bellhouse C. et al., 2022, ApJ, **930**, 43.

Whitaker K. E., van Dokkum P. G., Brammer G., Franx M., 2012, ApJL, **754**, L29.

Whitaker K. E., van Dokkum P. G., Brammer G., Momcheva I. G. et al., 2013, ApJL, **770**, L39.

White S. D. M., Clowe D. I., Simard L., Rudnick G. et al., 2005, A&A, **444**, 365.

Whitmore B. C. & Gilmore D. M., 1991, ApJ, **367**, 64.

Wijesinghe D. B., Hopkins A. M., Brough S., Taylor E. N. et al., 2012, MNRAS, **423**, 3679.

Wilman D. J. & Erwin P., 2012, ApJ, **746**, 160.

Wojtak R., Łokas E. L, Mamon G. A., Gottlöber S. et al., 2007, A&A, **466**, 437.

Wright E. L., 2006, PASP, **118**, 1711.

Wuyts S., Förster Schreiber N. M., van der Wel A., Magnelli B. et al., 2011, ApJ, **742**, 96.

Yoon Y. & Im M., 2020, ApJ, **893**, 117.

Yoon Y., Im M., Lee G.-H., Lee S.-K. et al., 2019, NatAs, **3**, 844.

Zhang B., Cui W., Wang Y., Dave R. et al., 2022, MNRAS, **516**, 26.

Zinger E., Dekel A., Kravtsov A., Nagai D. et al., 2018, MNRAS, **475**, 3654.